L-Università ta' Malta
Faculty of Engineering

MASTER OF SCIENCE IN ENGINEERING DISSERTATION

# Evaluation of Superconducting Magnet Technology to Improve the Energy Efficiency of a High Intensity Muon Beam Facility.


ROMAN FARRUGIA

*Supervised by:*

PROF. ING. ANDREW SAMMUT

*Co-supervised by:*

PROF. ING. NICHOLAS SAMMUT, DR. CIRO CALZOLAIO


*A dissertation submitted in partial fulfilment of the requirements for the degree of Master of Science in Engineering*

*by the*

Faculty of Engineering

July 2025

L-Università ta' Malta
Faculty of Engineering

# Copyright Notice

L-Università ta' Malta

**FACULTY/INSTITUTE/CENTRE/SCHOOL** Faculty of Engineering

## DECLARATIONS BY POSTGRADUATE STUDENTS

**(a) Authenticity of Dissertation**

I hereby declare that I am the legitimate author of this Dissertation and that it is my original work.

No portion of this work has been submitted in support of an application for another degree or qualification of this or any other university or institution of higher education.

I hold the University of Malta harmless against any third party claims with regard to copyright violation, breach of confidentiality, defamation and any other third party right infringement.

**(b) Research Code of Practice and Ethics Review Procedures**

I declare that I have abided by the University's Research Ethics Review Procedures. Research Ethics & Data Protection form code ENG-2024-00032.

As a Master's student, as per Regulation 77 of the General Regulations for University Postgraduate Awards 2021, I accept that should my dissertation be awarded a Grade A, it will be made publicly available on the University of Malta Institutional Repository.

# Acknowledgements

I want to express my sincere gratitude to Prof. Ing. Nicholas Sammut and Prof. Ing. Andrew Sammut for providing me with the opportunity to undertake this research project in collaboration with the Paul Scherrer Institute.

My deepest thanks go to my PSI supervisor, Dr. Ciro Calzolaio from the Magnet Section and Head of Simulations and Analysis, whose invaluable advice and guidance were crucial to the completion of this project. I also thank Dr. Stéphane Sanfilippo, Head of the Magnet Section, for his expert management and support throughout the project. Additionally, I am grateful to Mr. Alexander Gabard for providing essential information about the HIMB project and to all members of the Magnet Section for their engaging and insightful discussions, which greatly enriched my work.

Furthermore, I would like to acknowledge Dr. Michal Duda for his assistance with the cryogenic measurements and the technicians Mr. Henrique Garcia Rodrigues and Mr. Yannik Michael Studer for their support with the technical aspects of my master's project. Your collective expertise, dedication, and encouragement have been instrumental in completing this dissertation.

Lastly, I would like to acknowledge the use of the AI tool Grammarly, which assisted me in managing the grammar and language throughout this dissertation.

# List of Publications

The following is a list of publications and conferences from the research conducted during this dissertation.

1. S. Sanfilippo, C. Calzolaio, **R. Farrugia**, A. Gabard, D. Kiselev, A. Knecht, D. Reggiani, R. Riccioli, A. Sammut, N. Sammut, and V. Talanov, "Low Power Consumption Superconducting Solenoids for the PSI High-Intensity Muon Beams Project - A Design Study," *IEEE Transactions on Applied Superconductivity*, vol. 35, no. 5, pp. 1–5, 2025, doi: 10.1109/TASC.2024.3520095.
2. Conference: Symposium on Advanced Technologies in Electrical Systems (SATES25) held on April 8–9, 2025, at the Campus of the Faculté des Sciences et Technologies, Université de Lorraine, Nancy, France; presented by the head of the PSI Magnet Section, Dr. Stéphane Sanfilippo.

# Abstract

The High-Intensity Proton Accelerator (HIPA) facility at the Paul Scherrer Institute (PSI) is undergoing significant upgrades to support advanced experiments on charged lepton flavor violation. To achieve this, one of the existing target stations and its two connected beamlines will be dismantled and rebuilt as part of the High-Intensity Muon Beam (HIMB) project. The new MuH2 and MuH3 beamlines will incorporate 15 large aperture solenoids and five dipoles designed for muon beam transport to handle a large phase-space beam. The transport beamline components are based on standard resistive magnets, which suffer from high power consumption. This study explores the integration of superconducting magnet technology as a viable alternative to reduce power consumption and enhance the overall performance of the HIMB facility.

A simulation model incorporating radiation-induced thermal loads was developed using COMSOL Multiphysics, enabling realistic assessments of magnet performance. The study revealed that while low-temperature superconducting solenoids, which are based on Niobium-Titanium (NbTi), are effective in most settings, the extreme radiation heat load close to the target requires the use of a High-Temperature Superconductor (HTS) like Yttrium Barium Copper Oxide (YBCO) to ensure thermal stability and resilience. This led to successfully modeling an HTS YBCO solenoid, demonstrating its superior performance in high-radiation scenarios.

To further advance the feasibility of superconducting technology, the dissertation investigated layer winding techniques for YBCO tapes to overcome the challenges associated with traditional winding methods. Practical testing of a layer-wound YBCO magnet prototype at PSI confirmed no degradation in critical current, validating this method for future Research and Development (R&D) activities, particularly for the HTS demonstrator for HIMB radiation damage testing.

Economic and environmental evaluations underscored the substantial benefits of adopting superconducting solenoids over resistive magnets, highlighting significant energy savings and reductions in Carbon Dioxide ($CO_2$) emissions despite higher initial costs. Results of this study have shown that, over 15 years, operational savings make superconducting technology a financially and environmentally viable alternative. Consequently, the PSI directorate endorsed implementing one superconducting solenoid for HIMB, marking a significant advancement in PSI's commitment to sustainable, energy-efficient accelerator technologies and setting a benchmark for future integrations within the HIMB facility and beyond.

# Contents

# List of Figures

# List of Tables

# List of Abbreviations

**CERN** European Organization for Nuclear Research . . . . . 9
**CHART** Swiss Accelerator Research and Technology . . . . . 8
**$CO_2$** Carbon Dioxide . . . . . iii
**FEA** Finite Element Analysis . . . . . 5
**FCC** Future Circular Collider . . . . . 9
**HIPA** High-Intensity Proton Accelerator . . . . . iii
**HIMB** High-Intensity Muon Beam . . . . . iii
**HTS** High-Temperature Superconductor . . . . . iii
**IMPACT** Isotope and Muon Production using Advanced Cyclotron and Target technologies . . . . . 1
**LCA** Life Cycle Assessment . . . . . 26
**LTS** Low-Temperature Superconductor . . . . . 3
**MIITS** Mega Current Squared Time Seconds . . . . . 15
**MLI** Multilayer Insulation . . . . . 13
**$\mu$SR** Muon Spin Rotation . . . . . 1
**NbTi** Niobium-Titanium . . . . . iii
**NTS** Normal Transport Solenoid . . . . . 79
**PHP** Pulsating Heat Pipe . . . . . 23
**PSI** Paul Scherrer Institute . . . . . iii
**PM** Permanent Magnet . . . . . 9
**P3** PSI Positron Production . . . . . 8
**R&D** Research and Development . . . . . iii
**RTS** Radiation-hard Transport Solenoid . . . . . 78
**SINQ** Spallation Neutron Source . . . . . 1
**SLS** Swiss Light Source . . . . . 3
**S$\mu$S** Swiss Muon Source . . . . . 1
**TATTOOS** Targeted Alpha Tumor Therapy and Other Oncological Solutions . 1
**YBCO** Yttrium Barium Copper Oxide . . . . . iii

# 1

# Introduction

## 1.1 | Introduction to the HIMB Project

At Paul Scherrer Institute, the High-Intensity Proton Accelerator facility is a cornerstone of the institute's advanced research infrastructure. Operational since the 1970s, HIPA accelerates protons up to an energy of 590 MeV and a beam current of 2.4 mA, delivering a total beam power of 1.4 MW. This intense proton beam powers the Swiss Muon Source (S$\mu$S) for muon-based research, the Spallation Neutron Source (SINQ) for neutron generation, and various particle physics and materials science experiments. HIPA's proton beams are indispensable for Muon Spin Rotation ($\mu$SR) studies, probing materials' magnetic and electronic properties and enabling some of the most sensitive searches for Beyond Standard Model physics.

Under the Isotope and Muon Production using Advanced Cyclotron and Target technologies (IMPACT) project, PSI has undertaken significant upgrades to enhance its research capabilities. IMPACT has two main sub-projects: the High-Intensity Muon Beam project and the Targeted Alpha Tumor Therapy and Other Oncological Solutions (TATTOOS) project. While HIMB aims to significantly increase muon production rates for particle physics and condensed matter research, TATTOOS focuses on producing medical isotopes for cutting-edge cancer treatments. HIMB and TATTOOS represent a comprehensive approach to meeting the increasing demands of scientific research and clinical applications, positioning PSI as a versatile, sustainable facility for advanced physics, chemistry, and medicine studies. The future layout of HIPA, including the new beamlines and the TATTOOS project, is illustrated in Figure 1.1.

The HIMB project is a transformative upgrade designed to increase PSI's muon production rates by two orders of magnitude, elevating muon rates from approximately $10^8$ $\mu^+$/s to $10^{10}$ $\mu^+$/s. This enhancement is essential for next-generation experiments in charged lepton flavor violation and advanced $\mu$SR applications. The HIMB project involves dismantling one of HIPA's existing target stations and its connected beamlines to accommodate the new high-intensity beamlines, MuH2 and MuH3. These beamlines incorporate 15 large-aperture solenoids and five dipoles designed to manage and focus a large phase-space muon beam, ensuring efficient transport and high beam quality for experimental applications.

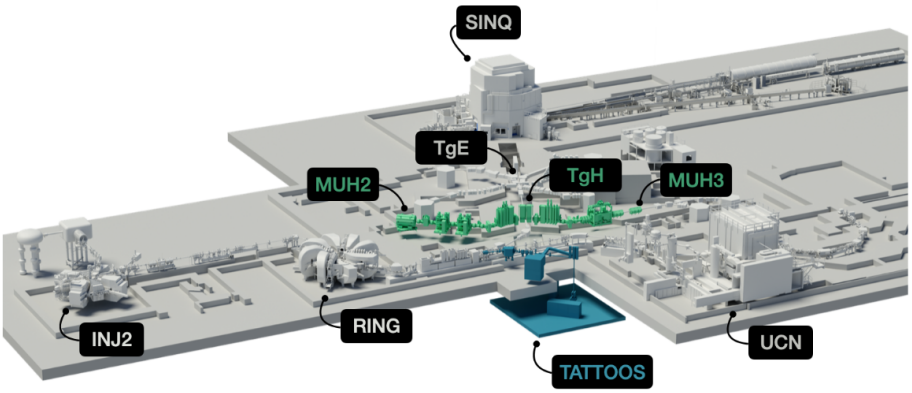


Figure 1.1: Future HIPA facility layout incorporating the new beamlines MuH2 and MuH3, along with the TATTOOS project [1].

Due to the high radiation environment in the HIMB facility, MuH2 beamline locations are categorized based on radiation exposure levels, as shown on the left side of the proton beam in Figure 1.2. For MuH3 located on the right side of the proton beam, the positions are undefined as no radiation data is available.

- Positions A and B: Located close to the target station TgH, these positions are highly and moderately exposed to radiation, respectively. They employ mineral-insulated conductors (MIC) to ensure radiation hardness and operational reliability [2].
- Position C: Experiences no significant radiation exposure and utilizes organic rather than mineral insulation, suitable for lower radiation environments.

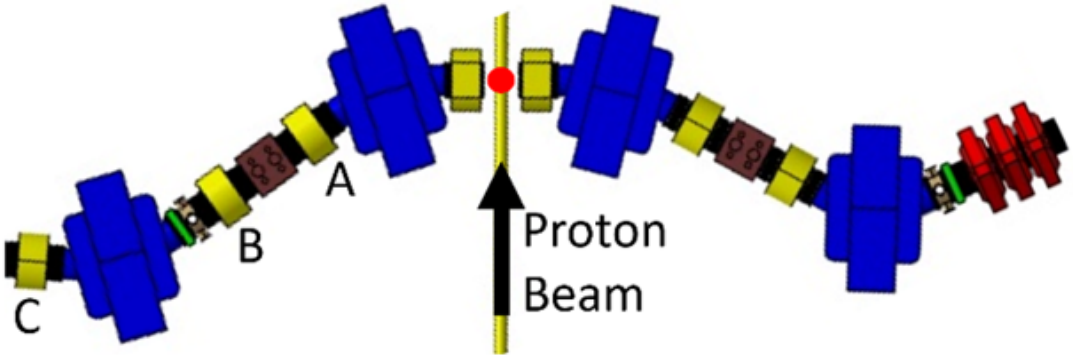


Figure 1.2: Positions within the MuH2 beamline.

The design and power consumption of the resistive magnets for HIMB has been thoroughly studied and presented in [3]. Table 1.1 presents the power consumption of all the resistive magnets deployed in HIMB. The beamlines operate under different cycles: MuH2 operates at 80 MeV/c for 5% of the time and at 28 MeV/c for 95%, while MuH3 operates at 28 MeV/c continuously, reflecting their distinct experimental requirements. The most power-consuming magnets are the transport solenoids at positions A, B, and C

and the capture solenoid at the target. An overview of the magnet configurations in the MuH2 and MuH3 beamlines is shown in Figure 1.3, showing the complex arrangement of solenoids and dipoles required for beam transport and focusing.

| Location | Magnet | Number | Power per Magnet | Total Power |
|---|---|---|---|---|
| MuH2 | Capture Solenoid | 1 | 142.5 kW | 142.5 kW |
| | Dipole | 1 | 3.2 kW | 3.2 kW |
| | Transport Solenoid (A-B) | 3 | 40 kW | 120 kW |
| | Dipole | 1 | 2.4 kW | 2.4 kW |
| | Transport Solenoid (C) | 6 | 18.9 kW | 113.2 kW |
| | Separator | 2 | 0.65 kW | 1.29 kW |
| MuH3 | Capture Solenoid | 1 | 142.5 kW | 142.5 kW |
| | Dipole | 1 | 2.3 kW | 2.3 kW |
| | Transport Solenoid (A-B) | 2 | 38 kW | 76 kW |
| | Dipole | 2 | 3.1 kW | 6.2 kW |
| | Transport Solenoid (C) | 2 | 16.4 kW | 32.8 kW |
| General | Other magnets | 2 | 5 kW | 10 kW |
| **TOTAL** | | | | **652 kW** |

Table 1.1: Power consumption of magnets at different locations along the HIMB beamline.

## 1.2 | Motivation

Energy consumption is critical for large-scale research facilities like PSI, where traditional resistive magnets contribute significantly to operational costs and environmental impact. The HIMB project is expected to increase power demands from 120 kW to approximately 652 kW, primarily due to the extensive use of resistive solenoids for high-intensity beam transport [1].

The previous PSI upgrade at the Swiss Light Source (SLS) reduced energy consumption by replacing resistive magnets with permanent magnet alternatives. However, this approach cannot be applied to HIMB. First, HIMB's proton beam requires a much higher magnetic field strength because of the greater mass of protons. Second, the beamline in HIMB is larger, necessitating magnets with significantly larger apertures. Additionally, the high-radiation environment at HIMB renders permanent magnets unfeasible because they cannot withstand such conditions. Consequently, the HIMB project must explore superconducting alternatives to manage power consumption and maintain operational efficiency effectively.

Based on the findings on power consumption and magnet design presented in [3] and shown in Figure 1.3, this study focuses on evaluating superconducting solenoids—specifically a Low-Temperature Superconductor (LTS) like NbTi and a

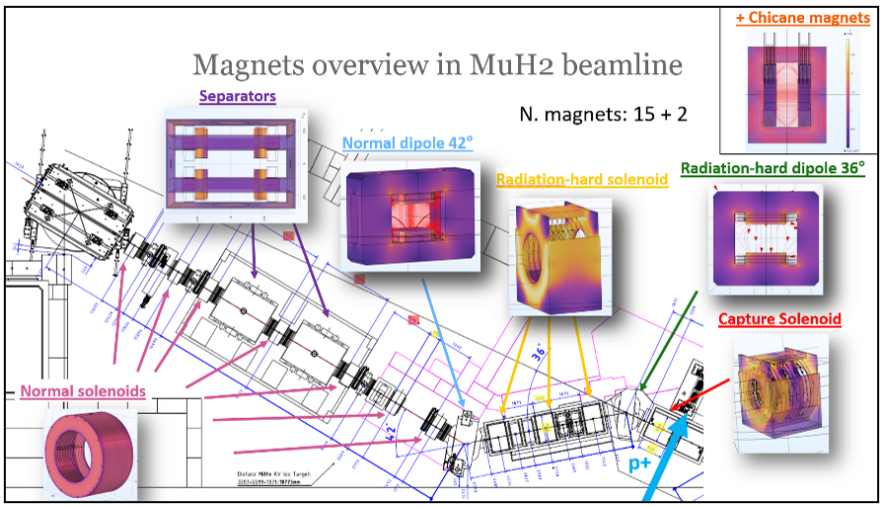


(a) Magnet overview in MuH2 beamline.

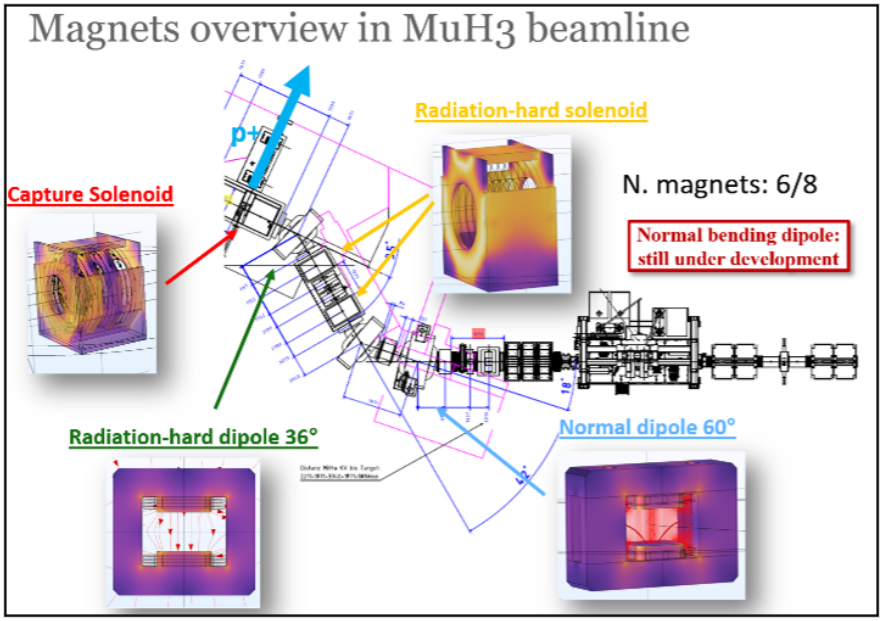


(b) Magnet overview in MuH3 beamline.

Figure 1.3: Magnet configurations in the MuH2 and MuH3 beamlines. Credit to Dr. Rebecca Riccioli from the PSI Magnet Section for the magnet configurations.

High-Temperature Superconductor such as Yttrium Barium Copper Oxide as viable alternatives for transport solenoids at positions A, B, and C. Superconducting solenoids offer the potential to significantly reduce power consumption by eliminating resistive losses, aligning with PSI's goals for energy efficiency and sustainability. However, the high-radiation environment poses unique challenges for superconducting materials, such as radiation-induced damage and thermal loads, necessitating a comprehensive evaluation of their feasibility and performance under HIMB conditions.

This research aims to contribute to the implementation of superconducting technology at PSI by exploring the feasibility of replacing the normal and radiation-hard transport solenoids with superconducting versions. The methodologies and findings will support PSI's immediate goals for the HIMB project and offer a scalable approach applicable to other particle accelerator facilities facing similar energy and radiation challenges. Superconducting solutions can enhance research infrastructure sustainability, reduce operational costs, and maintain PSI's leadership in high-intensity beam technology.

## 1.3 | Aims and Objectives

The primary aim of this dissertation is to evaluate the potential of superconducting technology to save energy at the new HIMB facility at the Paul Scherrer Institute. The research is structured around four key objectives:

1. Conduct a comprehensive literature review on the radiation environment and damage mechanisms:
    - Review and synthesize existing literature on radiation-induced degradation in superconducting magnets and their components, focusing on identifying key damage mechanisms, material vulnerabilities, and operational limitations.
    - Collaborate with the PSI beam dynamics team to integrate and analyze available radiation data at the HIMB facility, ensuring a robust understanding of the radiation environment relevant to the study.
2. Develop a superconducting model of the HIMB transport solenoid incorporating radiation effects:
    - Create a detailed Finite Element Analysis (FEA) model of a superconducting transport solenoid tailored for the HIMB facility.
    - Integrate radiation impact assessments into the FEA model to predict performance and safety parameters.

3. Investigate winding techniques for YBCO magnets to inform future design of HTS solenoids at PSI:
    - Analyze the layer winding method for YBCO tapes.
4. Evaluate the environmental and economic feasibility of implementing superconducting solenoids in the HIMB project:
    - Conduct a comprehensive environmental impact assessment, including material life cycle analysis.
    - Perform an economic analysis to compare the costs and benefits of superconducting solenoids versus traditional resistive magnets.

## 1.4 | Dissertation Structure

This dissertation is organized into six chapters. Chapter 1 introduces the context and motivation of the project, highlighting the limitations of traditional resistive magnets in high-intensity, high-radiation environments and the potential advantages of adopting superconducting technology.

Chapter 2 provides a thorough literature review, examining existing superconducting magnet technologies, critical design considerations, and the effects of radiation on superconducting materials. This chapter identifies key research gaps and technological challenges that the subsequent chapters aim to address.

Chapter 3 presents the design, development, and simulation analysis of superconducting solenoids for the HIMB environment. It begins with a detailed description of the COMSOL Multiphysics model, which integrates magnetic, thermal, and mechanical factors. The chapter outlines the selection of materials, configuration of key components, and simulation parameters used to replicate operational conditions, including radiation-induced thermal effects and quench studies. The simulation results for NbTi solenoids are then presented, and their magnetic field strength, thermal stability, and mechanical integrity under high-radiation conditions are evaluated. The analysis demonstrates that while NbTi solenoids perform effectively under most scenarios, they encounter significant challenges in extreme radiation environments.

Chapter 4 explores the performance of YBCO solenoids in high-radiation, high-intensity environments, addressing the limitations of NbTi solenoids identified in Chapter 3. Additionally, the second part of the chapter includes a practical component of layer winding techniques of YBCO tapes and critical current testing of the wound magnet.

Chapter 5 conducts economic and environmental analysis, comparing superconducting solenoids with traditional resistive magnets regarding costs,

energy savings, and $CO_2$ emissions. Based on the findings of this analysis, the chapter presents the PSI Directorate's favorable decision to adopt superconducting technology for the HIMB facility, accepting the proposal outlined in this dissertation.

Finally, Chapter 6 concludes the dissertation by synthesizing the research findings, discussing their implications for the HIMB facility, and outlining recommendations for future work to advance superconducting magnet technology in high-radiation, high-efficiency particle accelerator environments.

# 2

# Literature Review

At the PSI, the integration and optimization of superconducting magnets have been pivotal in several key projects, including the upgrade of the SLS and the Swiss Accelerator Research and Technology (CHART) collaboration's PSI Positron Production (P3) demonstrator project. As particle accelerators evolve, the demand for more efficient and reliable superconducting solenoids grows, necessitating ongoing research and development.

This literature review systematically explores the various dimensions of PSI's superconducting magnet technology. It begins with an overview of the institute's current implementation and advancements of superconducting solenoids. The review delves into the critical design considerations, including magnetic, thermal, mechanical, and quench protection aspects that ensure optimal performance and reliability. The impact of high-radiation environments on superconducting materials is examined, highlighting the challenges and mitigation strategies essential for maintaining solenoid integrity.

Furthermore, the section on winding techniques for YBCO tapes discusses the current methodologies, their challenges, and the potential for innovation in large-diameter coil applications.

Finally, the review assesses the economic and environmental implications of adopting superconducting technology, providing a comprehensive analysis of its feasibility and sustainability compared to traditional resistive magnets.

This comprehensive literature review identifies existing research gaps. It sets the foundation for future studies to enhance superconducting magnets' efficiency, reliability, and sustainability in high-intensity and high-radiation particle accelerator environments.

## 2.1 | Superconducting Magnets at PSI

At the PSI, the integration of superconducting solenoids has been a key focus in advancing accelerator technology, primarily aimed at improving machine performance rather than saving energy. The ongoing upgrade of SLS2 involves replacing two existing resistive superbend dipoles with superconducting dipole counterparts [4].

While this transition was initially motivated by the need to enhance performance, it has also considerably reduced energy consumption and operational costs. Despite these operational upgrades, the SLS2 project has demonstrated energy savings in magnet operation compared to SLS, highlighting the commitment of PSI towards sustainability. However, this has mainly been achieved through the implementation of Permanent Magnet (PM) technology, entirely omitting the power consumption of previous resistive magnets. In the case of HIMB, such an approach will not work as described in section 1.2.

In addition to the SLS2 upgrade, PSI 's CHART collaboration is undertaking the P3 demonstrator project, which involves analyzing an HTS magnet. This project was initially focused on evaluating the feasibility and performance of HTS magnets in high-energy environments, with potential applications in future facilities such as the Future Circular Collider (FCC) at European Organization for Nuclear Research (CERN). By replacing some resistive magnets with superconducting alternatives, the P3 project seeks to enhance energy efficiency further and reduce the carbon footprint of large-scale accelerator infrastructures [5]. However, unlike previous projects where superconducting technology was primarily utilized to improve performance, the HIMB project marks the first instance at PSI where superconducting solutions are being employed specifically to achieve substantial energy savings and operational cost reductions.

PSI plans to integrate a superconducting solenoid demonstrator into the HIMB. The HIMB solenoid demonstrator is expected to provide crucial radiation damage data, paving the way for broader implementation of energy-efficient superconducting magnets in particle accelerators.

Overall, the HIMB project exemplifies the shift towards more sustainable and energy-efficient technologies in particle accelerator systems by integrating superconducting magnets. By replacing resistive solutions with superconducting alternatives, the HIMB project enhances the performance and energy efficiency of its accelerators. It aligns with global sustainability goals by significantly reducing energy consumption and operational costs.

## 2.2 | Design Considerations

Designing superconducting solenoids requires a multidisciplinary approach addressing magnetic, thermal, mechanical, and quench protection to ensure optimal performance and reliability. Building upon the foundational principles outlined by [6, 7], this section highlights the critical elements essential for developing efficient and robust superconducting solenoids. Understanding these considerations is vital for advancing solenoid design in high-performance particle accelerators and informs the methodology

of this research.

### 2.2.1 | Magnetic Design

The magnetic design of a superconducting solenoid is a fundamental aspect that determines the solenoid's ability to generate and maintain the desired magnetic field strength and uniformity. Key considerations in magnetic design include:

1. **Magnetic Field at the Center**: The magnetic field at the center of a solenoid is a critical parameter that influences beam focusing and control within a particle accelerator.

2. **Magnetic Field Profile**: Besides the field strength at the center, the overall magnetic field profile is essential for ensuring beam stability and minimizing external interference. Reducing the fringe field, which is the magnetic field extending beyond the intended region, is crucial for preventing unwanted interactions with surrounding equipment and maintaining the integrity of the beam path. Techniques to achieve a controlled field profile include optimizing coil geometry, employing magnetic shielding materials, and implementing the magnetic yoke.

3. **Critical surface**: The critical surface defines the boundary in current density ($J$), magnetic field ($B$), and temperature ($T$) space beyond which the superconducting material transitions to the resistive state, potentially leading to a quench. Analyzing the critical surface is crucial for determining safe operating conditions and ensuring adequate quench and temperature margins.

The following subsubsections describe the methods used to calculate the ampere-turns, maximum magnetic field, stored energy in superconducting solenoids, and evaluate the critical surface for quench protection.

#### 2.2.1.1 | Ampere-Turns Calculation

The magnetic field generated by a solenoid is directly proportional to the number of ampere-turns, which is the product of the total number of turns $N$ and the current $I$ flowing through the solenoid. The peak magnetic field $B_0$ at the center of the solenoid is given by [6, 7]:

$$B_0 = J r_{\text{in}} F(\alpha, \beta), \tag{2.1}$$

Where:

- $J$ is the average overall current density (A/m$^2$),

- $r_{\text{in}}$ is the inner radius of the solenoid (m),
- $F(\alpha, \beta)$ is a geometric factor defined as:

$$F(\alpha, \beta) = \mu_0 \beta \ln \left( \frac{\alpha + \sqrt{\alpha^2 + \beta^2}}{1 + \sqrt{1 + \beta^2}} \right), \tag{2.2}$$

With:

- $\alpha = \frac{r_{\text{in}} + t}{r_{\text{in}}}$,
- $\beta = \frac{l}{2r_{\text{in}}}$,
- $t$ is the thickness of the solenoid (m),
- $l$ is the length of the solenoid (m),
- $\mu_0 = 4\pi \times 10^{-7}$ H m$^{-1}$ is the permeability of free space.

The average current density $J$ can also expressed as:

$$J = \frac{NI}{lt}. \tag{2.3}$$

By plugging in the values of $B_0$, $r_{\text{in}}$, and $F(\alpha, \beta)$, the total number of ampere turns $NI$ and the operating current can be calculated. This calculation, together with the operating temperature and the maximum magnetic field, is essential to obtaining the operating margins of the superconducting solenoid.

#### 2.2.1.2 | Maximum Magnetic Field and Stored Energy

Determining the maximum magnetic field $B_{\text{max}}$ within the solenoid is essential, as it influences the critical surface and operational limits of the superconducting material. Calculating the stored magnetic energy $E$ provides insights into energy management and quench protection requirements.

As noted in [6, 7], no analytical solution exists, and for this end, numerical methods such as COMSOL are employed.

#### 2.2.1.3 | Critical surface

The critical surface varies depending on the material and the manufacturer. For NbTi there exists an analytical solution for the critical surface, which also depends on the manufacturer, this is outlined in [8]. In the case of the YBCO tapes, the critical surface databases exist [9].

The quench margin $Q_m$ is calculated using:

$$Q_m = \frac{I_{\text{op}}}{I_{\text{load}}}, \tag{2.4}$$

Where $I_{\text{op}}$ is the operating current, and $I_{\text{load}}$ is the current at which the load line from the origin and passing through $I_{\text{op}}$ on the magnetic field-current projection intersects the critical surface. The quench margin is an important metric, with higher margins indicating greater safety against quenching.

Similarly, the temperature margin $T_m$ is determined by subtracting the operating temperature $T_{\text{op}}$ from the load temperature $T_{\text{load}}$, which is calculated by extending the temperature line horizontally from the operating point to the critical surface on a current-temperature projection.

$$T_m = T_{\text{load}} - T_{\text{op}}. \tag{2.5}$$

The temperature margin is a critical parameter that ensures the superconducting material remains below its critical temperature, preventing quenching and maintaining superconductivity. For LTS, the margins are significantly lower compared to HTS, making thermal management and quench protection more challenging.

### 2.2.2 | Thermal Design

Thermal management is essential to maintain superconductivity and prevent quenching. A well-designed thermal system keeps the solenoid operating below its critical temperature.

The key aspect is the analytical thermal budget. The thermal budget calculation provides an initial estimate of the heat load, guiding the selection of an appropriate cryocooler. For this project, the choice of the cryocooler is optimized for energy saving by selecting a cryocooler with the lowest possible power consumption while maintaining the thermal budget.

The thermal budget considers several heat load components, based on the work of [10, 11] on the large hadron collider (LHC) magnets at CERN [12, 13]. Their approach was also adopted for the SLS2 superconducting Superbend magnet [4]. The heat load components include heat conduction through current leads and structural supports, thermal radiation, heat conduction through sensor wires, and heat deposition from neutron radiation.

**Current leads** : Heat conduction through the current leads is a significant source of heat load. Current leads connect the solenoid to the power supply, and their thermal conductivity can contribute considerable heat to the cryogenic system. A pair of copper leads carrying current between 300 K and 77 K ideally has a shape factor of area per

length of 0.274 $mm^2$/m per ampere and a thermal load of 47 mW/A per lead [6, 14]. A thorough discussion of the derivation of these values is available in [10].

**Structural Supports** : The structural supports connect the solenoid to the cryostat and conduct heat due to the temperature difference between the warm and cold ends. The heat conduction through the supports is governed by the equation [11]:

$$P = \int_{T_c}^{T_h} \frac{A}{L} k(T)\, dT, \tag{2.6}$$

where $P$ is the power (W), $A$ is the cross-sectional area ($m^2$), $L$ is the length (m), $k(T)$ is the thermal conductivity (W $m^{-1}$ $K^{-1}$) as a function of temperature, $T_c$ is the cold temperature, and $T_h$ is the hot temperature. For G-10 fiberglass, commonly used in cryogenic supports due to its low thermal conductivity and good mechanical properties, the integrals of $k(T)$ over the relevant temperature ranges are known. Specifically, for G-10 [10]:

$$\int_{1.9\text{ K}}^{80\text{ K}} k(T)\, dT = 18\text{ W m}^{-1}, \tag{2.7}$$

$$\int_{80\text{ K}}^{290\text{ K}} k(T)\, dT = 135\text{ W m}^{-1}. \tag{2.8}$$

**Thermal Radiation** : Thermal radiation from warmer surroundings to the cold surfaces of the solenoid and thermal shield is another important heat load component. The heat transfer due to radiation can be reduced using Multilayer Insulation (MLI) blankets. The values used in the thermal budget are based on the MLI catalog [15], where an MLI layer covers both the coil and the thermal shield. The heat transfer coefficients are conservatively taken as 2 W $m^{-2}$ for the coil and 0.2 W $m^{-2}$ for the shield, slightly higher than the catalog values to account for uncertainties. These values were measured empirically by the manufacturer and are based on the thermal radiation transfer equations described in [10].

**Sensor Wires** : Heat conduction through sensor wires for temperature and magnetic field monitoring adds to the thermal load. The values for this component are adopted from the SLS2 Superbend project [16], where similar sensor wiring configurations were employed.

**Neutron Radiation** : Neutron radiation contributes to the thermal budget through heat deposition, which is particularly significant for solenoids near the target due to higher radiation levels. The heat deposition from neutron radiation is included in the thermal budget, with values obtained from the radiation dose rates listed in Table 3.2.

**HTS Current Leads** :HTS current leads were considered between the thermal shield and the solenoid. The values for HTS leads were adopted from the manufacturer HTS-110 [17].

### 2.2.3 | Mechanical Design

Mechanical design is critical in ensuring the structural integrity of superconducting solenoids under operational stresses and strains. Finite Element Analysis tools like COMSOL are employed to simulate the electromagnetic forces and system masses, providing approximate assessments of the resulting stresses and strains. G10 material is typically chosen for the support structure due to its low thermal conductivity and adequate mechanical strength, making it ideal for cryogenic environments [10, 11].

A key metric in the mechanical design is the Von Mises stress, which evaluates whether the material can withstand combined loading without yielding [6]. By analyzing the Von Mises stress distribution in simulations, designers can ensure that all components remain within safe operational limits, preventing deformation or failure. This metric is essential for optimizing the support structure, as it helps identify and mitigate potential points of mechanical weakness.

The von Misses stress $\sigma_v$ is determined from the principal stresses $\sigma_r, \sigma_\theta, \sigma_z$ which are namely the radial, the hoop and the axial stress respectively. The von Misses stress is given by [18]:

$$\sigma_v = \sqrt{\frac{1}{2}\left((\sigma_r - \sigma_\theta)^2 + (\sigma_\theta - \sigma_z)^2 + (\sigma_z - \sigma_r)^2\right)}. \tag{2.9}$$

### 2.2.4 | Quench Protection

Quench protection is a critical aspect of superconducting magnet design, aiming to prevent damage from sudden transitions from the superconducting state to the normal resistive state. This transition, known as a quench, can lead to rapid temperature increases and potential thermal and mechanical damage. Adequate quench protection is particularly vital for NbTi solenoids, which typically have lower energy margins compared to YBCO solenoids [19, 20]. Consequently, thorough quench analysis is essential to ensure the safety and reliability of superconducting magnets.

#### 2.2.4.1 | Quench protection circuit

A common quench protection circuit consists of the external dump resistor connected in series with the solenoid, allowing the current to decay rapidly during a quench. Such an approach is described in [6] and adapted by [16]. The circuit is shown in Figure 2.1.

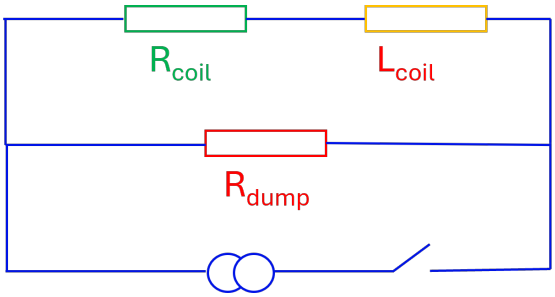


Figure 2.1: Quench protection circuit. The external dump resistor $R_{\text{dump}}$ allows rapid current decay. The $R_{\text{coil}}$ and $L_{\text{coil}}$ indicate the solenoids' developing quench resistance and inductance resepctively. Figure taken from [6].

#### 2.2.4.2 | MIITS Calculation Method

The Mega Current Squared Time Seconds (MIITS) calculation quantifies the thermal energy deposited in the magnet during a quench and is defined as:

$$\text{MIITS} = \int_0^{t_q} J(t)^2 \, dt, \tag{2.10}$$

Where:

- $J(t)$ is the operating current density during the quench,
- $t_q$ is the total quench duration.

To estimate the maximum temperature $T_{\text{max}}$ reached during the quench, Wilson's Gamma integral $\Gamma$ is employed:

$$\Gamma = \int_{T_{\text{op}}}^{T_{\text{max}}} \frac{c(T)}{\rho(T)} \, dT, \tag{2.11}$$

Where:

- $c(T)$ is the volumetric specific heat capacity of the conductor (J m$^{-3}$K$^{-1}$),
- $\rho(T)$ is the electrical resistivity of the conductor ($\Omega$ m),
- $T_{\text{op}}$ is the operating temperature (K).

By equating MIITS to Wilson's integral (MIITS = $\Gamma$), the maximum temperature $T_{\text{max}}$ during the quench can be determined. The MIITS calculation provides a conservative estimate of $T_{\text{max}}$ because it assumes worst-case conditions, modeling the quench as a zero-dimensional system in which all the energy is deposited and fully absorbed by the magnet, without accounting for energy diffusion or heat transfer to the surrounding environment [19].

During a quench, the voltage across the dump resistor represents the maximum voltage the external protection circuit must handle. Using Kirchoff's voltage law, the voltage across the dump resistor $R_d I$ during a quench can be expressed as [6]:

$$-R_d I = L\frac{dI}{dt} + R_{\mathrm{q}} I. \tag{2.12}$$

Where the inductive voltage drop across the solenoid is given by $L\frac{dI}{dt}$ and the developing quench resistance of the solenoid is represented by $R_{\mathrm{q}} I$. Particularly the voltage across the dump resistor is equal to the sum of the inductive voltage drop across the solenoid and the internal resistance of the solenoid.

The temperature distribution within the coil may differ from the analytical estimate due to non-uniform quench propagation and localized cooling effects. These differences between the analytical calculations and the actual behavior are explored through numerical simulations such as in the case of [4].

#### 2.2.4.3 | Material Properties and Wilson's Integral

For accurate MIITS calculations, the volumetric specific heat capacity $c(T)$ and electrical resistivity $\rho(T)$ are primarily derived from the copper content in the conductor, given copper's high thermal conductivity and heat capacity. Contributions from NbTi and epoxy are negligible, allowing the approximation based on copper fraction alone [21].

Wilson's integral $\Gamma$ is evaluated numerically over the temperature range from $T_{\mathrm{op}}$ to $T_{\mathrm{max}}$ using standard copper material property data. By plotting $\Gamma$ against $T_{\mathrm{max}}$, the intersection point where $\Gamma$ = MIITS provides an estimate of the maximum temperature achieved during the quench.

#### 2.2.4.4 | Key Components of Quench Protection

Effective quench protection systems incorporate the following key components:

- **Quench Detection**: Rapid identification of quench events using voltage taps and temperature sensors.
- **Energy Dissipation**: Efficiently dissipating stored energy through external circuits to prevent overheating.
- **Thermal Management**: Designing thermal pathways to distribute heat and avoid localized hotspots.

The MIITS calculation is instrumental in optimizing these components by providing estimates for necessary detection times and energy dissipation rates. For example, maintaining a quench decay time constant ($\tau_{\mathrm{dump}}$) below a certain threshold ensures

that the hotspot temperature remains within safe limits, thereby protecting the solenoid from thermal and mechanical degradation [10].

#### 2.2.4.5 | Analytical and Numerical Simulations

The MIITS method offers an analytical approach to estimate $T_{max}$ numerical simulations using COMSOL Multiphysics to provide a detailed and spatially-resolved analysis of quench dynamics. This approach was demonstrated by [4], where COMSOL simulations were used to model the quench propagation in superconducting magnets. These simulations account for temperature and current distribution within the solenoid, enabling a comprehensive understanding of the quench process.

Comparing MIITS-based estimates with COMSOL simulations validates the analytical models and enhances the accuracy of quench protection strategies. The MIITS calculation provides a conservative baseline, while simulations offer a more detailed view of the temperature distribution and quench dynamics, accounting for localized cooling effects and non-uniform quench propagation. Accurate prediction of the maximum temperature and understanding of the thermal behavior during a quench allows for the design of effective quench protection systems. This effective design ensures the safe and reliable operation of superconducting solenoids in high-energy environments, ultimately enhancing the performance and longevity of particle accelerators.

### 2.2.5 | Simulations

Finite Element Analysis software is indispensable for designing and optimizing superconducting solenoids, enabling detailed modeling of electromagnetic, thermal, and mechanical behaviors. COMSOL Multiphysics is a widely utilized tool in this context, offering the capability to integrate multiple physical phenomena within a single simulation environment.

Several case studies highlight the effectiveness of FEA in advancing superconducting magnet technology at PSI:

**Rossi et al. at Università di Milano**: Rossi and colleagues modeled dipole magnets for the HIMB upgrade using Magnesium Diboride ($MgB_2$) superconductors. Their FEA simulations focused on optimizing magnetic field distribution and thermal stability, demonstrating significant energy savings compared to traditional resistive magnets [22]. While their analysis successfully addressed magnetic, thermal, and mechanical aspects, it did not consider the economic implications of superconducting systems versus resistive alternatives, nor did it incorporate quench analysis.

The lack of an economic breakdown is a major drawback. Due to tight budget constraints, the capital cost of the superconducting magnet plays a significant role in

the viability of adopting superconducting technology at PSI.

**Design of the SLS2 Superbend Magnets at PSI**: Comprehensive FEA analyses of the SLS2 superbend magnets were conducted using COMSOL throughout the project development [4, 16]. These studies encompassed mechanical, thermal, magnetic, and quench analyses, providing a holistic understanding of magnet performance. Notably, their approach to quench protection was instrumental in the design of the HIMB transport solenoid, especially given the absence of a dedicated COMSOL quench module.

While previous studies have offered valuable insights, none have provided a comprehensive framework for fully using FEA software to model superconducting solenoids. This work explicitly fills that critical gap by presenting a detailed design process integrating radiation-induced thermal loads into the FEA model. By combining these additional factors, the study aims to enhance the accuracy and reliability of simulations, ensuring that superconducting solenoids can operate safely and efficiently in high-radiation environments.

## 2.3 | Radiation Effects

Particle accelerators operate in environments with exceptionally high radiation levels, particularly neutron radiation. This intense neutron flux poses significant challenges to the materials and components used within these facilities, including superconducting solenoids. Apart from neutron flux, there is also gamma radiation. Still, the data about the gamma radiation levels in HIMB is unavailable; therefore, this review will focus on neutron radiation.

As illustrated in Figure 2.2, the MuH2 beamline experiences substantial neutron flux. Neutron radiation induces defects in superconducting materials, leading to the degradation of their critical properties. Specifically, studies on NbTi and YBCO have demonstrated that neutron irradiation adversely affects critical current density $J_c$ and critical temperature $T_c$.

In Figure 2.2, the standard unit is taken as MeV cm$^{-3}$ per 1 proton on the target. The collision of the proton beam with the target generates neutron radiation within the beamline. The energy deposition was calculated using a three mA proton beam on the target, which translates to the rate $r$ of

$$r = \frac{3 \times 10^{-3}}{e} \tag{2.13}$$

protons per second where $e = 1.6 \times 10^{-19}$ C is the charge of an electron. Consequently, to convert from MeV cm$^{-3}$ per proton to W m$^{-3}$, the rate of protons is multiplied by the energy deposition where conversion from MeV s$^{-1}$ to W m$^{-3}$ is given by

$$1 \text{ MeV s}^{-1}\text{cm}^{-3} = e \times 10^6 \times 10^6 \text{ W m}^{-3} \tag{2.14}$$

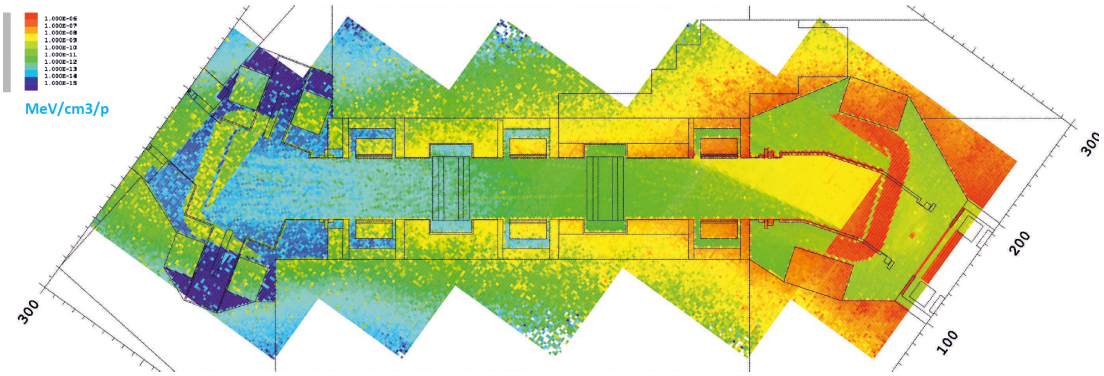


Figure 2.2: Neutron radiation levels in the MuH2 beamline, calculated using the FLUKA simulation toolkit by the beam dynamics team. The figure is available upon request from Dr. Vadim Talanov of the PSI beam dynamics team.

and thus the total factor from MeV cm$^{-3}$ per proton to W m$^{-3}$

$$1 \text{ MeV cm}^{-3}\text{p}^{-1} = 3 \times 10^{-3} \frac{1}{e} \times e \times 10^{6} \times 10^{6} \text{ W m}^{-3} = 3 \times 10^{9} \text{ W m}^{-3} \tag{2.15}$$

Understanding the impact of radiation on these materials is crucial for designing and maintaining reliable superconducting solenoids. Mitigating radiation-induced damage ensures the longevity and performance of superconducting magnets in high-radiation accelerator environments. This section reviews the sources and effects of neutron radiation in particle accelerators and examines how radiation impacts the superconducting properties of NbTi and YBCO.

## 2.3.1 | Impact of Neutron Radiation

This subsection introduces the currently available neutron radiation damage research on the NbTi and YBCO, followed by the impact of radiation on system components beyond superconducting materials.

**NbTi** have been extensively studied for their radiation tolerance since the 1980s. Early research by [23–25] demonstrated that neutron irradiation reduces the critical current density ($J_c$) in NbTi, potentially compromising solenoid performance. However, the critical temperature ($T_c$) decreases only marginally by a few tenths of a degree, rendering the overall degradation negligible [23, 26]. Figure 2.3 from [25] illustrates that after irradiation up to $3 \times 10^{22}$ n/m$^2$ fast neutrons, $J_c$ degrades by approximately 12% at 5 T and 15% at 8 T.

Recent studies at CERN's HiRadMat facility [27–29] have confirmed these findings under high radiation conditions, showing no significant degradation in critical parameters. However, a reduction in the Residual Resistivity Ratio (RRR) indicates a weakening of the copper matrix, leading to decreased thermal stability, however it is

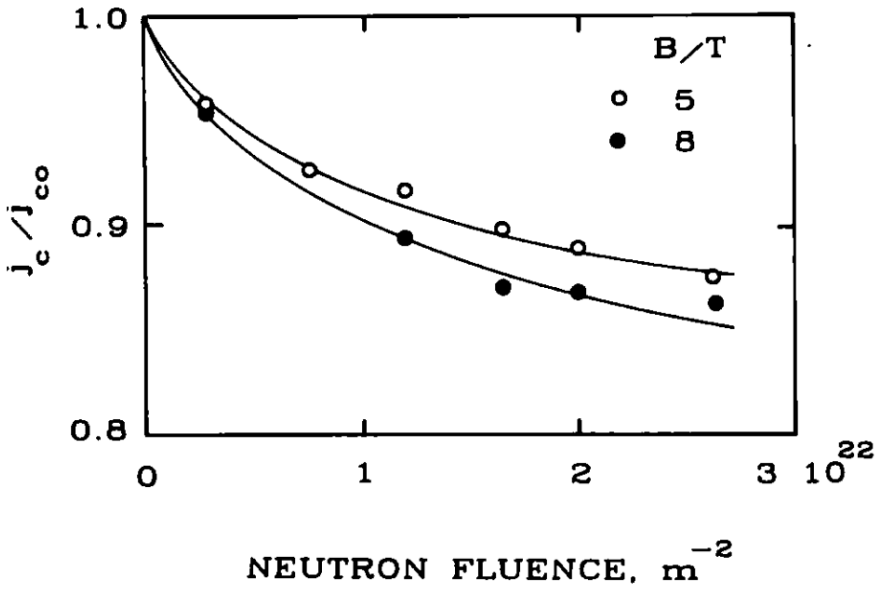


Figure 2.3: Change of critical current densities with fast neutron fluence (E > 0.1 MeV) at 5 and 8 T. Taken from [25].

unclear how the critical current will be affected under long-term radiation exposure in the HIMB.

**High-Temperature Superconductors** , such as YBCO, have also been subject to radiation studies since the early 1990s. Initial research by [30, 31] demonstrated that neutron irradiation adversely affects both $J_c$ and $T_c$ in YBCO. Figure 2.4 from [30] shows that $J_c$ initially increases due to radiation-induced pinning defects before decreasing at higher fluences [32].

Neutron irradiation of superconductors leads to atomic displacements that introduce disorder in the Cu-O chains, resulting in a reduction of the critical properties [30]. Simultaneously, the irradiation-induced defects namely the point defects and collision cascades act as effective pinning centers for fluxoids, initially enhancing $J_c$. However, as the defect density saturates, the ongoing Cu-O chain disorder predominates, causing a decline in $J_c$ [33].

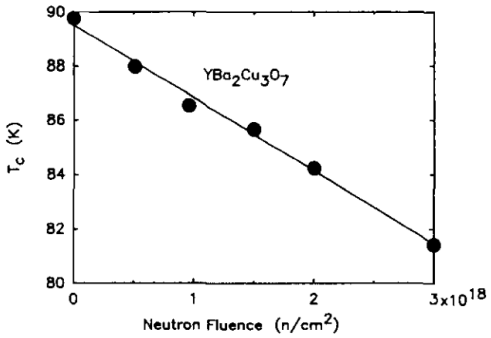


(a) Change in $T_c$ with fast neutron fluence.

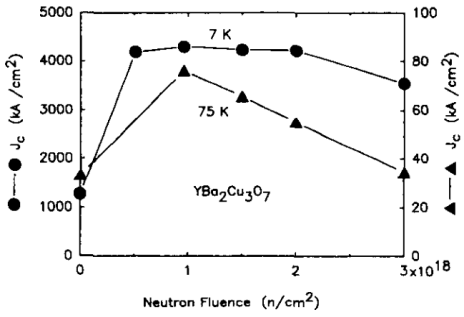


(b) Change in $J_c$ with fast neutron fluence.

Figure 2.4: Radiation damage effects on YBCO. Taken from [30].

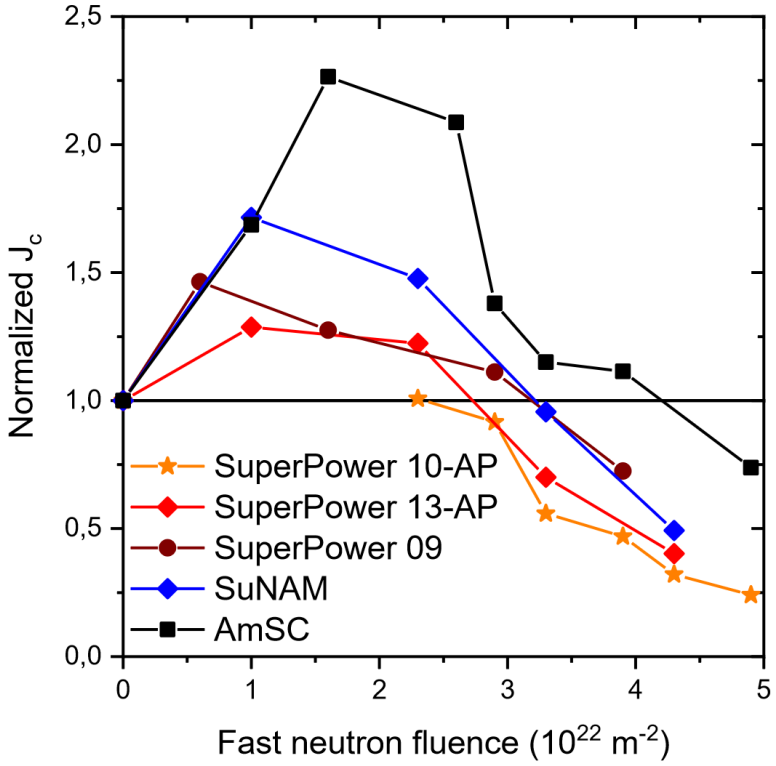


Figure 2.5: Change in $J_c$ with fast neutron fluence for YBCO tapes. Taken from [33].

Recent research at TU Wien Atomics Institute [33–35] and the Czech Institute of Plasma Physics [36] has given further progress on radiation-induced damage in YBCO tapes, confirming a linear decrease in $T_c$ and a non-linear decrease in $J_c$ with increasing neutron fluence. This behavior can be seen in Figure 2.5. However, experimental studies on YBCO magnets are limited, with insights also coming from Monte Carlo simulations of fast neutron flux deposition [37]. More empirical data is required, especially in the case of the HIMB beamline, where the neutron flux is not entirely known.

Radiation also affects system components beyond superconducting materials. The main components are the cryocooler and the insulating material.

Epoxy insulation in solenoids has a radiation tolerance limit of approximately 20 MGy [2, 38]. For HTS applications, alternatives such as steel insulation or non-insulated coils are being explored to withstand higher doses.

Additionally, radiation can degrade cryogenic cooling systems. Industry insights suggest that pulse tube cryocoolers may offer greater resistance to radiation-induced damage than Gifford-McMahon cryocoolers due to their lack of moving parts, though comprehensive analyses are pending.

Despite significant advancements in understanding the impact of radiation on superconducting materials, the full extent of radiation-induced damage remains

inadequately explored. This gap is primarily due to the diverse radiation spectra encountered in various particle accelerators and nuclear facilities. Consequently, further experiments are required to analyze the radiation damage on superconducting components.

For instance, the CERN RADSUM Topical Workshop on Radiation Effects in Superconducting Magnets, scheduled for 2025 [39], will focus on quantifying and contrasting the radiation environments specific to different applications, particularly emphasizing particle accelerators and fusion facilities. Furthermore, the workshop aims to advance the comprehension of how radiation induces degradation in material properties, with the ultimate objective of establishing radiation damage thresholds for superconductors and other magnet components.

To bridge existing knowledge gaps, PSI's P3 project involves testing HTS solenoids in high-radiation environments, aiming to inform future applications for CERN FCC-ee by analyzing radiation damage mechanisms and enhancing solenoid resilience [5]. Additionally, a solenoid demonstrator will be placed in the HIMB to monitor radiation damage over time and gather crucial data for future upgrades in particle accelerators.

In summary, neutron radiation poses significant challenges to both LTS and HTS in particle accelerators. Ongoing and future research is essential to develop radiation-resistant materials and effective mitigation strategies, ensuring the reliability and longevity of superconducting solenoids in high-radiation environments.

### 2.3.2 | Radiation-Induced Heat Load in Beamlines

Neutron radiation significantly contributes to the heat load in particle accelerator beamlines, in addition to causing material degradation. However, current thermal budget calculations for superconducting systems often overlook radiation effects. This study aims to fill this gap by evaluating various radiation levels and their impact on coil temperature, thereby establishing a maximum permissible radiation heat load based on the radiation dose at which the coil temperature reaches the current sharing temperature ($T_{cs}$). It is important to note that the COMSOL simulation will not be able to determine the radiation-induced damages but rather the effects of the radiation-induced heat load on the coil temperature.

Previous studies [40–42] have addressed radiation-induced heat loads in solenoids for the COMET experiment at J-PARC in Japan, the MuSiC experiment at the Research Center for Nuclear Physics in Japan and the EMus project at the China Spallation Neutron Source. However, this study uniquely parametrizes radiation dose and measures coil temperature for each dose, establishing a direct relationship between dose and temperature. This approach allows for a more precise determination of thermal responses under varying radiation conditions.

### 2.3.3 | Radiation Mitigation Strategies

Neutron shielding is a fundamental strategy to protect superconducting solenoids from radiation-induced damage. Various studies [43–45] have evaluated different neutron shielding materials. Among these, K-resin has proven most effective, exhibiting a macroscopic neutron cross-section of 0.19 $cm^{-1}$ [43]. In contrast, [41] utilized a stainless steel radiation shield with a thickness of 30 cm and a cross-section of 0.17 $cm^{-1}$. However, such thickness is impractical for the HIMB due to space constraints.

The relationship between neutron intensity ($I$) and material thickness ($x$) for shielding is governed by the exponential attenuation equation:

$$I = I_0 e^{-\Sigma x} \tag{2.16}$$

Where:

- $I_0$ is the initial neutron intensity,
- $\Sigma$ is the macroscopic neutron cross-section,
- $x$ is the thickness of the shielding material.

To reduce neutron intensity by a factor of 2, K-resin must be approximately 3.65 cm thick, while stainless steel requires 4.07 cm.

Beyond neutron shielding, mitigation strategies extend to other system components, primarily focusing on insulation and cryogenic systems. Utilizing radiation-hardened materials, such as stainless steel, for insulation of the solenoid tape or wire or opting for non-insulated coils helps mitigate radiation damage. Additionally, optimizing the placement and thermal management of cryogenic systems is crucial.

Discussions with Cryomech and Sumitomo, two major cryocooler suppliers, revealed a lack of data on cryocooler radiation damage. One design consideration for both superconducting magnet versions was positioning the cryocooler away from the beamline, minimizing radiation exposure to its components. However, this placement introduces challenges, including limited beamline space and the need for a longer thermal path between the cryocooler and the solenoid. The extended thermal path results in higher coil temperatures due to increased power loss during cooling.

While space constraints are unavoidable, the thermal path can be optimized by utilizing materials with high thermal conductivity, such as copper. In this analysis, a copper path was employed to minimize temperature gradients. Integrating a Pulsating Heat Pipe (PHP) is being considered for future enhancements. PHPs are passive heat transfer devices capable of transferring heat over long distances with minimal temperature drop. Implementing PHPs can increase thermal conductivity by an order of magnitude compared to copper, thereby reducing the temperature gradient between

the cryocooler and the coil. Ongoing research at PSI, in collaboration with the Dutch company VdL, is investigating the effectiveness of PHPs in cooling down HTS magnets, aiming to enhance cooling efficiency and reduce thermal losses in superconducting solenoids.

These mitigation strategies are critical for enhancing the resilience of superconducting solenoids in high-radiation environments. By implementing effective neutron shielding and advanced thermal management solutions, the longevity and performance of superconducting magnets in particle accelerators and future fusion power plants can be significantly improved.

## 2.4 | Layer Winding of YBCO Tapes

The performance and reliability of HTS solenoids are critically dependent on the winding techniques employed during their manufacturing. Effective winding methods ensure optimal superconducting properties, minimize electrical and thermal losses, and maintain structural integrity under operational stresses. Winding techniques such as pancake and layer winding are commonly used for superconducting materials. This section provides an overview of these winding methods, focusing on the layer winding of YBCO tapes.

Pancake winding is a commonly adopted technique for assembling HTS coils, especially when using YBCO tapes in which the conductor is wound in a flat, spiral configuration reminiscent of a stack of pancakes [46]. This geometry leverages the tape's planar form factor to reduce bending-induced stress and maintain superconducting properties [47].

While straightforward, pancake winding results in a high number of joints in large solenoids, potentially compromising superconducting performance and increasing failure points [46, 48]. Additionally, each joint introduces electrical and thermal discontinuities, which can affect the overall efficiency and reliability of the solenoid.

In contrast, layer winding is generally suited for wire-based superconductors and is not directly applicable to HTS tapes due to their distinct mechanical and electrical properties. In layer-wound coils, the coil is wounded in the axial direction before transitioning radially to the next layer. This transition introduces additional points of tension and strain, which can lead to mechanical damage and reduced critical properties. The impact of strain on the critical properties of YBCO tapes is outlined in [49], while the differential geometry method for evaluating strains is discussed in [47].

Despite these challenges, layer winding is still considered advantageous due to the absence of joints, which can enhance the solenoid's overall performance and reliability. A study by [48] found that the additional strain from layer winding does not degrade the critical properties of YBCO tapes, confirming the viability of this winding process.

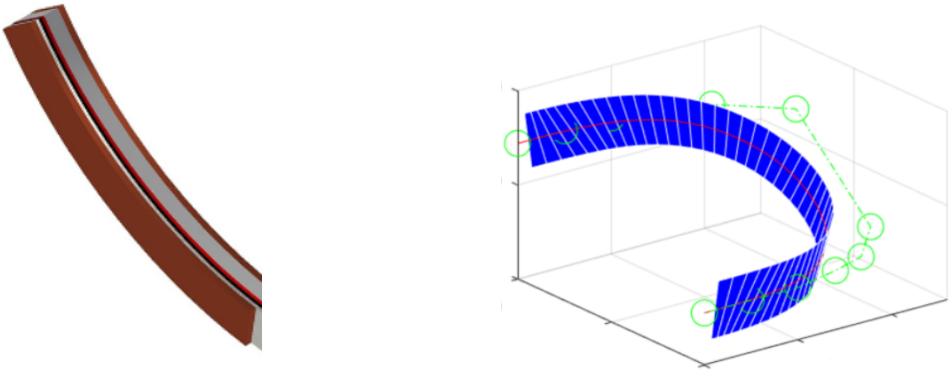

(a) Hardway bending of the HTS tape during layer winding.

(b) Detailed view of the bend using a 3D geometry.

Figure 2.6: Hardway bending of the HTS tape during layer winding. Figures adapted from [47].

However, these studies have typically focused on small-diameter coils (e.g., 60 mm), whereas particle accelerators like the HIMB require much larger diameters (62.5 cm). The effects of layer transitions in larger coils are less pronounced, but a comprehensive analysis is necessary to confirm their impact. This study aims to analyze the effects of layer transitions on large-diameter coils using the infrastructure available at PSI.

High-Temperature Superconductor solenoids have emerged as a significant focus in modern accelerator technology. This is exemplified by the CHART program—a collaborative initiative between PSI, CERN, EPFL, ETH Zurich, and the University of Geneva [50]. Despite these advancements, the winding of large-diameter coils remains largely unexplored, with only a few prototypes, each featuring a diameter of less than 10 cm, having been produced by Dr. Dmitry Sotnikov at PSI. This study addresses this gap by examining the effects of layer winding on large-diameter coils, laying the groundwork for future implementations in the HIMB beamline, particularly for radiation testing applications.

## 2.5 | Economic and Environmental Analysis

Adopting superconducting solenoids over conventional electromagnets involves significant economic and environmental considerations. This section examines superconducting technology's potential cost savings and environmental benefits, comprehensively analyzing its viability as an energy-efficient alternative.

### 2.5.1 | Economic Considerations

Superconducting solenoids are often employed where resistive magnets are inadequate or impractical, serving as enabling technologies. However, they are proposed

as replacements to achieve substantial energy savings in this context. While superconducting magnets entail higher initial capital costs, long-term operational savings due to reduced energy consumption are expected to offset these investments.

Recent projects at Università di Milano have explored energy-efficient upgrades for existing magnets at PSI's HIMB [22, 51]. However, these studies have focused mainly on energy savings, leaving a critical gap in examining the economic implications of transitioning to superconducting technology. This study addresses that gap by providing a comprehensive economic analysis considering initial capital expenditures and long-term operational costs. In doing so, it offers a much-needed framework for evaluating the overall viability and cost-effectiveness of adopting superconducting solutions in this context.

Several economic analyses support this transition. [52] conducted a comparative study of LTS coils versus HTS coils, providing a detailed cost breakdown that enables direct comparisons with resistive coils.

Another relevant study [53] employed a similar cost calculation approach. Still, it focused solely on cryogenics, conductors, and electricity, excluding full system costs such as cryostats, vacuum pumps, instrumentation, power supplies, and assembly. The current study aims to provide a more comprehensive economic evaluation by including these additional factors, offering a more accurate comparison between superconducting and resistive magnet systems.

Conducting a thorough economic analysis encompassing initial capital expenditures and long-term operational costs allows for determining the break-even point for adopting superconducting technology. This evaluation is crucial for assessing the viability of superconducting solenoids as energy-efficient alternatives in particle accelerator facilities and other applications where energy consumption is a significant concern.

### 2.5.2 | Environmental Impact and Sustainability

Aligned with the PSI 's commitment to environmental sustainability, this analysis uses $CO_2$ emissions as the primary metric to assess environmental impact. $CO_2$ directly contributes to global warming and is a key environmental performance indicator.

Superconducting magnets aim to save energy compared to conventional electromagnets. Using a conversion factor of approximately 100 g $CO_2$ per kilowatt-hour (kWh) [54], the environmental benefits of reduced electricity consumption can be quantified. Although this value is approximate, it reasonably estimates $CO_2$ emissions avoided through energy savings.

However, producing superconducting materials—such as the rare earth elements used in HTS and NbTi for LTS—remains an energy-intensive process significantly contributing to $CO_2$ emissions. While a full cradle-to-grave Life Cycle Assessment (LCA) was not performed in this study, such analyses are critical for evaluating

the environmental impact of superconducting materials from raw material extraction ("cradle") through manufacturing, use, and disposal ("grave"). The literature on the LCA of superconducting materials is limited, partly due to the historical emphasis on performance rather than cost efficiency and energy savings.

For example, [55] conducted an LCA for YBCO tapes and reported an emission factor of 5.8 kg $CO_2$ per meter of 12 mm tape—equivalent to 490 kg $CO_2$ per kilogram of YBCO. A notable limitation of this study is its reliance on production data provided directly by THEVA, a manufacturer of YBCO tapes, which may not fully capture variability in production practices across different manufacturers or regions. Similarly, [56] reported emission factors of 7 k g $CO_2$ per kilogram for copper and 17 kg $CO_2$ per kilogram for NbTi wire, underscoring the high energy demands inherent in producing superconducting materials.

Despite the higher production emissions, superconducting magnets require less material than copper magnets to achieve equivalent magnetic performance. Consequently, overall $CO_2$ emissions can still be reduced when considering both production and operational phases. The significant energy savings during operation, resulting from reduced electrical power consumption, further enhance the environmental benefits of superconducting magnets over their lifespan.

A comprehensive assessment that includes operational energy savings and the environmental impact of material production aligns with global eco-friendly goals. This dual consideration supports the development of environmentally responsible technologies and underscores the potential of superconducting solenoids as sustainable alternatives to conventional electromagnets.

## 2.6 | Conclusion

This literature review has comprehensively examined the landscape of superconducting magnets at PSI, focusing on design considerations, radiation effects, economic and environmental impacts, and winding techniques for YBCO tapes. Key findings highlight PSI's significant advancements in integrating superconducting solenoids to enhance accelerator performance and achieve substantial energy savings. Projects such as the Swiss Light Source upgrade and the CHART collaboration's P3 demonstrator underscore the potential of superconducting technology in improving beam stability, precision, and sustainability.

However, several research gaps warrant further investigation, forming the basis of this dissertation. These gaps include:

- **Incorporation of Radiation Effects in FEA Studies**: Current FEA models do not account for the thermal loads of radiation on superconducting systems.

Integrating these effects is essential to determine the maximum permissible radiation dose manageable by cryocoolers, ensuring safe solenoid operation.

- **Radiation Effects on Superconducting Materials**: The long-term impact of neutron radiation on superconducting materials, particularly HTS, is not fully understood. PSI aims to investigate these effects by placing an HTS demonstrator in the HIMB, with the layer versus pancake winding design still pending.
- **Comprehensive Superconducting Solenoid Design**: Existing studies lack a detailed breakdown of FEA software implementation for superconducting solenoids. This research will provide an in-depth overview of the design process and the integration of radiation-induced thermal loads into FEA models.
- **Winding Techniques for HTS Tapes**: Literature on layer winding techniques for HTS tapes remains limited, with pancake winding prevailing due to the inherent geometry of the tapes. This study aims to investigate various winding techniques for YBCO magnets to inform the future design of HTS solenoids at PSI.
- **Comprehensive Economic and Environmental Analysis**: Current studies often overlook low-powered magnets such as 1.5 T where superconducting technology is no longer an enabling technology. A thorough economic and environmental assessment, including material lifecycle impacts, is necessary to evaluate the feasibility of replacing resistive magnets with superconducting alternatives.

Addressing these gaps will advance the development and deployment of superconducting solenoids at HIMB and other particle accelerators, enhancing their performance, reliability, and sustainability in high-radiation particle accelerator environments. This study aims to contribute valuable insights and practical solutions to these pressing challenges, paving the way for more efficient and resilient accelerator technologies.

# 3

# Design of Superconducting Solenoids

This chapter presents a comprehensive framework for the multiphysics simulation of superconducting solenoids, specifically tailored for integration into the HIMB beamline. The primary objective is to validate the solenoid designs against the stringent requirements of high-precision particle accelerator applications. This objective ensures they meet the necessary standards for magnetic field accuracy, thermal stability, mechanical integrity, radiation tolerance, and economic feasibility.

The simulation begins with the detailed modeling of the solenoid using COMSOL Multiphysics. The modeling involves defining design parameters, setting up the geometry, selecting appropriate materials, and integrating various simulation modules. A novel aspect of this study is incorporating a thermal component to account for radiation deposition, modeled by introducing additional heat loads as a proxy for radiation. This approach ensures that the solenoid's thermal management system can effectively handle the heat generated under operational conditions.

Subsequent analyses focus on evaluating the solenoid's performance across multiple domains:

- **Magnetic Properties**: Calculating the required ampere-turns to achieve the desired peak magnetic field of 0.55 T and optimizing the field profile to align with existing resistive magnets. This analysis includes analyzing critical surfaces to ensure adequate quench and temperature margins.

- **Thermal Management**: Developing a detailed thermal budget for heat contributions from current leads, structural supports, radiation, and other sources. Simulations assess whether the selected cryocoolers can effectively manage these loads, particularly in high-radiation environments with substantial heat deposition.

- **Mechanical Stability**: Evaluating the structural resilience of the solenoid under electromagnetic forces and thermal stresses to ensure deformations and stresses remain within safe limits.

- **Quench Protection**: Conducting quench studies to verify that the solenoid can safely transition to a normal conducting state without incurring damage during a

quench event. Simulations provide insights into hotspot temperatures and voltage developments.

- **Radiation Effects**: Investigating the impact of neutron radiation on superconducting materials and overall solenoid performance. This includes assessing the degradation of critical current and temperature and evaluating mitigation strategies such as material selection and shielding.

The methodologies and analyses detailed in this chapter establish a robust foundation for evaluating the superconducting solenoid's design and operational performance, ensuring it meets the specific requirements and constraints of the HIMB beamline.

## 3.1 | Coil Design

The primary design constraints for the superconducting solenoid are as follows:

1. Achieve a peak magnetic field of 0.55 T on the central axis of the solenoid.
2. Ensure an inner aperture diameter larger than 55 cm to accommodate the 50 cm diameter of the beamline.
3. Match the magnetic field profile of the existing resistive solenoid.
4. Steady state application with 4000 hours per year of operation.

Due to limited space in the beamline, the design must be optimized to fit within the available area while adhering to these constraints. Furthermore, it is imperative that the solenoid is designed to achieve the specified magnetic field characteristics while minimizing power consumption. Particular attention must be paid to the cryocooler's capacity to manage the additional thermal load resulting from neutron radiation. Additionally, in the event of a quench, the solenoid must be capable of safely transitioning to the normal conducting state to prevent damage and ensure the continued operational integrity of the system.

### 3.1.1 | Coil Geometry

The solenoid geometry was determined by considering the following parameters in a logical sequence:

1. Solenoid length $L$.
2. Inner radius $R_{\text{in}}$.

3. Thickness of the wire in the radial direction $t_x$.

4. Number of layers in the radial direction $n_x$.

5. Total thickness of the solenoid $t = t_x n_x$.

6. Outer radius $R_{\text{out}} = R_{\text{in}} + t$.

7. Thickness of the wire in the axial direction $t_y$.

8. Number of turns in the axial direction $n_y = \left\lfloor \frac{L}{t_y} \right\rfloor$.

9. Total number of turns $N = n_x n_y$.

### 3.1.2 | Additional Components

In addition to the coil, the superconducting system design included several other components:

1. **Thermal Shield**: A shield cooled to an intermediate temperature of 77 K to reduce the thermal load on the cryocooler at 4 K.

2. **Iron Yoke**: An iron yoke was added to the solenoid to match the field profile of the resistive solenoid more closely by reducing the fringe field.

3. **Cryocooler**: A cryocooler considered for cooling the solenoid.

4. **Cryostat**: A cryostat to house the solenoid and the cryocooler, providing a vacuum environment.

5. **Current Leads**: Copper current leads extending from the power supply at room temperature to the thermal shield.

6. **Support Rods**: G10 fiberglass support rods to mechanically support the solenoid.

7. **HTS Current Leads**: HTS current leads extending from the thermal shield to the solenoid.

8. **Copper Path**: A copper path providing thermal conduction between the solenoid and the cold head of the cryocooler.

# 3.2 | COMSOL Implementation

The modeling process involved defining all necessary parameters to vary the geometry and underlying physical quantities dynamically. The geometry was implemented, and the mesh was optimized, as the default physics-controlled mesh was insufficient for the required accuracy. Various physics modules were employed to simulate the solenoid's behavior. 2D-axisymmetric and 3D models were developed; the 2D model was primarily used to optimize the iron yoke and magnetic field, while the 3D model provided a comprehensive analysis of the solenoid.

## 3.2.1 | Geometry

### 3.2.1.1 | 3D Model

The 3D geometrical implementation of the solenoid in COMSOL is shown in Figure 3.1. For clarity, a surrounding sphere of air with a radius of 3 m centered at the origin is omitted. In Figure 3.2, the thermal shield is hidden to focus on the solenoid itself.

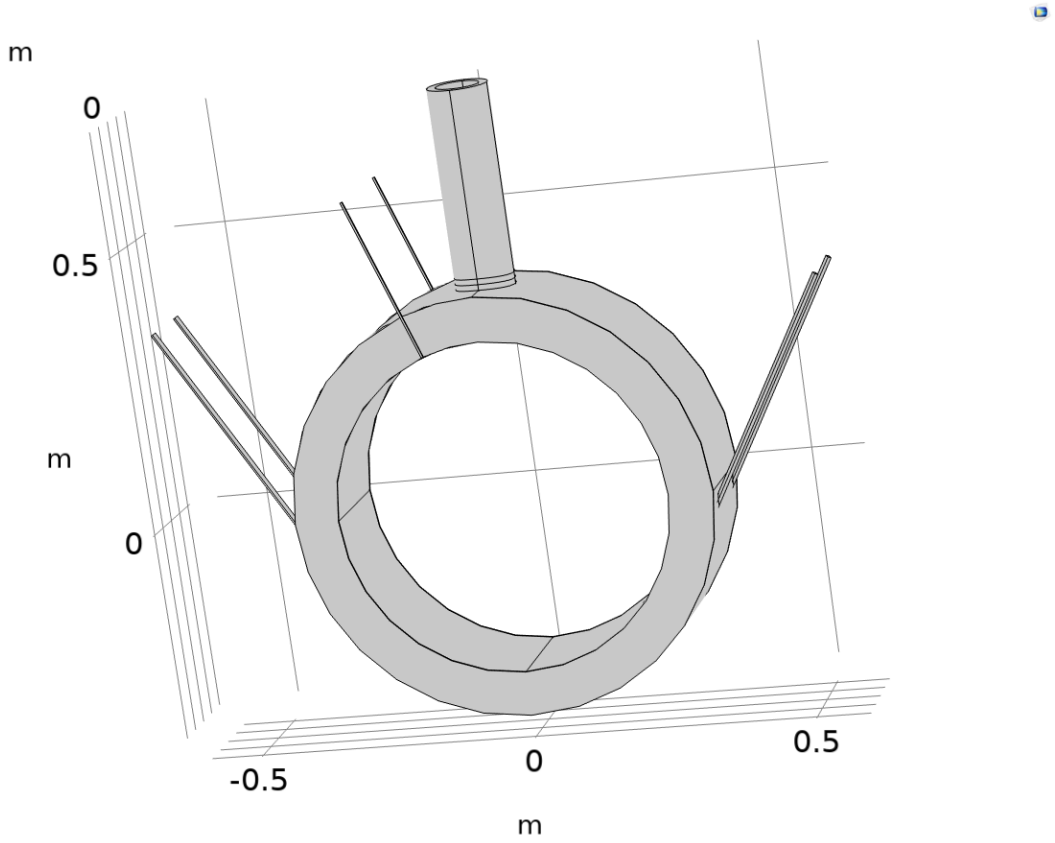


Figure 3.1: 3D model of the solenoid with the thermal shield.

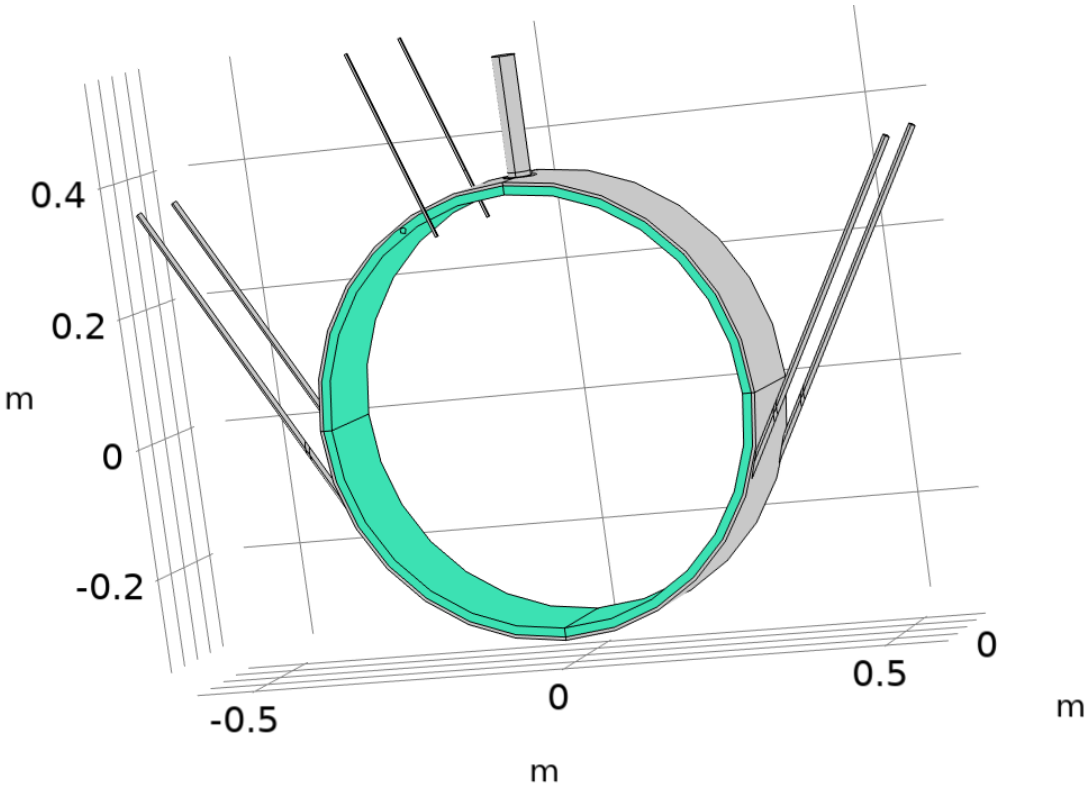


Figure 3.2: 3D model of the solenoid with the thermal shield hidden.

#### 3.2.1.2 | 2D Model

A 2D projection was used to visualize the system further. By revolving the 2D model around the central axis, the 3D model is obtained. The solenoid, copper path, thermal shield, and yoke are depicted in Figure 3.3.

A 2D axisymmetric study was used to optimize the magnetic yoke selection due to the symmetry of the problem.

### 3.2.2 | Materials

Copper was used for the thermal shield, current leads, cold head paths, and the thermal path in contact with the solenoid. G10 fiberglass was used for the support rods. The choice of materials was guided by previous work on Large Hadron Collider (LHC) solenoids [10]. Material properties, such as thermal conductivity, heat capacity at constant pressure, and thermal strain, were implemented using data available at PSI rather than the default values in COMSOL. This data was accessible due to prior projects, such as modeling the Superbend magnet for the Swiss Light Source upgrade [16]. The data is presented in Appendix B.

The NbTi wire properties were manually defined. The thermal conductivity varies depending on the radial, axial, and azimuthal directions. The anisotropic thermal conductivities were calculated using composition laws. For the HTS wire, thermal conductivities and heat capacities were extracted from the literature [57, 58].

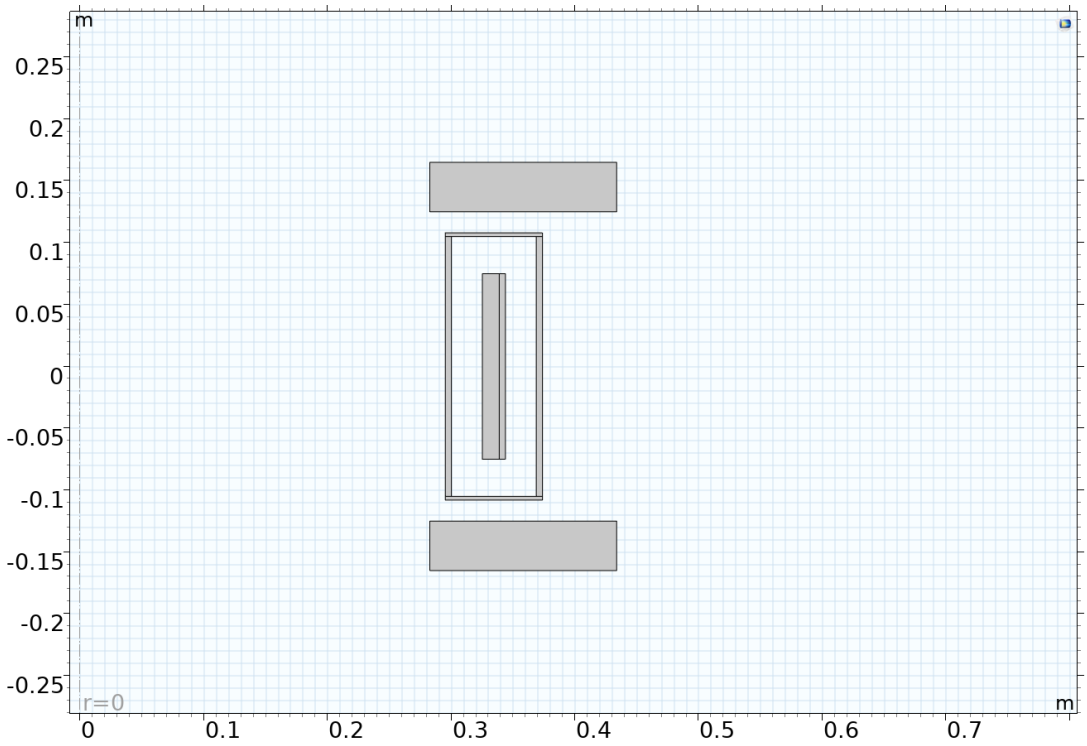


Figure 3.3: 2D model of the solenoid and surrounding components.

### 3.2.3 | Functions

Several interpolated functions were defined in COMSOL based on available literature and experimental data:

1. **Thermal Conductivities and Heat Capacities**: Functions for the thermal properties of materials used in the model.

2. **Cryocooler Capacity Curves**: Data for various cryocoolers, including:

   - RDK-305D2 two-stage Gifford-McMahon cryocooler, with a cooling capacity of 0.6 W at 4 K and 15 W at 40 K [59].
   - CH110 LT single-stage Gifford-McMahon cryocooler, with a cooling capacity of 80 W at 40 K [60].
   - RD125D single-stage Gifford-McMahon cryocooler, with a cooling capacity of 30 W at 77 K [61].

   Such cryocoolers were chosen to handle the thermal load of the superconducting system while minimizing the power consumption.

These functions allowed for accurately modeling the materials' thermal behavior and the cryocoolers' performance under varying conditions.

### 3.2.4 | Meshing

A free tetrahedral mesh was employed to capture the complex geometry [62], with distinct meshing strategies applied to different components based on their impact on simulation accuracy . The relative importance of mesh accuracy for each component was as follows:

1. **Coil**: Highest priority; a very fine mesh was necessary to resolve sharp magnetic field gradients and thermal variations.
2. **Copper thermal path**: Moderately refined, as accurate thermal distribution is important though less critical than the coil.
3. **Thermal shield**: A coarser mesh was acceptable while maintaining adequate thermal resolution.
4. **Magnetic Yoke**: Moderately refined to accurately capture its influence on the magnetic field distribution.
5. **Support rods**: Lower priority; a relatively coarse mesh sufficed since structural details were not the main focus of this study.
6. **Central Axis**: A custom edge mesh was applied to measure the field profile along the central axis accurately.
7. **Surrounding Air**: Coarsely meshed, serving mainly as a background to assess the central field.

Mesh convergence was established by progressively refining the mesh and monitoring key metrics. For the magnetic analysis, both the maximum magnetic field ($B_{\text{max}}$) and the central magnetic field ($B_{\text{central}}$) were tracked. For the thermal and quench analyses, the maximum temperature on the coil ($T_{\text{max}}$) was used as an indicator. The numerical results were validated against analytical solutions for the magnetic field and thermal budget, as discussed in the literature review.

Element quality was quantified primarily by skewness, a widely used measure that evaluates how far an element's angles deviate from those of an ideal element. For tetrahedral meshes, an ideal element is a perfect tetrahedron with equilateral triangular faces [63]. Skewness penalizes elements with large or small angles, making it particularly effective for identifying poorly shaped elements during mesh generation. The minimum skewness value for the coil and thermal shield was 0.2, well above the common threshold of 0.1. At the same time, most elements exhibited skewness values of 0.7 or higher, indicating a high-quality mesh overall.

To further validate the meshing strategy, a complementary 2D axisymmetric magnetic study featuring a parametric sweep of the coil's maximum element size was

conducted. The results from the 2D model showed excellent agreement with those of the 3D model, confirming the reliability of the meshing approach and the convergence of key parameters.

While more sophisticated methods such as adaptive mesh refinement based on error estimation or solution gradients are available [64, 65], the simplified progressive refinement approach adopted here and in the previous superconducting magnet at PSI [4] proved sufficient. The stable behavior of the monitored parameters across successive mesh refinements supports the adequacy of this approach for the present analysis, all while avoiding excessive computational overhead.

### 3.2.5 | Modules Used

The following COMSOL modules were utilized to model the superconducting solenoid accurately:

#### 3.2.5.1 | Curvilinear Coordinates Interface

Curvilinear coordinates were employed to enhance the accuracy of simulations involving anisotropic materials, where properties such as thermal conductivity vary depending on the direction relative to the material's structure.

For the superconducting solenoid, the primary application of curvilinear coordinates was to accurately define the coil material's anisotropic thermal conductivities, which vary in the radial, azimuthal, and axial directions.

The curvilinear coordinate system was established by defining the geometry of the coil where this system was applied and then providing the directions along the coil. The software then solved to find the curvilinear coordinate system at every point on the solenoid.

#### 3.2.5.2 | Magnetic Fields Module

The *Magnetic Fields* module in COMSOL Multiphysics® was used to simulate static magnetic fields and their interactions with the material environment. It solved Maxwell's equations in their magnetic vector potential form to accurately describe the magnetic field distribution within and around various geometries.

In the project, the Magnetic Fields module was utilized to perform several critical calculations for the superconducting solenoid:

- **Magnetic Field Distribution**: Computing the magnetic field distribution across the solenoid, especially focusing on the central axis, where the beam would pass through. This information was essential for ensuring that the field profile matched the requirements of the resistive solenoid.

- **Stored Magnetic Energy**: Calculating the total magnetic energy stored within the solenoid. This metric was important for assessing the quench dynamics of the solenoid due to the relationship between the magnetic energy and the coil inductance.
- **Maximum Magnetic Field Intensity**: Extracting the maximum magnetic field intensity within the solenoid to determine the corresponding critical surface. This information was crucial for evaluating the quench margin.
- **Impact of Iron Yoke**: Evaluating how an iron yoke surrounding the solenoid affected the field distribution, including assessments of changes in the maximum field and the magnetic energy due to the yoke, informing decisions on yoke geometry.

#### 3.2.5.3 | Heat Transfer Module

The *Heat Transfer* module was adept at modeling various modes of heat transfer. This capability was crucial for accurately predicting the thermal behavior of materials and systems under various conditions. Understanding and controlling the temperature distribution is essential for superconducting coils used in high-energy physics to maintain superconductivity and prevent thermal runaway conditions that lead to quenching.

A novel aspect of this study was incorporating a thermal component due to radiation deposition. Radiation from the beamline can deposit energy into the solenoid, leading to localized heating. The maximum permissible radiation dose the solenoid can withstand without quenching was determined by modeling this effect as an additional heat load.

The Heat Transfer module was utilized to perform a range of thermal analyses:

- **Cooldown Simulation**: Simulating the cooldown process of the superconducting coil from room temperature to its operational temperature. This process was crucial to ensure that the coil reached superconducting conditions reasonably.
- **Operational Temperature Analysis**: Modeling the temperature distribution across the solenoid during operational conditions, particularly focusing on the impact of having the beamline and current leads turned on.
- **Parametric Study of Radiation Effects**: Conducting a parametric study to determine how different radiation heat loads impacted the solenoid. The maximum permissible dose mimicking the maximum radiation dose was established by considering extra heat loads as a proxy for radiation.

Understanding and controlling the thermal environment of a superconducting solenoid is paramount. The heat transfer analysis ensured that the solenoid could

be operated within safe thermal limits, thus maintaining superconductivity throughout its operational regime.

#### 3.2.5.4 | Structural Mechanics Module

The *Structural Mechanics* module was used to analyze structural behavior under various mechanical loads. It allowed studying static, dynamic, and thermal stresses within engineered structures and materials.

For the superconducting coil, the Structural Mechanics module was employed to:

- **Model Displacement**: Analyze the displacement of the coil under magnetic stress and gravity, ensuring that the coil structure remains stable and functional under operational loads.
- **Assess Von Mises Stress**: Compute the von Mises stress within the coil to evaluate its mechanical integrity and prevent failure due to excessive stress under normal operating conditions.

These applications ensured that the superconducting coil could withstand the physical forces encountered during its operation, maintaining structural integrity and performance reliability.

#### 3.2.5.5 | Events Interface

The *Events Interface* in COMSOL Multiphysics® is part of the Ordinary Differential Equations and Differential Algebraic Equations (ODE and DAE) interfaces, located under the Mathematics branch. This interface was designed to handle scenarios where solver events were needed during simulation.

The Events Interface allowed for the creation of explicit or implicit events within a simulation:

- **Explicit Events**: The user specifies when the event should be triggered.
- **Implicit Events**: The event triggers when a specified condition is met, such as a specific variable reaching a threshold.

In this project, the Events Interface was employed to simulate a quench event in the superconducting coil. The simulation was set to:

- **Triggering a Quench**: The interface was configured to trigger an event when certain conditions indicative of a quench were met, such as the coil's temperature exceeding its critical threshold due to localized heating.

- **Solver Response**: Upon activation of the event, the simulation was set to modify the coil's thermal and electrical properties to reflect the superconductivity loss.

Using the Events Interface was pivotal in accurately modeling the quench dynamics, enabling a detailed study of the coil's response under critical failure conditions.

### 3.2.6 | Study Implementation

The study was implemented in the study node of COMSOL. Several studies were considered:

1. **Curvilinear Coordinates Study**: To obtain the curvilinear coordinate system for the coil.
2. **Magnetic Field Study**: To compute the magnetic field on the coil and at the central axis.
3. **Heat Cooldown Study**: To determine the temperature distribution in the solenoid without the beamline and current leads' heat loads.
4. **Heat Operational Study**: To obtain the temperature distribution in the solenoid with the beamline and current leads' heat loads.
5. **Radiation Thermal Study**: To determine the temperature distribution in the solenoid due to radiation from the beamlines.
6. **Mechanical Study**: To analyze the stress and strain in the coil.
7. **Quench Study**: To evaluate the quench margin.

All the nodes are demonstrated in Figure 3.4.

#### 3.2.6.1 | Curvilinear Coordinates Study

The curvilinear coordinates study was implemented to account for the anisotropic thermal conductivity in the coil. The `Jump` diffusion method was used to ensure smooth transitions of the curvilinear coordinate system across boundaries.

#### 3.2.6.2 | Magnetic Field Study

A 2D axisymmetric model was used to optimize the geometry for the yoke and the coil, significantly reducing computation time compared to the 3D model. The key nodes used included:

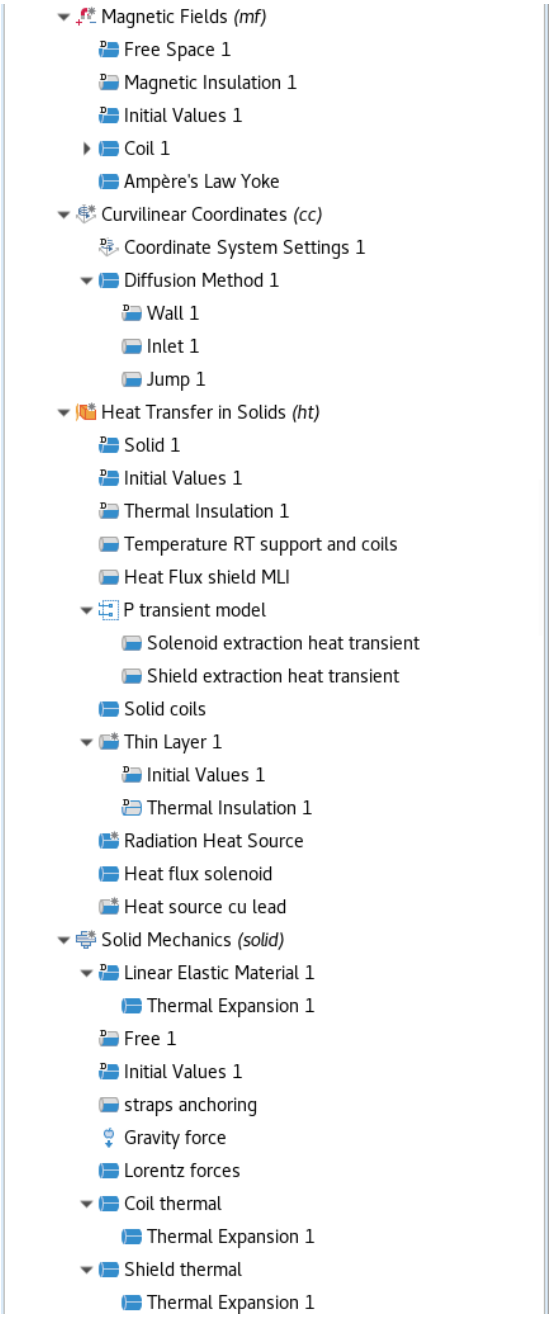


Figure 3.4: Study nodes in COMSOL Multiphysics®.

- **Free Space**: Defines regions outside the solenoid where the magnetic field is free to propagate.
- **Magnetic Insulation**: Imposes boundary conditions where no magnetic field can penetrate.
- **Initial Values**: Specifies initial values for the magnetic field.
- **Coil**: Defines the superconducting coil parameters.
- **Ampère's Law for Yoke**: Implements Ampère's Law for the magnetic yoke with a specific B-H curve.

A 3D model was also used to confirm the results of the 2D model.

#### 3.2.6.3 | Heat Transfer Studies

Several heat transfer studies were conducted:

**Heat Cooldown Study** A time-dependent simulation lasting 60 hours was used to model the solenoid's cooldown. Initial temperatures were set to room temperature, and heat loads from radiation and current leads were disabled.

**Heat Operational Study** Heat sources from the current leads were enabled. The study was time-dependent with a 5-hour duration, modeling the solenoid under operational conditions.

**Radiation Thermal Study** A novel aspect of this study was the inclusion of radiation heat loads. The *Radiation Heat Source* node was enabled to simulate how radiation from the beamline affected the thermal performance of the solenoid. As mentioned in subsection 2.3.2, such radiation thermal load approach was already used in [40–42]. However, the novel aspect of this study lies in the parameterization of the radiation dose to establish a direct relationship between the radiation dose and the maximum coil temperature. This approach aids in determining the threshold for the maximum allowable radiation dose. The study was time-dependent and lasted for 100 hours.

Previous studies [40–42] have addressed radiation-induced heat loads in solenoids for the COMET experiment at J-PARC in Japan, the MuSiC experiment at the Research Center for Nuclear Physics in Japan and the EMus project at the China Spallation Neutron Source. However, this study uniquely parametrizes radiation dose and measures coil temperature for each dose, establishing a direct relationship between dose and temperature. This approach allows for a more precise determination of thermal responses under varying radiation conditions.

The following is a comprehensive list of all the nodes:

1. **Solid 1**: Default node
2. **Initial Values 1**: Sets initial temperature values.
3. **Thermal insulation 1**: Defines boundaries that are thermally insulated. Default node.
4. **Temperature RT support**: Sets the temperature of the ends of the support to room temperature.
5. **Heat Flux shield MLI**: Applies MLI heat flux to the shield as given in the MLI catalog [15].

6. **Solid Coils**: applies the curvilinear coordinate system to the coil.
7. **Thin Layer**: applies a thin layer of epoxy between the copper path and the coil.
8. **Heat flux solenoid**: Applies MLI heat flux to the solenoid as given in the MLI catalog [15].
9. **Heat source current lead**: Applies the heat source from the current leads.
10. **Heat source radiation**: Applies the heat source from radiation.

#### 3.2.6.4 | Mechanical Study

The mechanical study imported the curvilinear coordinates to account for anisotropic material properties. Nodes utilized included:

1. **Linear Elastic Material**: Defines material properties.
2. **Free**: Specifies free boundaries.
3. **Initial Values**: Sets initial mechanical conditions.
4. **Straps Anchoring**: Defines mechanical constraints from support straps.
5. **Gravity Force**: Applies gravitational forces.
6. **Lorentz Forces**: Applies magnetic forces.
7. **Coil Thermal Expansion**: Accounts for thermal expansion or contraction of the coil material.
8. **Shield Thermal Expansion**: Similar to the previous node but applied to the thermal shield.

The thermal path in the system will be implemented using flexible copper braids. In the COMSOL simulation, it was not necessary to explicitly model this detail, as the primary focus was to evaluate the thermal resistance of the copper braids themselves, rather than their mechanical deformation due to thermal expansion.

#### 3.2.6.5 | Quench Study

The quench was implemented based on previous experience at PSI with the Superbend magnet [4]. The same nodes from the thermal study were reused, with additional nodes added:

- **Heat Source (Quench Pulse)**: A localized heat source simulating a disturbance at the most quench-sensitive region.

- **Heat Source (Joule Coil)**: Joule heating node represents the wire's resistance during quench.

Events Interface nodes included:

- **Discrete States**: Sets the initial state of the quench to be off.
- **Indicator States**: Sets the delay time and threshold voltage for quench initiation.
- **Implicit Events**: Controls the timing of the quench release based on voltage thresholds.

From the quench study, quench propagation was visualized. The hotspot temperature and peak voltage on the coil were obtained, helping to determine whether any damage would occur to the coil in the case of a quench.

## 3.3 | Magnetic Study

This section presents the calculations and analyses to determine the solenoid specifications, including the required ampere-turns, maximum magnetic fields, stored energy, critical surface analysis, and field profile matching. The magnetic parameters are summarised in Table 3.1.

Table 3.1: Summary of NbTi Solenoid Parameters. The third column indicates whether the parameter was calculated analytically or obtained from the COMSOL simulation.

| **Parameter** | **NbTi** | **Method** |
|---|---|---|
| Manufacturer | Bruker | Analytical |
| Cu:NonCu ratio | 1.35:1 | Analytical |
| Operating Temperature | 4.5 K | Analytical |
| Conductor Dimensions (width × thickness) | 1 mm × 0.6 mm | Analytical |
| Number of layers | 20 | Analytical |
| Number of turns | 2,760 | Analytical |
| Total Conductor Length | 5,800 m | Analytical |
| Cost per metre | 1 CHF | Analytical |
| Solenoid Cost | 5,800 CHF | Analytical |
| Current | 96 A | Analytical |
| Peak Magnetic Field | 0.55 T | Simulation |
| Solenoid Mass | 30 kg | Analytical |
| Field Integral | 0.310 T m | Simulation |
| Maximum Field | 1.5 T | Simulation |
| Quench Margin | 24% (3–4 K) | Simulation |
| Stored Magnetic Energy | 38 kJ | Simulation |

To achieve a peak magnetic field of $B_0 = 0.55$ T at the center of the solenoid, a configuration with a length $l = 0.15$ m, an inner radius $r_{in} = 0.65$ m, and a winding thickness $t$ ranging from 0.6 mm to 2 cm requires approximately 300,000 ampere-turns calculated using Eq. 2.1. The winding thickness was parametrically varied to optimize the design and the parameters of the solenoid. In particular the winding thickness affects the number of turns and consequenly the current and the required length of the conductor.

The final design employs a NbTi solenoid with 20 layers, optimized to minimize the heat load at the current leads, which was identified as the system's most restrictive parameter. This optimization is facilitated by the low cost of NbTi wire, priced at 1 CHF per meter. In this configuration, the solenoid achieves a maximum magnetic field of 1.5 T and stores magnetic energy of 38 kJ by integrating the field over the entire spatial volume. The maximum magnetic field refers to the field on the solenoid while the peak magnetic field of 0.55 T refers to the peak field on the central axis of the solenoid. The quench margin was calculated as described in section 2.2.1.3.

### 3.3.1 | Critical Surface Analysis

Figures 3.5a and 3.5b display the critical current density as a function of magnetic field and temperature for NbTi, respectively. A uniform current distribution was assumed and the maximum magnetic field on the solenoid was considered.

The critical surface data were extracted from CERN's measurements [8], normalized to the critical current of 1500 A at 1.5 T and 4.2 K. The data are presented in Appendix A.

The calculations show that the NbTi solenoid has a quench margin of approximately 24%, with a temperature margin of 3–4 K, providing a reasonable safety buffer. Reducing the operating current can improve these margins; however, a margin of 24% is considered sufficient for safe operation.

### 3.3.2 | Field Profile Analysis

Matching the magnetic field profile along the central axis of the superconducting solenoid to that of the existing resistive solenoid is essential to ensure consistent beam dynamics and field quality. The field integral is defined as:

$$\int_{\text{solenoid}} B \, dl, \tag{3.1}$$

Where $B$ is the magnetic field and $dl$ is the differential length along the solenoid, it serves as a key figure of merit.

Initial simulations without an iron yoke revealed significant fringe fields, resulting in a larger field integral of 0.36 T m compared to the desired 0.32 T m from the resistive

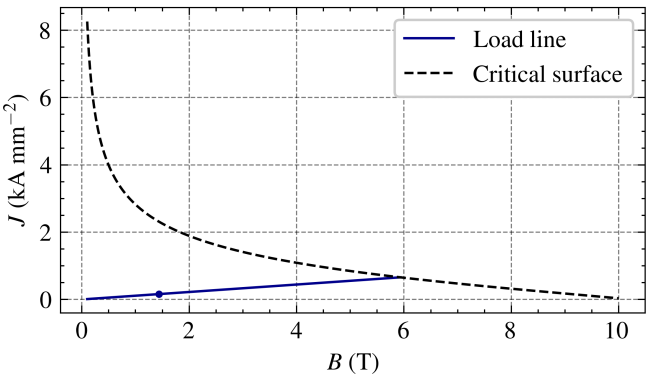


(a) Critical current density vs. magnetic field (NbTi) at 4.5 K.

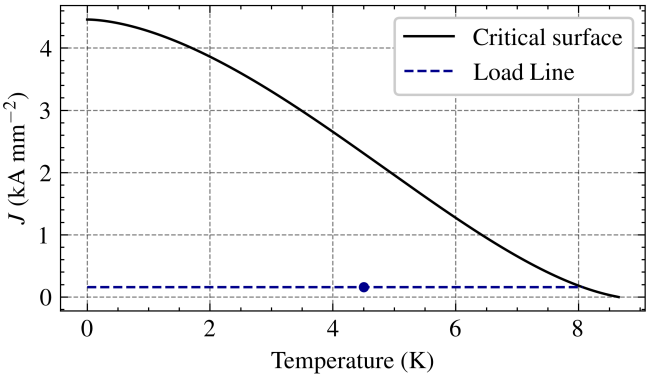


(b) Critical current density vs. temperature (NbTi) at 1.5 T.

Figure 3.5: Critical current density as a function of magnetic field and temperature for NbTi. The operating conditions are indicated with dots.

solenoid. An iron yoke made of stainless steel was implemented to reduce the fringe field. The optimized design, featuring top and bottom lids with a thickness of 5 cm and a length of 10 cm, effectively confined the magnetic field, reducing fringe effects.

Figure 3.6 illustrates the field profile comparison between the resistive solenoid and the superconducting solenoid with the iron yoke. The field integral of the superconducting solenoid was reduced to 0.31 T m, closely matching the resistive solenoid and satisfying the field quality requirements.

#### 3.3.2.1 | Iron Yoke Selection

The dimensions of the iron yoke were parametrically varied to optimize field confinement while adhering to spatial constraints within the beamline. The iron yoke consists of only the top and bottom lids, as side walls did not significantly impact the field profile. Stainless steel was chosen for its suitable magnetic properties and compatibility with cryogenic environments.

The lids were positioned as close as possible to the beamline, and their thickness

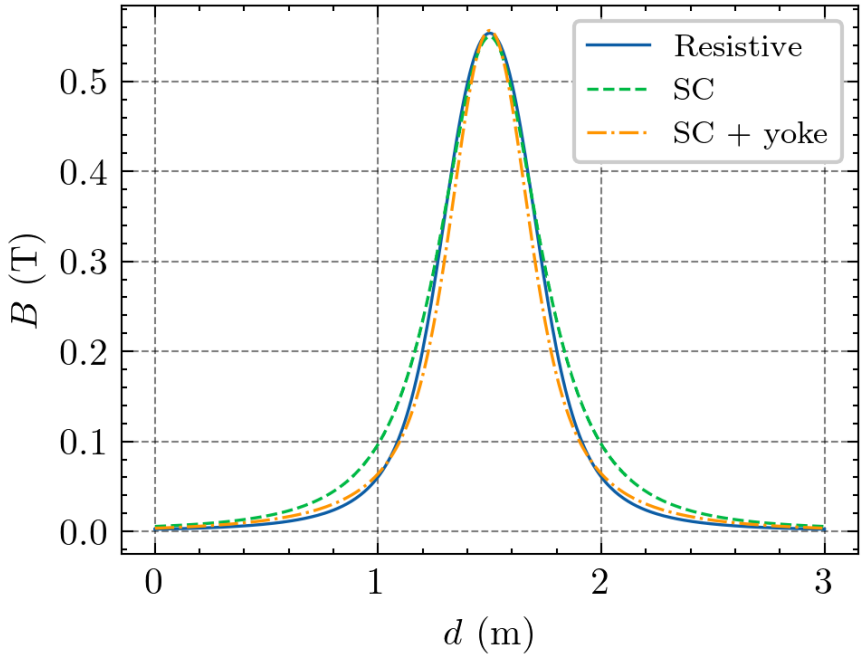


Figure 3.6: Field profile comparison between the resistive solenoid (blue) and the superconducting solenoid with iron yoke (green). Including the iron yoke reduces fringe fields and aligns the field integral with the resistive solenoid.

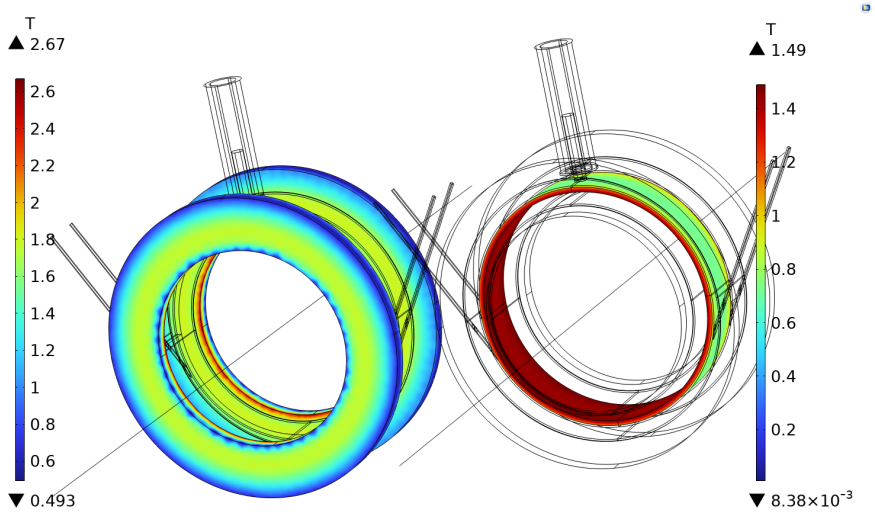


Figure 3.7: Magnetic field distribution on the magnetic yoke and the solenoid. The iron yoke effectively confines the magnetic field, reducing fringe effects and aligning the field integral with the resistive solenoid.

was increased incrementally until no substantial improvement in field confinement was observed. The final dimensions were selected based on a balance between magnetic performance and practical considerations such as available space and ease of integration into the beamline infrastructure.

The final magnetic field distribution on the magnetic yoke and the solenoid is shown in Figure 3.7.

# 3.4 | Thermal Study

Effective thermal management is crucial for maintaining the solenoids' superconducting state. This section presents the thermal analysis to ensure that the solenoids operate within safe temperature limits under various heat loads, including those induced by radiation near the target. The study involves developing a thermal budget, selecting appropriate cryocoolers, and simulating the thermal performance of a NbTi solenoid.

## 3.4.1 | Thermal Budget

Before performing thermal simulations, an analytical thermal budget was established to estimate the heat loads and aid in selecting suitable cryocoolers. The thermal budget also informed constraints on the coil currents to minimize the thermal load from the current leads. The simulation results were expected to align with the thermal budget estimates.

The heat load from radiation in the beamline significantly contributes to the thermal budget. Solenoids closer to the target receive higher radiation doses, resulting in greater heat deposition. Table 3.2 summarizes the radiation dose rates and corresponding power deposition for NbTi solenoids at different positions along the beamline. Figure 1.2 outlines the relative position within the beamline. The beam dynamics team calculated the dose rates using FLUKA simulations, with special credit to Dr. Vadim Talanov. Based on discussions with the team, it is assumed that the power is deposited uniformly over the surface of the solenoids.

Table 3.2: Radiation dose rates and power deposition for NbTi solenoids at different positions along the MuH2 beamline.

| Position | Number of Solenoids | Dose Rate (mGy/s) | Power (W) |
|---|---|---|---|
| A | 2 | 800 | 23.88 |
| B | 3 | 4.2 | 0.127 |
| C | 6 | 0.2 | 0.005 |

Table 3.3 presents the estimated heat loads for the first and second cooling stages. These values were calculated as described in section 2.2.2.

Data analysis in Table 3.2 indicates that the heat load on solenoid A is too high for practical cooling at 4.2 K. Cryocoolers capable of extracting such heat loads at this temperature are not energy-efficient and contradict the project's goal of reducing overall power consumption. Therefore, the NbTi solenoid was considered primarily for positions with lower radiation doses (Positions B and C).

A suitable cryocooler for the NbTi solenoid is the Sumitomo RDK-305D2 two-stage cryocooler, which consumes 3.6 kW of power. Its cooling capacity at the desired operating temperatures (4.5 K at the second stage and 77 K at the first stage) is sufficient

Table 3.3: Heat load components for the NbTi solenoid.

| **Heat Source** | **Power [W]** |
|---|---|
| **1st Stage** | |
| Current Leads (95 A) | 9.0 |
| Structural Supports | 1.2 |
| Thermal Radiation (2 W m$-^2$) | 1.6 |
| Sensor Wires | 0.3 |
| **Total 1st Stage** | **12.1** |
| **2nd Stage** | |
| HTS Leads | 0.04 |
| Structural Supports | 0.12 |
| Thermal Radiation (0.2 W/m$^2$) | 0.13 |
| Sensor Wires | 0.15 |
| Neutron Radiation (position B) | 0.13 |
| **Total 2nd Stage** | **0.57** |

to handle the estimated heat loads, as shown in Figure 3.8. This cryocooler was chosen as it has one of the lowest power consumptions among the 4.2 K cryocoolers available on the market. All the cryocooler curves were extracted from the manufacturer's website and incorporated into the COMSOL model to accurately determine the cooling capacity at each temperature.

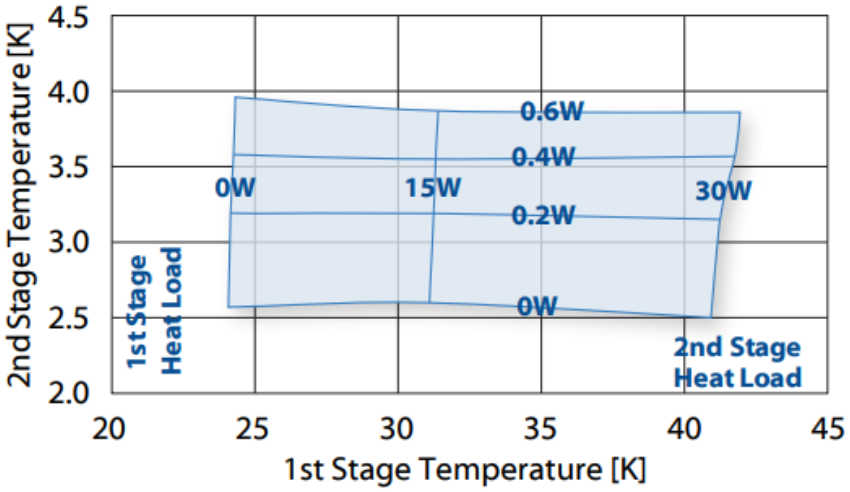


Figure 3.8: Cooling capacity of the Sumitomo RDK-305D2 cryocooler at various temperatures.

## 3.4.2 | Initial Cooldown

The initial cooldown simulation involved cooling the solenoid and thermal shield without any heat load from the current leads. The temperature distribution after the

cooldown is shown in Figure 3.9a, and the temperature evolution over time is presented in Figure 3.9b.

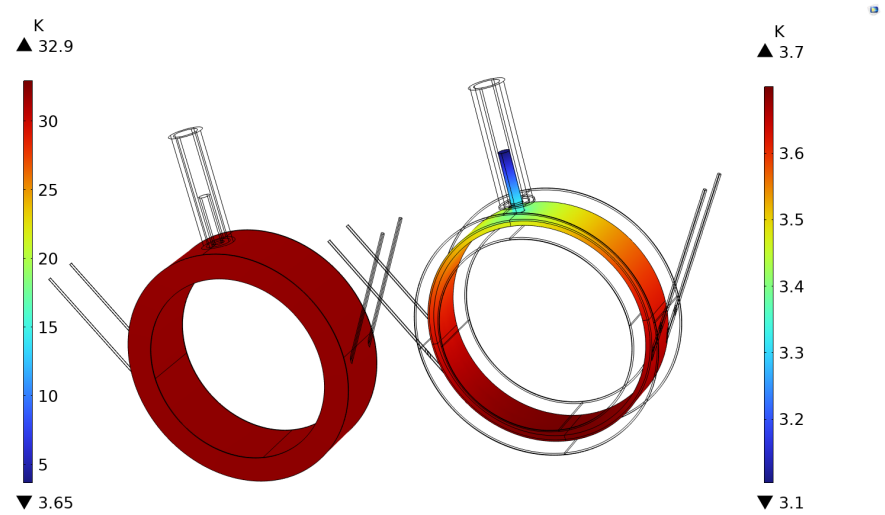


(a) Temperature distribution after initial cooldown.

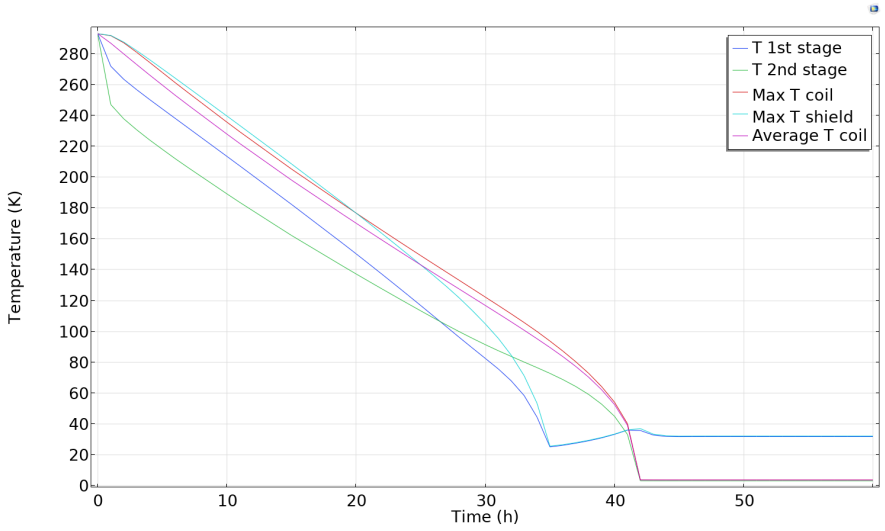


(b) Temperature evolution during initial cooldown.

Figure 3.9: Initial cooldown of the NbTi solenoid and thermal shield.

The cooldown time to reach steady-state conditions is approximately 45 hours, which is acceptable given the beamline's continuous operation schedule.

A copper thermal path was included to enhance heat conduction from the cryocooler to the solenoid, compensating for the lower thermal conductivities in the radial and azimuthal directions of the coil. Without the copper path, higher temperatures are observed, as shown in Figure 3.10.

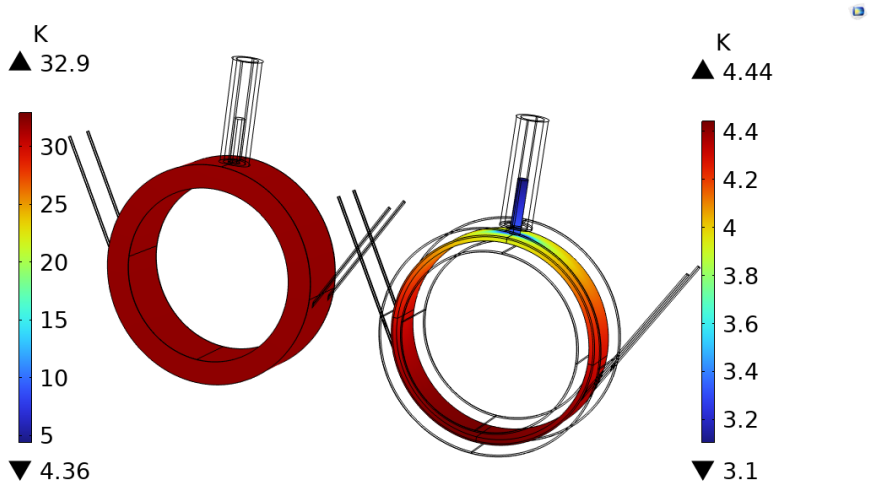


Figure 3.10: Temperature distribution without the copper thermal path, showing higher temperatures in the solenoid.

### 3.4.3 | Steady-State Operation

After the initial cooldown, the heat load from the current leads was introduced to simulate regular operation. The steady-state temperature distribution is shown in Figure 3.11a, and the temperature evolution is presented in Figure 3.11b.

Due to the additional heat load, the thermal shield experiences a slight temperature increase, but the superconducting coil's temperature remains stable and well below the critical temperature.

### 3.4.4 | Radiation Heat Load Analysis

The radiation dose was varied in the simulation to determine the maximum radiation heat load that the NbTi solenoid can tolerate without exceeding the current-sharing temperature. Figure 3.12 shows the maximum coil temperature as a function of the radiation heat load.

The results indicate that the NbTi solenoid can handle a maximum radiation heat load of approximately 1 W. This is significantly lower than the heat load at Position A (approximately 24 W), suggesting that an NbTi solenoid is unsuitable for this location without substantial radiation shielding.

In theory, one can also use several cryocoolers to extract 24 W at 4 K. For instance, 24 RDK-305D cryocoolers can be used, but this would lead to two critical showstoppers:

- The power consumption rises from 3.6 kW to $3.6 \times 24 = 86.4$ kW, more than the resitive magnet.
- Each cryocooler costs at least 30 kCHF, so 24 cryocoolers would cost 720 kCHF.

Such a solution is impractical, and an HTS solution is required.

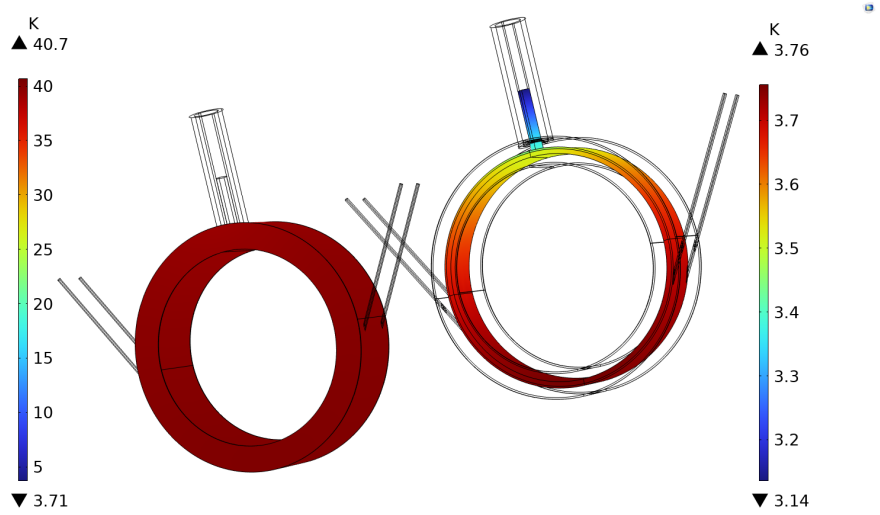


(a) Temperature distribution during steady-state operation.

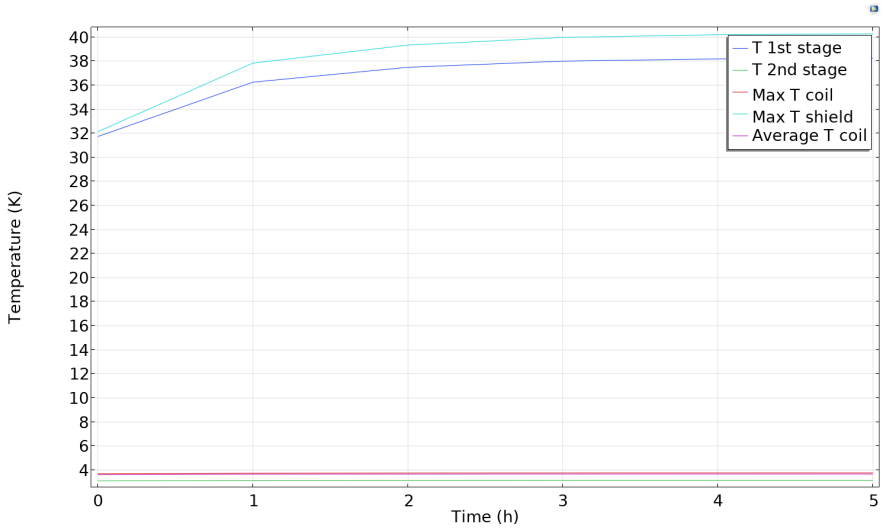


(b) Temperature evolution during steady-state operation.

Figure 3.11: Steady-state operation of the NbTi solenoid and thermal shield.

**Radiation Shielding Requirements** Using K-resin as a neutron radiation shield, with an effective removal cross-section of $\lambda = 0.2\ \mathrm{cm}^{-1}$, the required shielding thickness $t$ to reduce the radiation levels by a factor of $f$ is given by [43]:

$$t = -\frac{\ln f}{\lambda}. \tag{3.2}$$

To reduce the radiation levels by a factor of 30, the required thickness is:

$$t = -\frac{\ln(30)}{0.2\ \mathrm{cm}^{-1}} \approx 20\ \mathrm{cm}. \tag{3.3}$$

Due to space constraints in the beamline, incorporating such thick shielding is impractical.

**Summary** The thermal analysis demonstrates that the NbTi solenoid suits positions with lower radiation heat loads (Positions B and C). Still, it cannot handle the high heat

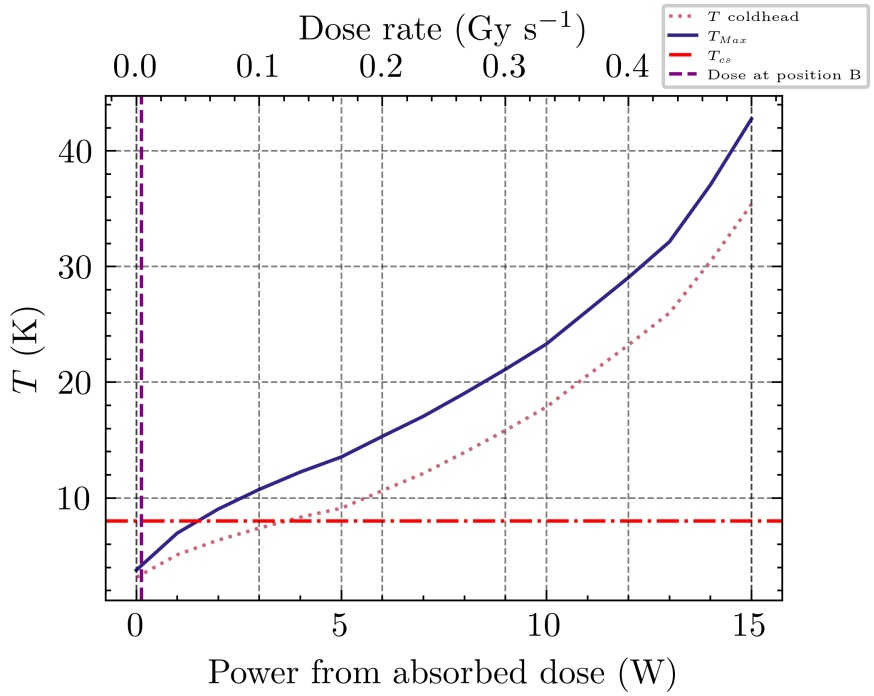


Figure 3.12: Maximum coil temperature as a function of radiation heat load for the NbTi solenoid.

loads at Position A without impractical radiation shielding.

## 3.5 | Mechanical Study

Mechanical resilience is essential to ensure the solenoids maintain structural integrity under operational stresses, including electromagnetic forces and thermal contractions. Given the relatively light mass of 30 kg and a field of 1.45 T, no mechanical issues were expected.

The von Mises stress distributions for the NbTi solenoid and thermal shield are shown in Figure 3.13. The maximum von Mises stress was 18 MPa, well below the allowable stress limit of 200 MPa [6]. The thermal shield and support structures also exhibited stresses significantly below their respective material limits.

Mechanical displacements were calculated to assess potential deformations affecting the solenoid's performance or alignment. The maximum displacement was less than 0.1 mm, occurring at the outer edges of the coil. Such minimal displacement is considered negligible and is unlikely to impact the operation of the solenoid.

Mechanical simulations indicate that the solenoid has adequate strength and stiffness to endure the operational stresses encountered during beamline operation. The calculated von Mises stresses and displacements are considerably below the material limits, ensuring structural integrity and reliable performance.

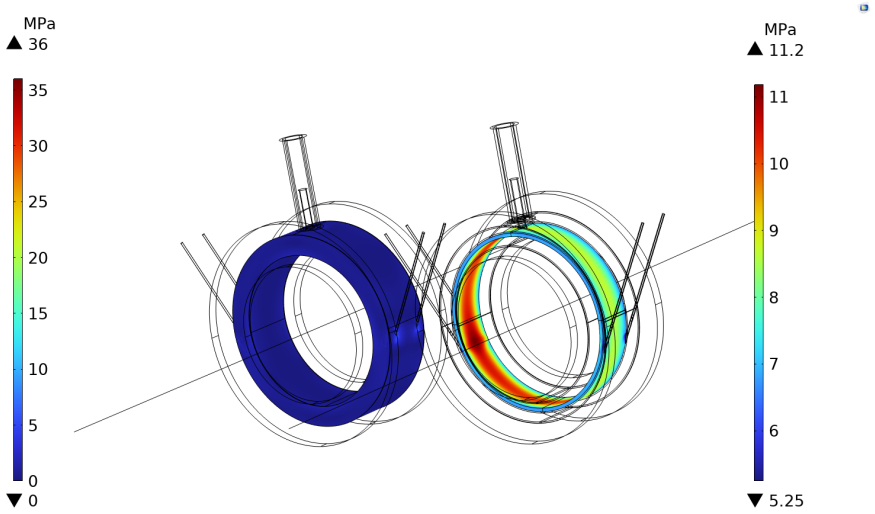


(a) Von Mises stress distribution in the NbTi solenoid and thermal shield.

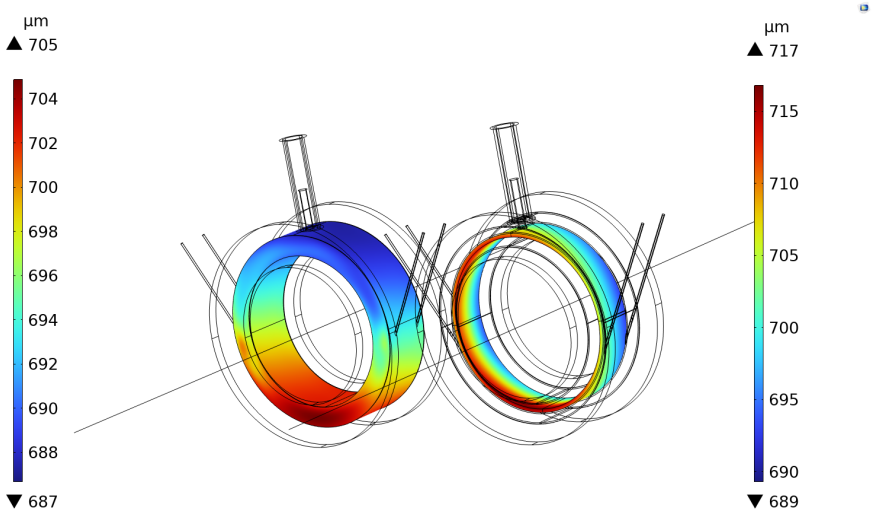


(b) Mechanical displacement in the NbTi solenoid and thermal shield.

Figure 3.13: Mechanical simulation results for the NbTi solenoid: (a) von Mises stress distribution, (b) mechanical displacement. The results indicate that stresses and displacements are within acceptable limits.

## 3.6 | Quench Analysis

As mentioned in section 2.2.4, an external dump circuit is implemented to protect the solenoid from quench events. This section presents the analytical calculations and numerical simulations performed to assess the quench behavior of the solenoid, including the maximum temperature and voltage during a quench.

The quench parameters are:

- Operating temperature: $T_{\text{op}} = 4.5$ K,
- Maximum magnetic field: $B_{\text{max}} = 1.5$ T,
- Operating current: $I_0 = 96$ A,
- Operating current density $J_{\text{op}} = 159$ A mm$^{-2}$,
- Inductance: $L = 8.3$ H,
- Dump resistor: $R_{\text{dump}} = 3.5\ \Omega$,
- Quench detection time: $t_{\text{d}} = 100$ ms,
- Voltage limit: $V_{\text{max}} = I_0 R_{\text{dump}} = 336$ V.

The time constant of the discharge circuit is:

$$\tau = \frac{L}{R_{\text{dump}}} = \frac{8.3\ \text{H}}{3.5\ \Omega} \approx 2.371\ \text{s}. \tag{3.4}$$

Assuming an exponential decay of current, the MIITS value is approximated as:

$$\text{MIITS} = J_0^2 \left(t_{\text{d}} + \frac{\tau}{2}\right) \approx 32700\ \text{A}^2\text{s m}^{-4}. \tag{3.5}$$

Using the calculated MIITS value of approximately 22776 A$^2$s, Wilson's integral yields a maximum temperature:

$$T_{\text{max}} \approx 95\ \text{K}. \tag{3.6}$$

This temperature is below the critical temperature limits of the conductor and insulation materials, ensuring safe operation and avoiding damage to the magnet components.

The MIITS calculation provides a conservative estimate of $T_{\text{max}}$ because it assumes worst-case conditions, such as instantaneous quench propagation, uniform energy deposition throughout the conductor, and neglecting heat removal during the quench. These assumptions ensure sufficient safety margins in the magnet design.

During a quench, the voltage across the dump resistor ($V_{\text{max}} = 336$ V) represents the maximum voltage that the external protection circuit must handle. In contrast, the voltage across the coil during the quench is influenced by the internal resistance

development and inductive effects, which typically result in lower voltages within the coil. Similarly, the temperature distribution within the coil may differ from the analytical estimate due to non-uniform quench propagation and localized cooling effects.

### 3.6.1 | Quench Simulation

To obtain a more detailed understanding of the quench behavior, a simulation was performed using COMSOL Multiphysics. The simulation incorporates the coupled electromagnetic and thermal phenomena during a quench, accounting for the spatial and temporal evolution of temperature and resistance within the coil.

The summary of the simulation results, including the current decay, resistive voltage $IR_{\text{coil}}$ across the coil, temperature rise, and magnetic field evolution, is shown in Figure 3.14.

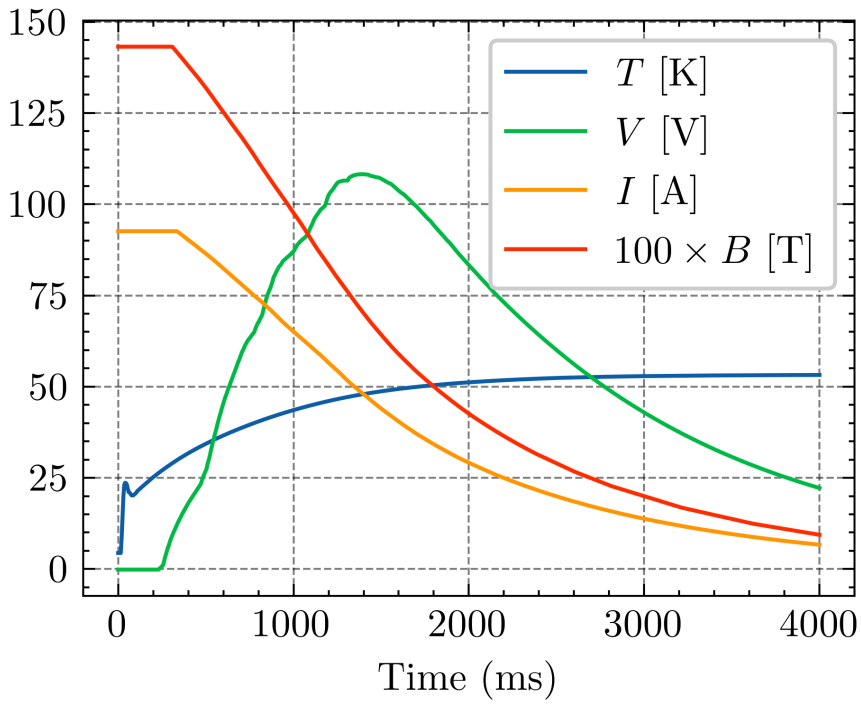


Figure 3.14: Quench simulation results in COMSOL: (a) Current decay over time, (b) Resistive voltage across the coil, (c) Temperature distribution showing hotspot, (d) Magnetic field evolution during the quench.

Key findings from the simulation are:

- The hotspot temperature reached approximately 55 K, significantly lower than the 95 K estimated from the MIITS calculation.
- The maximum resistive voltage across the coil was below 150 V. The maximum total voltage across the coil is the initial voltage across the dump resistor $V_{\text{max}} = I_0 R_{\text{dump}} = 336$ V. as described by Eq. 2.12.

The analytical MIITS calculation and the numerical simulation provide a comprehensive understanding of the quench behavior in the NbTi solenoid. The MIITS method ensures that the design includes sufficient safety margins by estimating the worst-case scenario. The simulation confirms that, under realistic conditions, the maximum temperature and voltage are lower than the conservative estimates.

In conclusion, the NbTi solenoid is adequately protected against quench events, with both analytical and simulation results demonstrating safe operation within material limits.

## 3.7 | Radiation Damage

Radiation damage to superconducting coils is primarily caused by neutron radiation in the beamline, as outlined in the literature review. The neutron spectrum, crucial for precise damage assessment, was unavailable due to the PSI beam dynamics team's current focus on the SLS2.0 upgrade. However, based on existing radiation dose data, significant damage is expected at position A, where the dose is highest. For positions B and C, the radiation impact decreases substantially by factors of 200 and 1000, respectively, with further downstream solenoids experiencing negligible radiation.

Neutron radiation degrades the critical current and the critical temperature of superconducting tapes. For the NbTi solenoid, a margin of 24% allows a 76% reduction in critical current, corresponding to greater than $3 \times 10^{22}$ high-energy neutrons as seen in Figure 2.3.

### 3.7.1 | Cryocooler Damage

Consultations with cryocooler manufacturers (Sumitomo and Cryomech) revealed no existing radiation damage data for cryocoolers. The superconducting system's design places the cryocooler away from the beamline to minimize radiation exposure, particularly to the seals, which are most susceptible.

This placement introduces challenges, notably the need for a longer thermal path between the cryocooler and the coil, resulting in higher coil temperatures due to energy loss in cooling the extended path. A copper path was chosen for this analysis. Still, future designs could benefit from PHPs, which offer thermal conductivity an order of magnitude higher than copper, reducing the temperature gradient. Research on this technology is ongoing, with one team at PSI currently exploring its use for HTS magnet cooling.

## 3.8 | Conclusion

The simulation results confirm that the NbTi superconducting solenoid is well-suited for integration into the HIMB beamline at positions with manageable radiation-induced heat loads. It meets the magnetic field specifications, maintains acceptable quench and temperature margins, and demonstrates structural integrity under operational stresses. Thermal analyses indicate that, with appropriate cryocooling solutions, the NbTi solenoid can reliably operate at positions B and C, thereby enhancing the facility's energy efficiency and performance.

However, the high radiation-induced thermal loads at position A exceed the cooling capabilities of the NbTi solenoid, making it impractical due to the excessive number of cryocoolers or shielding required. This limitation highlights the necessity for alternative solutions capable of withstanding such demanding conditions without compromising efficiency. The current design at this position involves radiation-hard resistive magnets using mineral-insulated cables[2, 3].

To address these challenges, the adoption of HTS technology, specifically utilizing YBCO magnets, becomes essential for position A. HTS magnets offer higher thermal stability and can tolerate greater radiation-induced heat loads, addressing the challenges faced by NbTi solenoids at this location. Their implementation ensures operational feasibility while maintaining the desired magnetic performance and advancing the energy efficiency objectives of the HIMB facility.

In conclusion, while NbTi solenoids are effective and practical for most positions along the HIMB beamline, the extreme conditions at position A necessitate using HTS magnets. The next chapter will delve into the design and performance of HTS solenoids in high-radiation environments, focusing on their capacity to meet the stringent requirements at position A and further advancing the HIMB facility's energy efficiency objectives.

# 4

# Simulation and Implementation of a YBCO Solenoid

This chapter explores the implementation and performance of a YBCO magnet within the high-radiation environment of Position A on the MuH2 beamline. Operation of LTS deemed unsuitable for this location due to excessive heat loads, compromising their operational feasibility. To address these challenges, adopting HTS technology, specifically YBCO, is essential for achieving the required thermal stability and performance in high-radiation conditions.

This research incorporates the layer winding of a YBCO magnet prototype at PSI as a practical component. This winding technique reduces the number of soldered joints, thereby minimizing heat load and enhancing the magnet's reliability compared to pancake winding methods. However, layer winding introduces hard way bending, presenting its challenges, as detailed in Section 2.4. The developed prototype serves as a foundation for future demonstrators at PSI, which will empirically assess radiation-induced damage in HTS solenoids and further validate the efficacy of layer winding in high-radiation environments.

## 4.1 | Magnetic Results

This section evaluates the magnetic performance of the YBCO solenoid through simulations conducted using COMSOL Multiphysics. The maximum magnetic field and magnetic energy were calculated following the methodology established in the previous chapter. The total length and number of turns were minimized to optimize conductor costs. The minimum number of turns was found by analyzing the critical surface of the YBCO tape. The optimal configuration was determined to consist of 20 layers with a total of 1,000 turns, as summarized in Table 4.1. This configuration achieves a peak magnetic field of 2.05 T and a field integral while maintaining a quench margin of 70% and operating at 30 K, thereby ensuring enhanced thermal stability suitable for high-radiation environments. A magnetic yoke is once again considered to reduce the stray field. The critical surface data for the YBCO tape, obtained from manufacturer specifications [66] and presented in Appendix A, are illustrated in Figure 4.1. These plots depict the critical current density as a function of magnetic field and

temperature, with operating conditions indicated by markers. The YBCO solenoid demonstrates a substantial quench margin of approximately 70% and a temperature margin of 15 K, highlighting its superior thermal stability compared to NbTi.

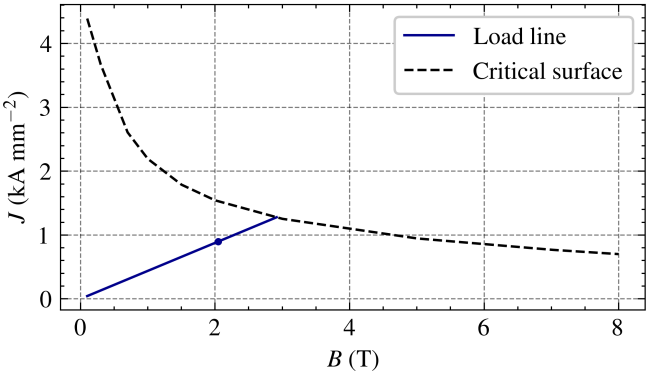


(a) Critical current density vs. magnetic field (HTS) at 30 K.

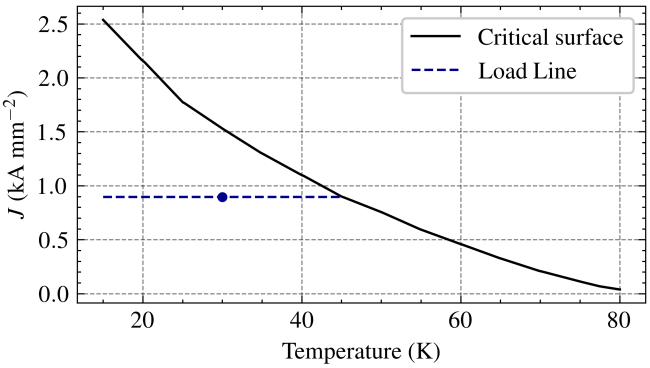


(b) Critical current density vs. temperature (HTS) at 2.05 T.

Figure 4.1: Critical current density as a function of magnetic field and temperature for YBCO. The operating conditions are indicated with dots.

## 4.2 | Thermal Study

### 4.2.1 | Thermal Budget

For the HTS solenoid, which operates at a higher temperature of 30 K, two single-stage cryocoolers were considered:

- **CH-110LT Cryocooler**: Used to cool the HTS coil to 30 K.
- **RD-125D Cryocooler**: Used to cool the thermal shield and current leads to 77 K.

The thermal budget for the HTS solenoid is similar to that of the NbTi solenoid presented in Table 3.3, with adjustments for the higher operating current of 270 A and the associated heat load from the current leads (approximately 25 W). The estimated heat load at the first stage is around 28 W. The capacity curves for the selected cryocoolers are shown in Figure 4.2.

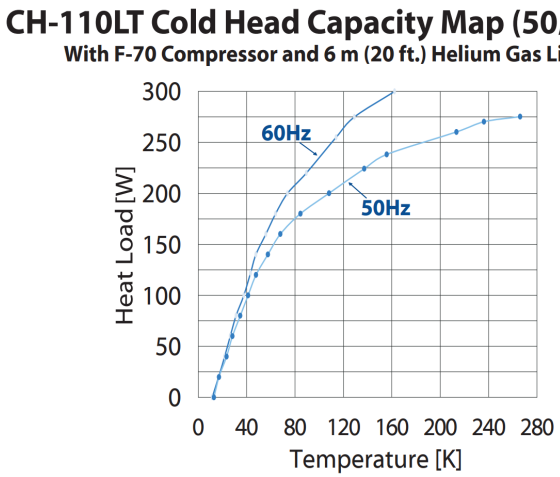


(a) Cooling capacity of the CH-110LT cryocooler.

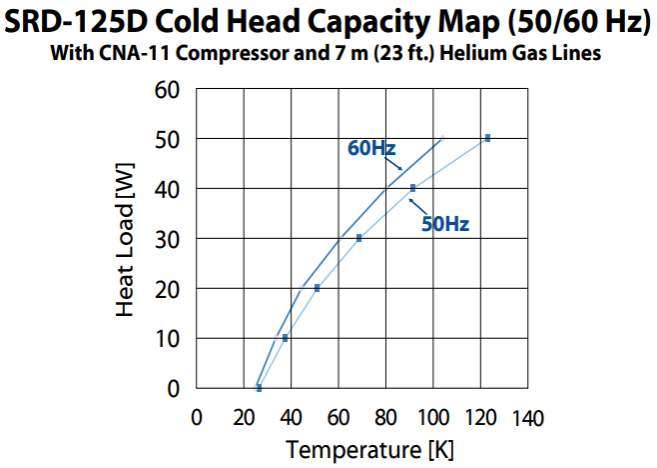


(b) Cooling capacity of the RD-125D cryocooler.

Figure 4.2: Capacity curves for the selected cryocoolers for the HTS solenoid.

### 4.2.2 | Initial Cooldown

The initial cooldown of the HTS solenoid is shown in Figure 4.3b. The cooldown time is about 35 hours. The temperature distribution after the cooldown is presented in Figure 4.3a.

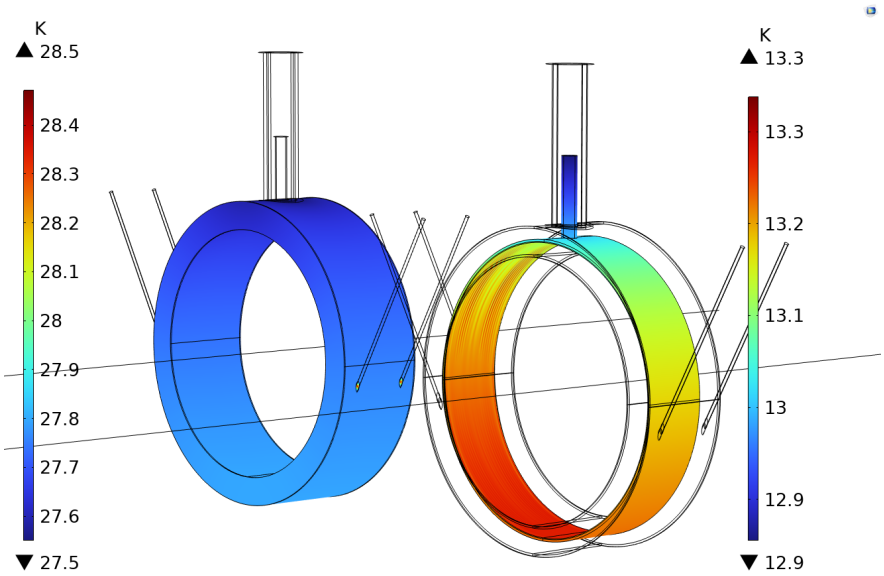


(a) Temperature distribution after initial cooldown.

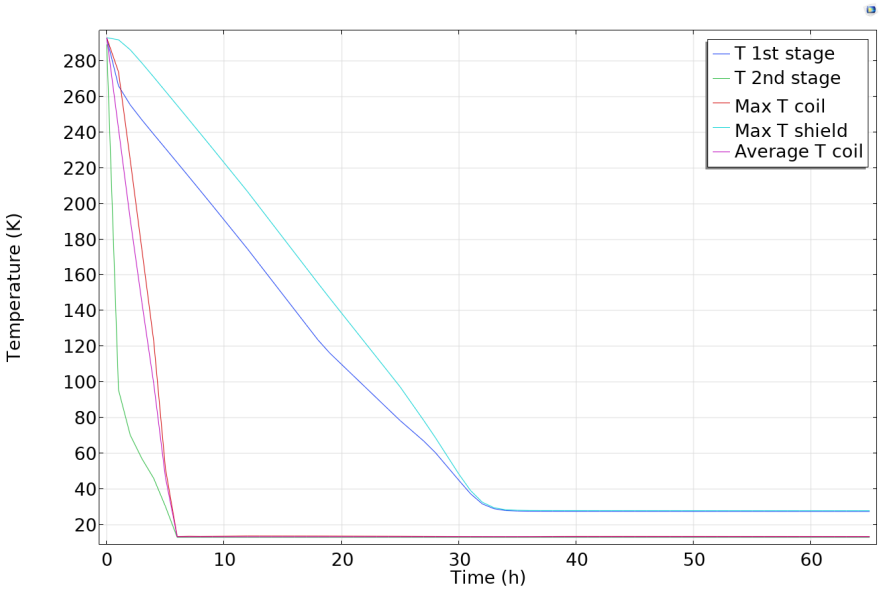


(b) Temperature evolution during initial cooldown.

Figure 4.3: Initial cooldown of the HTS solenoid and thermal shield.

### 4.2.3 | Steady-State Operation

During steady-state operation at Position A, the YBCO HTS solenoid effectively manages the elevated heat load associated with the high-radiation environment. Figure 4.4 illustrates the solenoid's temperature distribution and its thermal shield during operation.

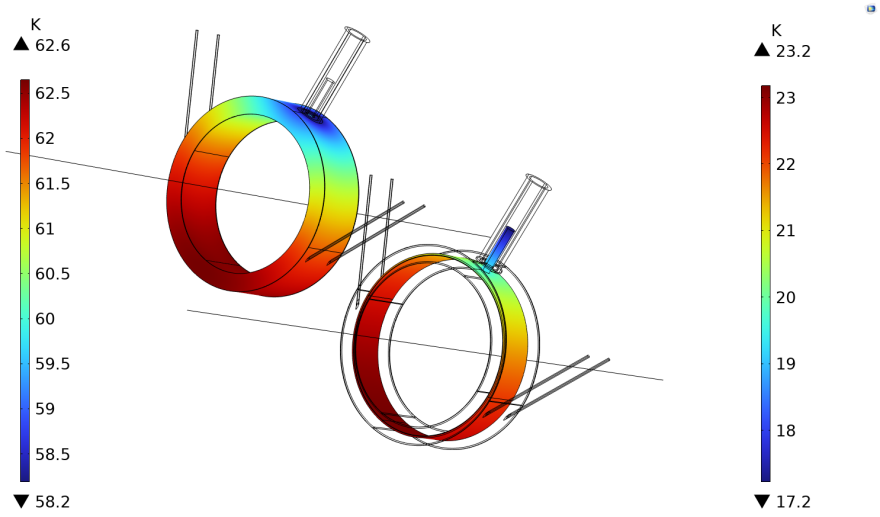


Figure 4.4: Temperature distribution on the HTS solenoid and thermal shield at Position A during steady-state operation.

As shown in Figure 4.4, the coil temperature remains well below the critical temperature of YBCO, indicating robust thermal stability under increased heat loads. This thermal performance confirms that the HTS solenoid can withstand the demanding conditions at Position A without compromising its superconducting properties.

The YBCO solenoid's ability to maintain low temperatures despite the heightened thermal demands is a significant achievement. It validates the HTS technology's effectiveness in high-radiation environments and supports the feasibility of deploying such solenoids within the MuH2 beamline. These findings are pivotal as they strongly justify further research and development of YBCO magnets, particularly focusing on enhancing their resilience and efficiency in similar high-radiation operational settings.

### 4.2.4 | Radiation Heat Load Analysis

The maximum allowable radiation heat load for the HTS solenoid was determined by varying the dose rate in the simulation. The dose rate is provided by the beam dynamics team. The total power deposition is obtained by multiplying the dose rate by the mass of the solenoid. Figure 4.5 shows the maximum coil temperature as a function of the radiation heat load.

As seen in Figure 4.5, the HTS solenoid can tolerate radiation heat loads up to approximately 30 W, corresponding to a dose rate of about 3 Gy/s, without exceeding

Table 4.1: Summary of HTS YBCO solenoid parameters.

| **Parameter** | **HTS (YBCO)** |
|---|---|
| Manufacturer | Fujikura FYSC |
| Conductor Dimensions (width × thickness) | 3 mm × 0.1 mm |
| Number of layers | 20 |
| Number of turns | 1000 |
| Total Conductor Length | 2,050 m |
| Cost per metre | 23 CHF |
| Coil Cost | 47,000 CHF |
| Peak Magnetic Field | 0.55 T |
| Current | 270 A |
| Coil Mass | 5 kg |
| Maximum Field | 2.05 T |
| Number of Turns | 1,000 |
| Operating Temperature | 30 K |
| Quench Margin | 70% (15 K) |
| Stored Energy | 39 kJ |

Table 4.2: Radiation dose rates and power deposition for HTS solenoids at different positions along the beamline. *N* refers to the number of solenoids.

| **Position** | *N* | **Dose Rate (Gy/s)** | **Mass (kg)** | **Power (W)** |
|---|---|---|---|---|
| A | 2 | 0.7960 | 10 | 7.96 |
| B | 3 | 0.0042 | 10 | 0.042 |
| C | 6 | 0.0002 | 10 | 0.002 |

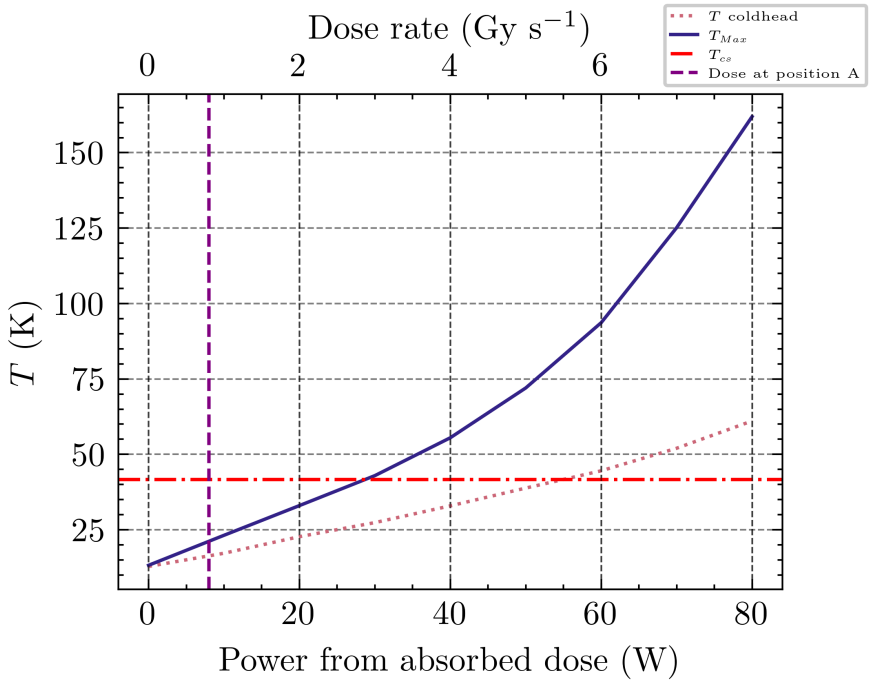


Figure 4.5: Maximum coil temperature as a function of radiation heat load for the HTS solenoid.

the critical temperature. This maximum dose rate is significantly higher than the dose rate of 0.7960 Gy/s at Position A, indicating that the HTS solenoid can operate safely in this environment. Therefore, a HTS solenoid is advantageous in the high-radiation environment as more heat can be extracted by a single cryocooler if the operational temperature is increased.

**Insulation Material Concerns** A critical issue with the HTS solenoid is the radiation-induced degradation of the epoxy insulation. The total dose limit for epoxy is approximately 20 MGy. The operational time before reaching this limit can be calculated as:

$$t = \frac{20 \times 10^6 \text{ Gy}}{\text{Dose Rate (Gy/s)} \times 3600 \text{ s/h}}. \tag{4.1}$$

At a dose rate of 0.7960 Gy/s, the operational time is:

$$t = \frac{20 \times 10^6}{0.7960 \times 3600} \approx 6,998 \text{ hours}. \tag{4.2}$$

Assuming an annual operation of 4,000 hours, the insulation would degrade after approximately 1.75 years, which is insufficient for long-term operation.

**Alternative Insulation Solutions** Alternatives to epoxy insulation must be considered to address the issue with the insulation. Potential solutions include:

- **Radiation-Resistant Materials**: Using insulation materials with higher radiation tolerance.
- **Metal-Insulated Coils**: Employing metal insulation layers (e.g., stainless steel or aluminum) between turns.
- **Non-Insulated Coils**: Designing coils without inter-layer insulation, relying on the inherent resistance of the superconducting tape to limit current sharing.

Further research and development are required to implement the HTS magnet effectively in a high-radiation environment. To address this, PSI plans to deploy a YBCO magnet in the high-radiation zone of the HIMB beamline to collect radiation damage data on the magnet.

Using the layer winding technique, a prototype will be fabricated at the PSI Magnet Development Laboratory. The prototype will then be tested to evaluate critical current degradation caused by hardway bending during layer transitions. These tests will validate the layer winding method, ensuring its suitability for future radiation damage assessments at HIMB.

## 4.3 | Magnet Winding

This section details the design, fabrication, and testing of an HTS YBCO magnet at the PSI Superconducting Magnet Development Laboratory. The work focuses on fabricating a non-insulated, layer-wound HTS magnet and analyzing its performance. This contributes to advancing HTS magnet technology at PSI.

### 4.3.1 | Facilities and Expertise at PSI

#### 4.3.1.1 | Superconducting Magnet Development Laboratory

The Magnet Development Laboratory at PSI specializes in the fabrication of superconducting magnets. Equipped with precision winding machines and tension control systems, it enables the precise fabrication of HTS coils using YBCO tapes.

#### 4.3.1.2 | Cryogenics Laboratory

The Cryogenics Laboratory provides essential infrastructure for testing superconducting magnets at cryogenic temperatures. It facilitates the validation of magnet performance, critical current measurements, and assessment of material properties under operational conditions. A photograph of the Cryogenics Laboratory is shown in Figure 4.6.


Figure 4.6: Cryogenics Laboratory at PSI.

### 4.3.2 | HTS Tape Characterization

The HTS tape utilized in this project is a 12 mm wide YBCO tape supplied by THEVA Dünnschichttechnik GmbH [67]. The key specifications are summarized in Table 4.3.

Table 4.3: Manufacturer specifications for THEVA 12 mm HTS tape.

| **Parameter** | **Value** |
|---|---|
| Tape Width | 12 mm |
| Tape Thickness | 0.1 mm |
| Critical Current ($I_c$) at 77 K, Self-field | >600 A |
| Minimum Bend Radius | 3 cm |
| Price per Meter | 90 CHF |

The HTS tape sample was prepared to ensure accurate, critical current measurements and maintain the superconducting material's integrity. The preparation process included the following steps:

1. **Cutting**: The HTS tape was precisely cut to the desired length using specialized tools to minimize mechanical stress.
2. **Soldering Connections**: Copper blocks were soldered to both ends of the tape to serve as mechanical supports and electrical connections. A low-temperature solder was employed to prevent thermal damage.
3. **Thermal Insulation**: A layer of G10 fiberglass was placed between the copper blocks to minimize heat transfer to the HTS sample along its length.
4. **Double-Tape Configuration**: To reduce current density and enhance thermal management, a second HTS tape was soldered parallel to the first tape near the copper blocks, creating a double-tape region.
5. **Voltage Taps**: Voltage taps were attached to the copper blocks using low-temperature tin-lead solder for accurate voltage measurements.

The prepared sample shown in Figure 4.7 was then immersed in liquid nitrogen to cool it down. Superconductivity was verified by passing a small current and observing the voltage drop as the temperature decreased. The critical current ($I_c$) was determined by gradually increasing the current until a voltage threshold indicated the onset of resistance. Multiple measurements were conducted to ensure accuracy and repeatability.

### 4.3.3 | Burning the Tape

To emphasize the critical importance of quench protection systems, an experiment was performed where the quench protection was intentionally disabled. The current was

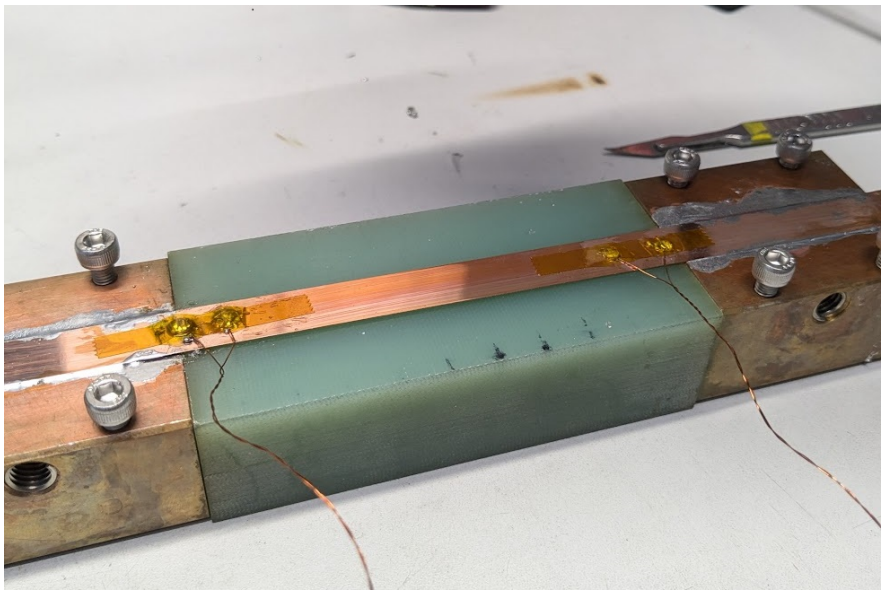

Figure 4.7: HTS tape sample setup with copper blocks, G10 insulation, and voltage taps.

incrementally increased beyond the critical current, resulting in the tape burning at approximately 850 A. This experiment demonstrated the catastrophic failure that can occur without proper protection measures.

Figure 4.8: Photograph of the burnt HTS tape after exceeding critical current without quench protection.

The burnt HTS tape, as shown in Figure 4.8, highlights the severe damage caused by surpassing the critical current without adequate quench protection. This underscores the necessity of incorporating robust quench detection and protection systems in HTS magnet designs to prevent irreversible damage.

### 4.3.4 | Winding of the HTS Magnet

The design of the HTS coil focused on several key factors to ensure optimal performance and mechanical stability:

- **Coil Geometry**: Utilized a cylindrical mandrel with a 25 cm diameter to prevent overbending of the tape and minimize mechanical stresses during layer transitions.
- **Winding Configuration**: Configured the coil with two layers, each comprising three turns, totaling six turns. This setup tested the layer winding method and its mechanical stability.
- **Tape Orientation**: Positioned the superconducting side of the HTS tape radially outward to reduce mechanical strain during winding.
- **Voltage Tap Placement**: Strategically placed four voltage taps at the current entrance (Segment 12), before and after the layer transition (Segment 23), and at the current exit (Segment 34) to monitor performance and detect quench onset.
- **Double-Tape Implementation**: Soldered an additional HTS tape parallel to the main tape near the current entrances to lower current density and mitigate heating effects.

The winding process was conducted in the Magnet Development Laboratory at PSI, following established procedures to ensure precision and repeatability based on the previous R&D experience at PSI. The key steps involved in the winding process are detailed below:

- **Machine Setup**: Adjusted the winding machine to securely hold the 25 cm mandrel, ensuring it was thoroughly cleaned with alcohol before use.
- **Tension Control**: Applied manual tension to the HTS tape for uniform winding.
- **Layer Transition**: Carefully managed the transition from the first to the second layer to minimize mechanical stress on the tape.
- **Voltage Tap Integration**: Attached voltage taps at designated locations during the winding process.
- **Current Lead Connections**: Connected current leads using copper blocks with indium layers to ensure reliable electrical contact.

The winding setup is shown in Figure 4.9. For completeness, the YBCO tape and the stainless steel tape are shown. For this experiment, the stainless steel tape was not wound.

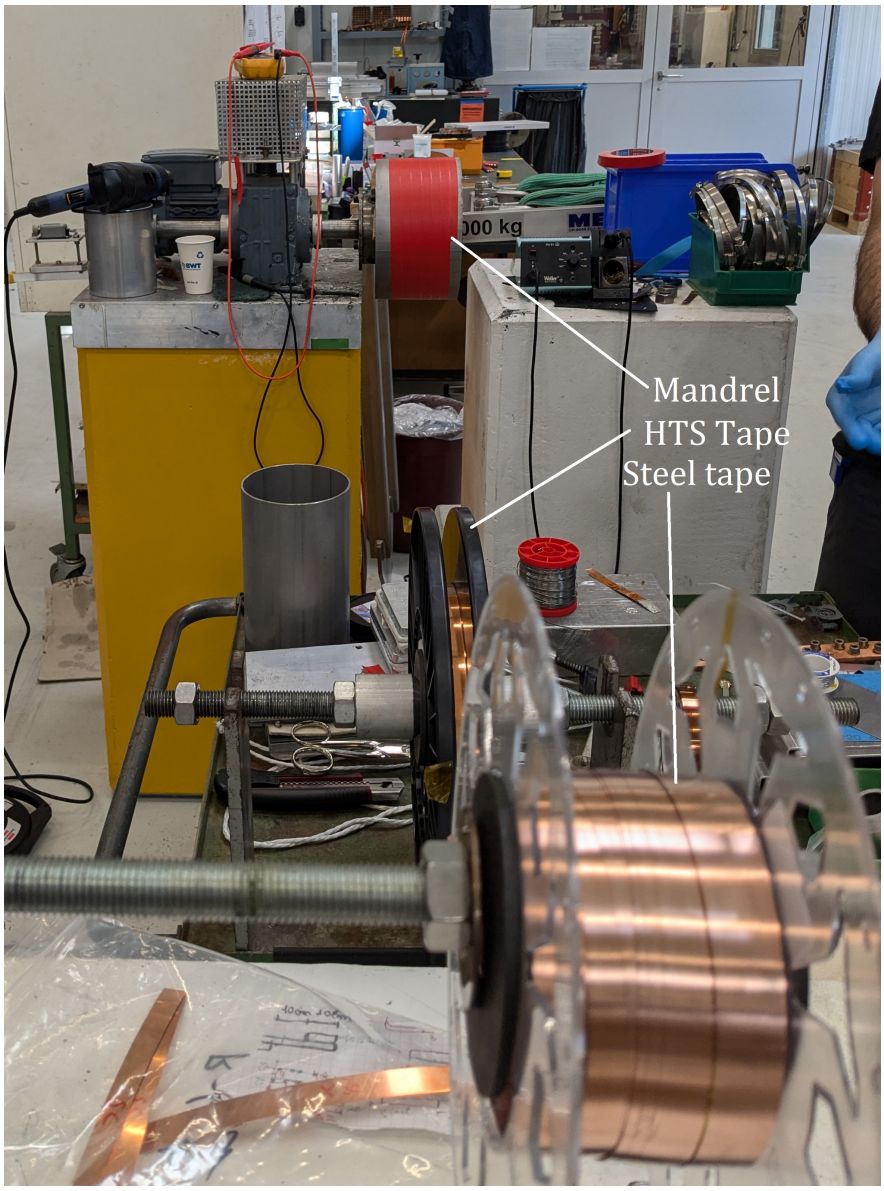


Figure 4.9: Winding of the HTS tape onto the mandrel.

**Magnet Technical Specifications** The wound HTS magnet's key technical specifications are outlined in Table 4.4. The maximum magnetic field $B_{\text{max}}$ of 0.13 T was calculated using COMSOL simulations, assuming a peak current of 600 A as specified by the manufacturer. Figure 4.10 illustrates the magnetic field distribution within the HTS coil.

**Final Design** The final design of the HTS magnet, ready for testing, is depicted in Figure 4.11a. The coil is positioned inside the cryogenic bath, with white blocks under the current leads providing mechanical support to prevent stress on the fragile HTS tape. The current leads are then connected to the copper blocks, and the coil is submerged in liquid nitrogen for testing, as shown in Figure 4.11b.

Table 4.4: HTS coil parameters.

| **Parameter** | **Value** |
|---|---|
| Number of Layers | 2 |
| Total Number of Turns | 6 |
| Inner Diameter | 25 cm |
| Height | 36 mm |
| Total Length of Tape | 4.71 m |
| Maximum Magnetic Field ($B_{max}$) | 0.13 T |

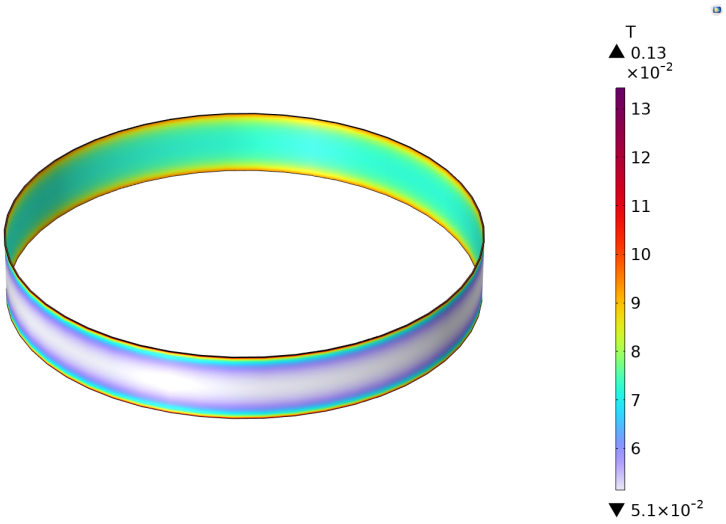


Figure 4.10: Magnetic field distribution in the HTS coil.

(a) Final design of the HTS magnet ready for testing.

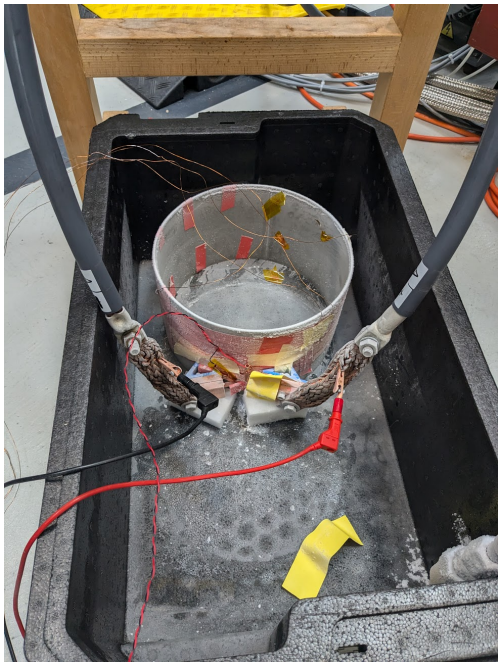

(b) Test setup in the Cryogenics Laboratory for testing the HTS coil.

Figure 4.11: (a) Final design of the HTS magnet ready for testing. (b) Test setup in the Cryogenics Laboratory for testing the HTS coil.

## 4.3.5 | Testing and Results

### 4.3.5.1 | Critical Current Measurements of the HTS Tape Sample

The voltage-current ($V$-$I$) behavior of the HTS tape sample is presented in Figure 4.12. The critical current ($I_c$) is identified when the voltage transitions from negligible to an exponential increase. The critical current is approximately 540 A, slightly below the manufacturer's specification of >600 A, likely due to tape degradation from factors such as exposure to high temperatures or mechanical stress. After discussions with the cryogenics lab technician, the precise cause of degradation could not be determined as the YBCO tapes are sensitive to various factors, namely tape degradation while winding, voltage taps soldering, copper terminals clamping and the critical current drop due to the magnetic field.

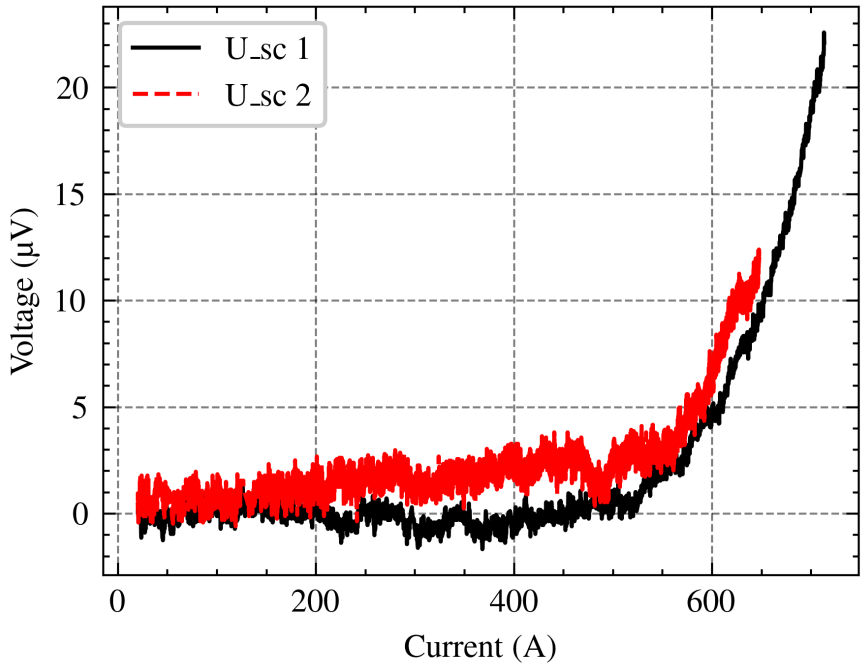


Figure 4.12: Voltage-current behavior of the HTS tape sample at 77 K. Multiple measurements demonstrate consistency across trials.

To further investigate the tape's behavior beyond its critical current, the quench protection system was intentionally disabled. The current was increased until the tape failed, resulting in burning at approximately 850 A, as depicted in Figure 4.8. This experiment underscores the critical importance of quench protection in preventing catastrophic failure.

### 4.3.5.2 | Initial Testing and Observations

Initial tests on the wound HTS coil revealed challenges with the voltage tap connections. A miscommunication regarding the soldering technique resulted in connections that

were not entirely secure, leading to intermittent disconnections during testing. As a temporary measure, crocodile clips were used to maintain connectivity; however, their use introduced additional resistance and affected signal stability.

The crocodile clips were placed at three locations - the current entrance, the layer transition, and the current exit - to measure the voltage across the HTS tape.

A resistive voltage was observed between the current entrance and the layer transition (segment 1) due to solder joint resistance, but not between the layer transition and the current exit (segment 2). The resistive behavior resulted in a quadratic $V$-$I$ curve as shown in Figure 4.13. The red curve shows the 2nd-degree polynomial that was fitted to the voltage-current curve, and the actual voltage in the superconducting segment 1 was obtained by subtracting the fitted curve from the measured voltage.

Despite this numerical fix, the coil reached 300 A before the quench protection system was triggered, potentially due to voltage spikes from boiling liquid nitrogen, shifting of the crocodile clips, or damage in the tape. This issue necessitated further investigation and corrective measures to ensure reliable performance.

#### 4.3.5.3 | Issues Encountered and Solutions Implemented

To address the observed issues, the following actions were taken:

- **Voltage Taps**: Properly soldered at the four designated locations to ensure reliable connections.
- **Thermal Management**: Applied Kapton tape to cover the second copper block and used indium between the copper block and HTS tape. Indium smoothens the rough copper surface, ensuring good thermal and physical contact. Kapton tape electrically insulates the copper block opposite the current leads, as the block was solely mechanical support. These suggestions were based on the experience of the cryogenics lab technician who's had similar issues with the YBCO tape characterization in the past.

#### 4.3.5.4 | Subsequent Testing and Observations

After implementing the fixes, the coil was retested. Resistive behavior between the current entrance and the first layer transition was observed, indicating a broken segment. Figure 4.14 shows the abnormal resistive behavior where segment 12 exhibits a direct proportionality to the current, implying resistance, while segments 23 and 34 remain superconducting.

Inspection revealed a kink in the HTS tape near the current entrance, causing mechanical damage (Figure 4.15). The damaged 10 cm section was removed, and

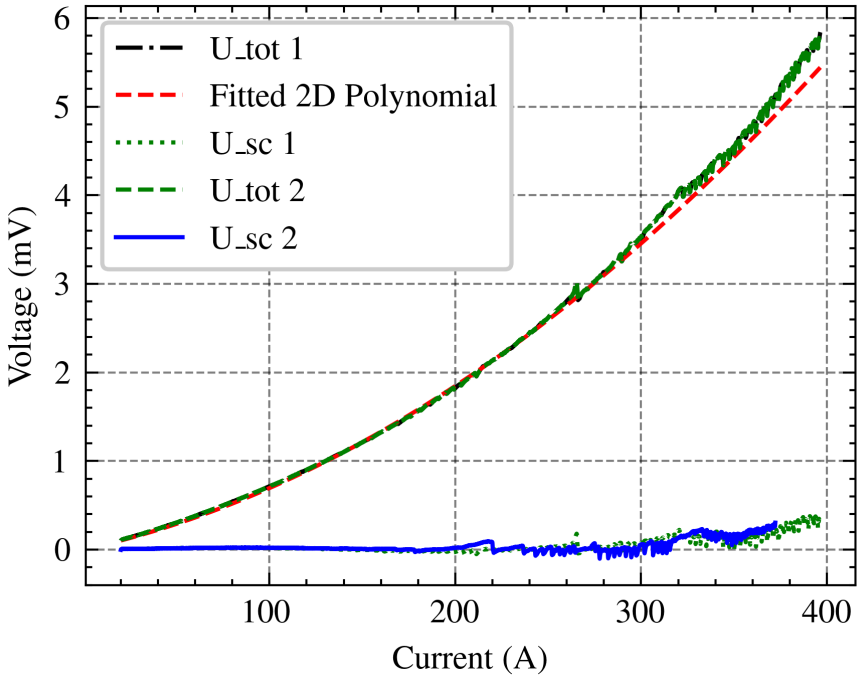


(a) Raw voltage-current data of the HTS coil during initial tests.

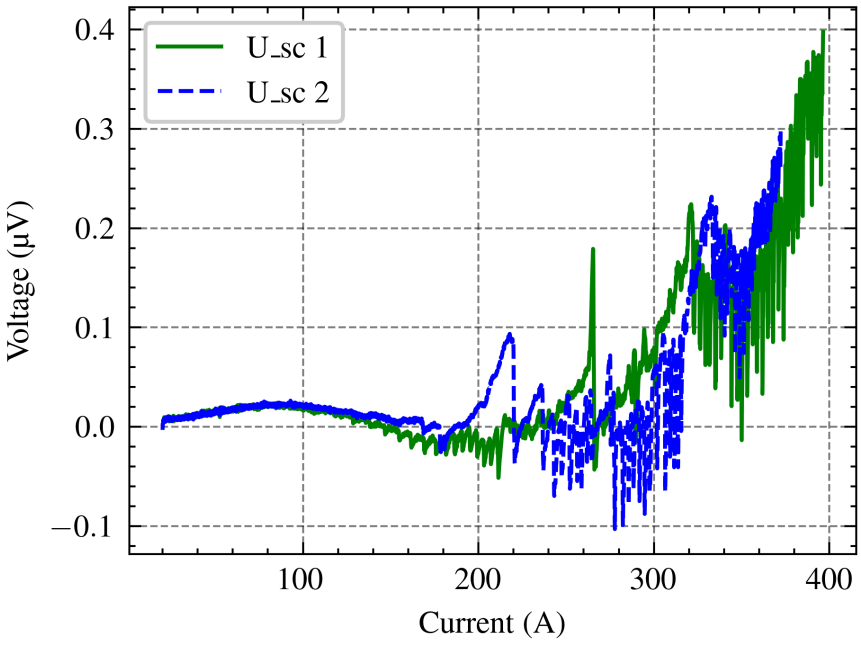


(b) Adjusted voltage-current curve after subtracting the resistive voltage.

Figure 4.13: Voltage-current behavior of the HTS coil during initial tests.

the double-tape configuration was resoldered. The coil was then retested to evaluate performance.

This experiment showed the fragility of the YBCO tape, as a slight bending led to the complete deterioration of the superconductivity. This kink was only discovered after the first test, as the tape was wound in a way that the kink was not visible. The kink waslikely caused by the weight of the copper connections that bent the tape and permanently damaging it.

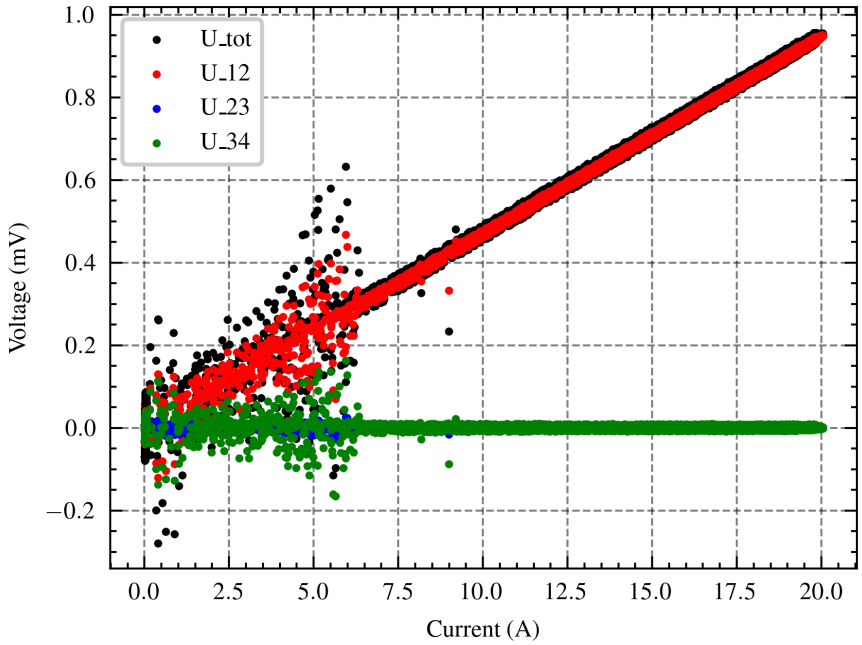


Figure 4.14: Resistive behavior observed in the HTS coil due to a damaged segment.

#### 4.3.5.5 | Final Testing and Results

Post-repair testing showed significant improvements:

- **Resistive Voltage Eliminated**: The resistive voltage between the first and second layers was no longer present.
- **Consistent Superconducting Behavior**: The $V$-$I$ curves in Figure 4.16 displayed the expected superconducting behavior, with a clear transition at the critical current for segment 34, which to recall is the segment after the layer transition and before the current exit.
- **Reliable Quench Point**: By removing the damaged tape the original performance of the coil was restored. Repeated readings confirmed that the quench consistently occurred at approximately 500 A in segment 34, verifying measurement reliability.

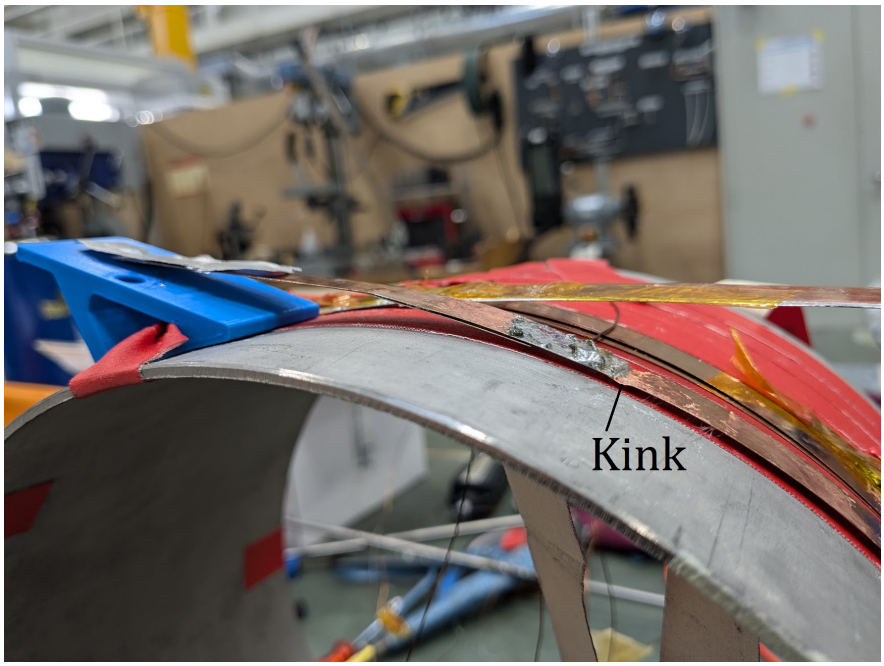


Figure 4.15: Kinked HTS tape near the current entrance.

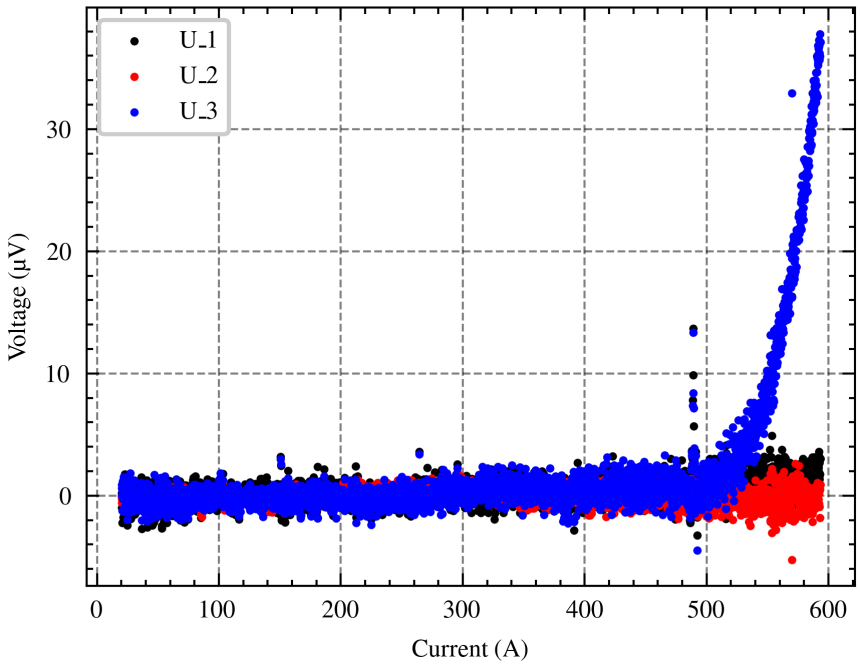


Figure 4.16: Voltage-current curve of the repaired HTS coil after removing resistive voltage effects.

The superconductivity in segment 23, spanning the layer transition, remained intact up to the manufacturer's specified current of 600 A. This indicates that the layer transition did not contribute to resistive behavior, suggesting that layer winding is a viable method for future HTS coil designs, offering advantages over the pancake winding method, as discussed in the literature review.

## 4.4 | Conclusion

This chapter investigated the implementation and performance of a YBCO HTS magnet within the high-radiation environment of Position A on the MuH2 beamline at PSI. Due to excessive heat loads, LTS like NbTi were deemed unsuitable for this location, necessitating the adoption of HTS technology to achieve operational feasibility.

Through simulations using COMSOL Multiphysics, incorporating radiation-induced thermal effects, the YBCO magnet demonstrated the ability to maintain thermal stability and magnetic performance under the expected radiation levels. This validates its potential application in Position A. A layer-wound YBCO magnet prototype was fabricated to enhance practical feasibility at PSI. This winding technique reduces the number of soldered joints, minimizing heat loads and improving reliability compared to pancake winding methods despite introducing challenges like hard way bending.

The successful fabrication and initial testing of the layer-wound YBCO magnet confirm its viability for high-radiation applications where thermal loads from radiation significantly contribute to the thermal budget. This prototype lays the groundwork for future demonstrators at PSI, which will empirically assess radiation-induced damage in YBCO solenoids. By using this winding technique, PSI aims to develop more resilient and efficient superconducting magnets, advancing the energy efficiency and performance of the HIMB facility.

The next chapter will present an economic comparison of using HTS and LTS magnets in the HIMB facility, providing insights into superconducting technology's cost-effectiveness and long-term benefits.

# 5

# Economic and environmental analysis

Transitioning from traditional resistive magnets to superconducting magnets within the HIMB beamline necessitates thoroughly evaluating economic and environmental implications. This chapter delves into the comparative analysis of capital and operational costs, life cycle assessments of $CO_2$ emissions, and potential energy savings associated with superconducting versus resistive magnet systems. This chapter aims to comprehensively understand the feasibility, sustainability, and long-term benefits of adopting superconducting technology in HIMB.

The chapter is structured as follows: Section 5.1 discusses the capital costs associated with superconducting and resistive magnet installations, including personnel expenses outlined in section 5.1.1. The life cycle assessment of the superconducting system is presented in section 5.2, focusing on $CO_2$ emissions. Section 5.3 quantifies the potential energy savings from adopting superconducting magnets. The economic implications of transitioning to superconducting systems are explored in section 5.4, followed by an environmental analysis in section 5.5. Finally, section 5.6 outlines the PSI directorate's decision based on the comprehensive analyses conducted in this chapter.

## 5.1 | Capital Costs

The initial costs of the superconducting system are presented in Table 5.1, based on data from the PSI P3 project [5], where a similar superconducting system is employed.

In evaluating the capital costs of the superconducting system, components such as the cryostat, vacuum pump, cryocooler, instrumentation, and a 20% contingency were considered, totaling 240 kCHF. This estimate excludes the cost of the magnet winding material and the power supply and installation costs, which are comparable to those of resistive magnets. Notably, resistive magnets often require more powerful and expensive power supplies due to their higher power consumption.

Maintenance costs for both systems were also considered. For superconducting systems, the cryocooler's cold head is maintained in-house every 10,000 hours, while the compressor is serviced by the manufacturer every 30,000 hours (approximately 7.5 years, assuming 4,000 hours of annual operation). Although compressor maintenance

Table 5.1: Initial and maintenance costs of the superconducting system based on PSI data.

| **Type** | **Cost (kCHF)** |
|---|---|
| Cryostat | 120 |
| Cryocooler | 30 |
| Vacuum Pump | 20 |
| Power Supply | 50 |
| Instrumentation | 30 |
| Installation | 30 |
| **Total** | **280** |
| Total w/o Power supply and installation | 200 |
| Contingency (20%) | 240 |

costs are not negligible, they are comparable to the costs of replacing water hoses and connections in resistive magnets, which can be labor-intensive, especially in radioactive environments. Given this comparability, maintenance costs were excluded from the analysis.

The cost of the magnet is taken as the cost of the required material, assuming in-house winding at the MagDev facility at PSI. If the magnet production is outsourced, as was done for the SLS2 project, the costs would increase significantly due to service charges. The superconducting SLS2 Superbend [4] cost approximately 700 kCHF. Nevertheless, the extra costs are analyzed in section 5.1.1.

For the NbTi magnet, one meter of material costs 1 CHF. With a total coil length of 5,800 m, the magnet material cost is 5,800 CHF. For the YBCO magnet, a 12 mm wide tape costs 92 CHF per meter, and a 3 mm tape costs 23 CHF per meter. This data is available from the previous orders of the PSI Magnet team. Therefore, the price of the tape scales linearly with its width. The total length of the coil is 2,050 m, leading to a magnet material cost of 47,000 CHF.

An additional cryocooler is required for the YBCO system, as mentioned in Section 4.2, costing an extra 30,000 CHF. The total capital costs for both configurations are shown in Table 5.2. Maintenance costs are deemed comparable to those of the resistive magnets and are therefore excluded from the analysis.

Table 5.2: Capital costs of different systems. NTS and RTS refer to normal and radiation-hard transport solenoids, respectively.

| **Component** | **NbTi** [kCHF] | **YBCO** [kCHF] | **NTS** [kCHF] | **RTS** [kCHF] |
|---|---|---|---|---|
| System | 240 | 270 | 100 | 225 |
| Material | 5.8 | 47 | — | — |
| **Total** | **245** | **317** | **100** | **225** |

For the resistive magnets, the capital costs differ between the Radiation-hard

Transport Solenoid (RTS) and normal RTS. The RTS uses Pyrotenax and costs 225,000 CHF per magnet, while the Normal Transport Solenoid (NTS) uses copper and costs 100,000 CHF per magnet. Consequently, the capital costs of the NbTi superconducting transport solenoid are nearly 2.5 times larger than its resistive counterpart but comparable to the RTS. For the YBCO version, the capital cost is 3.2 times larger than the resistive version, 33% higher than the NbTi transport solenoid, and 40% higher than the RTS.

Considering the capital costs, the NbTi transport solenoid is preferred due to its lower price; however, the YBCO version remains a viable solution if the radiation thermal load is too high for the NbTi version. Despite the higher costs compared to NTS, superconducting solenoids are expected to offset their costs through energy savings eventually. The subsequent analysis evaluates when this occurs and quantifies the savings.

### 5.1.1 | Personnel costs for PSI

In addition to material costs, personnel expenses must be considered when winding the magnet at PSI. PSI provided estimates for the required personnel months to complete the magnet fabrication. For the C-type solenoid, an estimated 12 personnel months are needed. The AB-type solenoid, being more complex due to its location inside the vacuum chamber, requires approximately 16 personnel months. The breakdown of these personnel months is illustrated in Figure 5.1.

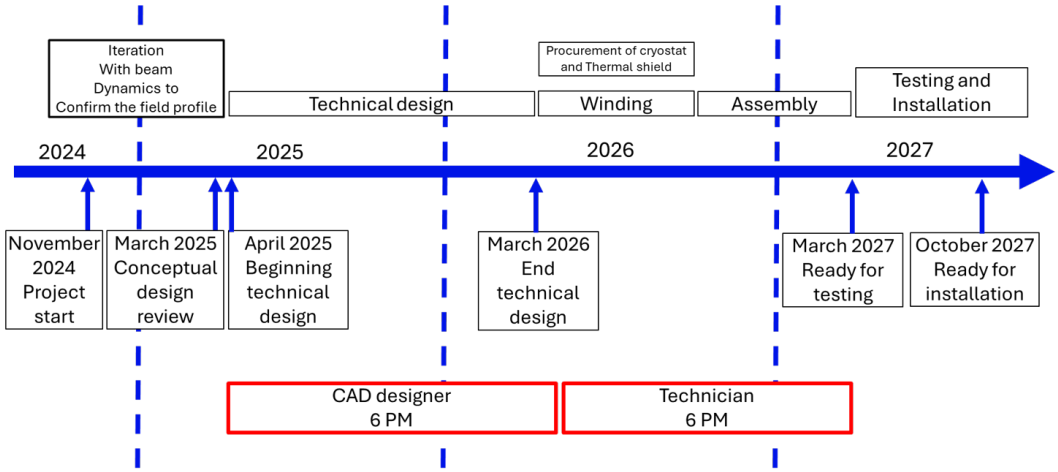


Figure 5.1: Breakdown of personnel months required for winding the C-type and AB-type solenoids.

For the AB-type solenoids, the additional four personnel months are allocated as follows: modeling of vacuum lines and vacuum flanges for the large vacuum chamber (1 month for the CAD designer), modeling of test equipment (1 month for the CAD designer), assembly of the large vacuum flange and vacuum lines (1 month for the technician), and assembly of test equipment (1 month for the technician).

Assuming an annual personnel cost of 120 kCHF per full-time equivalent (FTE), and accounting for entitled vacation time (approximately 2 months per year), the effective cost per personnel month is 10 kCHF. Therefore, the personnel costs are calculated as:

- **C-type solenoid**: 12 personnel months × 10 kCHF/month = 120 kCHF.
- **AB-type solenoid**: 16 personnel months × 10 kCHF/month = 160 kCHF.

These personnel costs are consistent regardless of the superconducting material used (NbTi or YBCO), as the winding process and labor requirements are similar for both materials.

Notably, if multiple solenoids are produced, the design and setup costs can be spread over several units, effectively reducing the average price per solenoid. Even the implementation of a single superconducting solenoid constitutes a significant advancement in science and engineering by introducing low-power, large-aperture superconducting transport solenoids into radioactive beamlines. For a single solenoid, the worst-case scenario, the total capital costs, including personnel, are summarized in Table 5.3.

Table 5.3: Capital costs of different systems, with and without personnel costs.

| **Component** | **NbTi** [kCHF] | **YBCO** [kCHF] | **NTS** [kCHF] | **RTS** [kCHF] |
|---|---|---|---|---|
| System | 240 | 270 | 100 | 225 |
| Material | 5.8 | 47 | — | — |
| Personnel (C) | 120 | 120 | — | — |
| Personnel (AB) | 160 | 160 | — | — |
| **Total for C** | **366** | **437** | **100** | **225** |
| **Total for AB** | **406** | **467** | **100** | **225** |

## 5.2 | Life Cycle Assessment

As discussed in the literature review, $CO_2$ emissions are used as the environmental proxy due to their direct impact on global warming.

Only the $CO_2$ contribution from the wire or tape is considered, as it is the most emission-intensive part of the magnet system. Other potential $CO_2$ emission sources not considered include:

1. Cryostat
2. Vacuum system
3. Cryocooler

4. Power supply
5. Insulation material
6. Structural support
7. Thermal shield
8. Steel yoke

This simplification is justified because the excluded components contribute minimally to the total emissions. For instance, the insulation material consists of a small amount of MLI [15], the structural support comprises four small G10 rods, and the thermal shield is a thin layer of aluminum or copper. The steel yoke lids are straightforward to produce and thus have a minor emission footprint.

The $CO_2$ emissions for producing the resistive magnet, NbTi magnet, and YBCO magnet are shown in Table 5.4. The $CO_2$ emissions per tonne of the product are extracted from the literature [55, 56]. It is important to note that the available literature on the LCA of superconducting materials remains limited, highlighting the need for further research in this area. Nevertheless, the analyses by [55] for YBCO and [56] for NbTi wire provide the most comprehensive data currently available, incorporating complete cradle-to-grave assessments into their studies.

Table 5.4: $CO_2$ emissions for producing different materials used in transport solenoids.

| **Material** | **$CO_2$ [kg/kg]** | **Mass [t]** | **$CO_2$ per Solenoid [t]** |
|---|---|---|---|
| Copper | 7.0 | 1.3 | 9.1 |
| NbTi | 17.0 | 0.03 | 0.51 |
| YBCO | 490.0 | 0.005 | 2.5 |

From Table 5.4, it is evident that YBCO wire has significantly higher $CO_2$ emissions per kilogram compared to NbTi and copper, being 29 times more polluting than NbTi and 70 times more than copper. However, due to the much lower required mass of YBCO wire, the total $CO_2$ emissions per solenoid are lower than those of the copper wire used in resistive magnets. The NbTi wire results in the lowest total $CO_2$ emissions among the three materials, making the NbTi magnet version the most favorable replacement from an environmental perspective.

## 5.3 | Energy Savings

The power consumption breakdown for the superconducting magnets is calculated as follows:

1. **Cryocooler Power Consumption**: 3.6 kW for the NbTi version and 4.8 kW for the YBCO version, accounting for maximum radiation power extraction. In principle, operation of the YBCO with a lower powered cryocooler is possible, but to operate at a high radiation position, a 4.8 kW cryocooler is required.

2. **Vacuum Pump**: 0.5 kW.

3. **Power Supply**: Assuming a maximum power supply voltage of 10 V originating due to the resistive current leads, the maximum power is $P = VI$, where $I$ is the current (96 A for NbTi and 269 A for YBCO).

   Based on the beamline life-cycle:

   - For the MuH2 beamline, the magnet operates at full power 5% of the time and at half power 95% of the time. The average power consumption is:

   $$P_{\text{avg}} = 0.05 \times VI + 0.95 \times \frac{VI}{2} = 0.525\, VI.$$

   - For the MuH3 beamline, the magnet runs at half power 100% of the time, leading to $P_{\text{avg}} = 0.5\, VI$.

   For simplicity, $P_{\text{avg}} = 0.525\, VI$ is used for both beamlines.

4. **Calculated Power Supply Consumption**:

   - NbTi: $0.525 \times 10\ \text{V} \times 96\ \text{A} = 504\ \text{W}$.
   - YBCO: $0.525 \times 10\ \text{V} \times 269\ \text{A} = 1,411\ \text{W}$.

Table 5.5 presents the key energy consumption results. The capital costs for all the magnets are presented in the second column. The annual energy $E$ is calculated by multiplying the power $P$ by the operational hours (4,000 h). The annual energy is visualized in Figure 5.2. These energy savings will inform the subsequent economic and environmental analyses.

Table 5.5: Energy consumption and savings for different options.

| Option | Capital [kCHF] | $P$ [kW] | $E$ [MWh] |
|---|---|---|---|
| NbTi | 246 | 4.6 | 18.4 |
| YBCO | 317 | 6.7 | 26.8 |
| MuH2 AB | 225 | 40.1 | 160.4 |
| MuH2 C | 100 | 18.9 | 75.6 |
| MuH3 AB | 225 | 38.0 | 152.0 |
| MuH3 C | 100 | 16.4 | 65.6 |

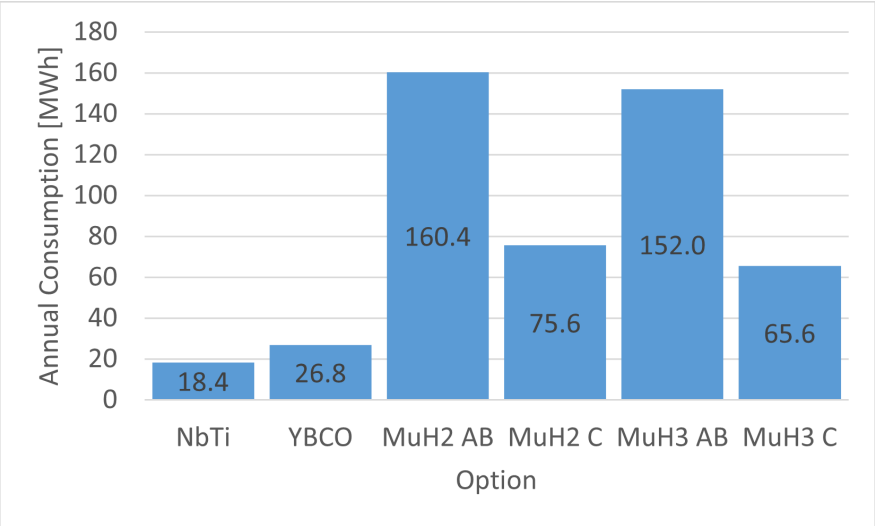


Figure 5.2: Annual energy consumption for different magnet options.

## 5.4 | Economic Implications

As shown in Table 5.2, the capital costs of the superconducting magnet are higher than those of the normal transport solenoid but approximately equal to the costs of the radiation-hard transport solenoid. This raises the question of whether the superconducting magnet is economically viable.

To evaluate the economic viability, three key metrics are considered:

1. **Break-even time**: The time it takes for the superconducting magnet to offset its higher initial capital cost through energy savings.
2. **Break-even capital cost**: The capital cost at which the superconducting magnet would break even after 15 years of operation.
3. **Total running costs after 15 years**: The sum of capital and operational costs over 15 years.

The total cost of a magnet is given by:

$$C = C_{\text{capital}} + C_{\text{running}}, \tag{5.1}$$

where $C_{\text{capital}}$ is the capital cost, and $C_{\text{running}}$ is the running cost calculated as:

$$C_{\text{running}} = E \times t \times p, \tag{5.2}$$

with $E$ being the annual energy consumption, $t$ the operational time in years, and $p$ the price of electricity.

Using these equations, the break-even time $T$ is calculated by:

$$T = \frac{C_{\text{SC}} - C_{\text{RC}}}{p \times (E_{\text{RC}} - E_{\text{SC}})}, \tag{5.3}$$

where:

- $C_{SC}$ and $C_{RC}$ are the capital costs of the superconducting and resistive magnets, respectively.
- $E_{SC}$ and $E_{RC}$ are their annual energy consumptions.

The break-even time is minimized when:

- The capital cost difference between superconducting and resistive magnets is small.
- The superconducting magnet consumes significantly less energy annually.
- The electricity price is high.

The total costs after 15 years are:

$$C_{\text{total}} = C_{\text{capital}} + E_{\text{total}} \times p, \tag{5.4}$$

where $E_{\text{total}}$ is the total energy consumption over 15 years, as given in Table 5.5.

For the superconducting system to break-even after 15 years, the break-even capital cost is calculated as:

$$C_{\text{break-even}} = C_{RC} + E_{\text{total}} \times p. \tag{5.5}$$

Using an electricity price of 0.2 CHF per kWh (as projected by PSI's infrastructure department head Markus Jörg), the results are presented in Table 5.6. The table includes the total capital costs, total running costs, and break-even times for the NbTi and the YBCO version of the superconducting solenoid.

Table 5.6: Economic analysis for different options. The MuH2 AB, MuH2 C, MuH3 AB, and MuH3 C correspond to resistive solenoids at positions A, B, and C, respectively, for beamlines MuH2 and MuH3. Variables include capital costs, total costs, and break-even times

| Option | Capital [kCHF] | $C_{\text{running}}$ [kCHF] | $T_{\text{NbTi}}$ [years] | $T_{\text{YBCO}}$ [years] |
|---|---|---|---|---|
| NbTi | 246 | 55 | — | — |
| YBCO | 317 | 80 | — | — |
| MuH2 AB | 225 | 481 | 0.7 | 3.4 |
| MuH2 C | 100 | 227 | 12.7 | 22.2 |
| MuH3 AB | 225 | 456 | 0.8 | 3.7 |
| MuH3 C | 100 | 197 | 15.4 | 28.0 |

Figure 5.3 compares the economic performance of NbTi and YBCO superconducting magnets with resistive transport solenoids.

**Key insights from the economic analysis:**

- The break-even time for a NbTi normal transport solenoid is 13 and 15 years for the MuH2 and MuH3 beamlines, respectively, which aligns with the conservative

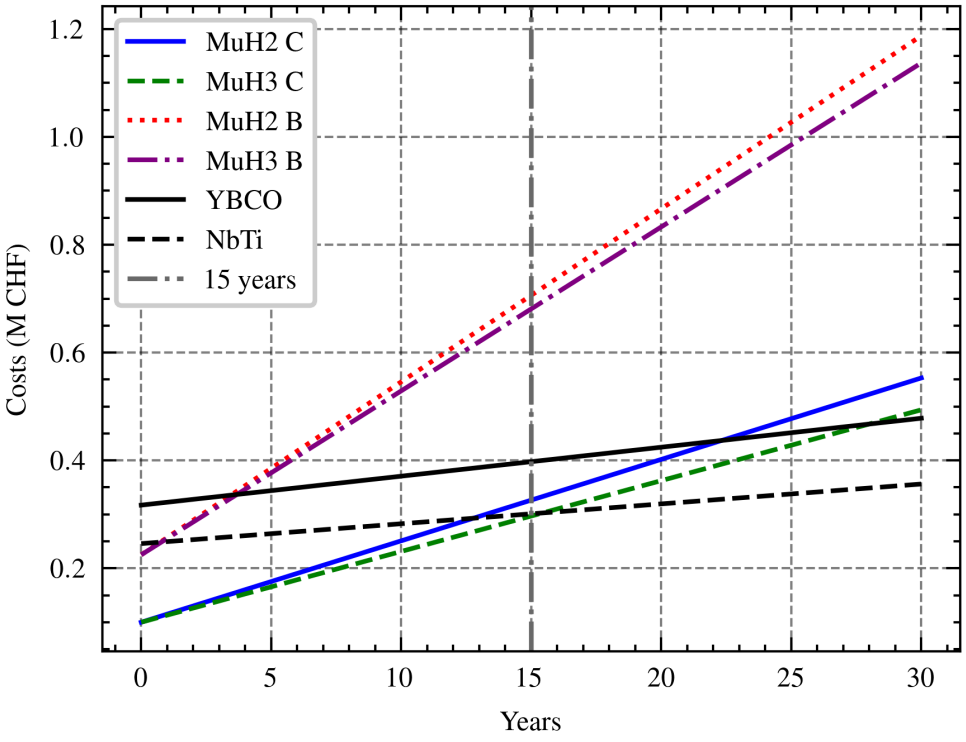


Figure 5.3: NbTi vs. YBCO Transport Solenoids.

operational estimate. The investment is justified since previous beamlines operated for 25–30 years.

- For YBCO, the break-even time is 22 and 28 years for the MuH2 and MuH3 beamlines, making it less economically viable for normal solenoids. However, significant benefits are observed for radiation-hard solenoids, with a break-even time of less than 4 years.

- The break-even time for the radiation-hard transport solenoids is less than a year for the NbTi version. Due to high radiation levels at position A, the NbTi version is suitable for position B, while the YBCO version may be adapted for position A.

- Overall, the NbTi version is economically advantageous compared to the YBCO version, owing to lower capital and running costs.

The break-even time of 22 and 28 years for YBCO is concerning as the longevity issues might arise. Past experience shows that the superconducting magnets are capable of surviving more than 50 years such as the SULTAN facility at PSI [68]. In the next section, an environmental analysis is conducted to assess the benefits of the NbTi and YBCO versions compared to the resistive magnet.

## 5.5 | Environmental Analysis

To quantify $CO_2$ savings, a conversion factor of 100 g $CO_2$ equivalent per kWh is used [54]. Using the annual energy consumption values from Table 5.5, the annual $CO_2$ emissions are calculated as:

$$CO_{2\text{annual}} = E \times k, \tag{5.6}$$

where $E$ is the annual energy consumption and $k$ is the conversion factor (0.1 kg/kWh). The $CO_2$ savings for NbTi and YBCO superconducting magnets are determined by subtracting their emissions from those of the resistive magnets. The total $CO_2$ savings after 15 years are obtained by multiplying the annual savings by 15.

Equation 5.6 indicates that $CO_2$ savings are maximized when the difference in energy consumption between superconducting and resistive magnets is significant and when the $CO_2$ conversion factor is high. According to [54], Switzerland has relatively low $CO_2$ emissions per kWh compared to neighboring countries—Poland's conversion factor is eight times higher, and Germany's is three times higher. This disparity is due to Switzerland's significant use of nuclear power, whereas Poland relies heavily on coal, a highly polluting energy source.

The results are summarized in Table 5.7, where the LCA data from Table 5.4 is combined with the operational $CO_2$ emissions to obtain the total $CO_2$ emissions per transport solenoid after 15 years of operation. Although data for the radiation-hard transport solenoids are lacking due to uncertainty in pyrotenax data, their $CO_2$ emissions are assumed to be similar to those of the normal transport solenoids.

Table 5.7: $CO_2$ emissions for different options. The MuH2 AB, MuH2 C, MuH3 AB, and MuH3 C correspond to the resistive solenoids at positions A, B, and C for beamlines MuH2 and MuH3.

| **Option** | LCA [t] | $CO_2^{\text{annual}}$ [t] | Total $CO_2$ [t] |
|---|---|---|---|
| NbTi | 0.5 | 1.8 | 28 |
| YBCO | 2.5 | 2.7 | 43 |
| MuH2 AB | 9.1 | 16.0 | 250 |
| MuH2 C | 9.1 | 7.6 | 123 |
| MuH3 AB | 9.1 | 15.2 | 237 |
| MuH3 C | 9.1 | 6.6 | 108 |

**Key insights from the environmental analysis:**

- **MuH2 AB Beamline**: The NbTi version saves 16 tonnes of $CO_2$ annually and 241 tonnes after 15 years. The YBCO version saves 13 tonnes annually and 200 ,tonnes after 15 years.
- **MuH2 C Beamline**: The NbTi version saves 71 tonnes of $CO_2$ after 15 years, while the YBCO version saves 58 tonnes.

- **Normal Transport Solenoids**: The NbTi version saves 1.8 tonnes of $CO_2$ annually and 28 tonnes after 15 years. The YBCO version saves 2.7 tonnes annually and 40 tonnes after 15 years.

For perspective, an average Swiss resident emits about 13 tonnes of $CO_2$ annually [69].

The evolution of $CO_2$ emissions for different options is illustrated in Figure 5.4. From an environmental standpoint, the superconducting versions are more advantageous than the resistive versions. The NbTi version is particularly favorable due to the lower $CO_2$ emissions of NbTi wire production and lower power consumption.

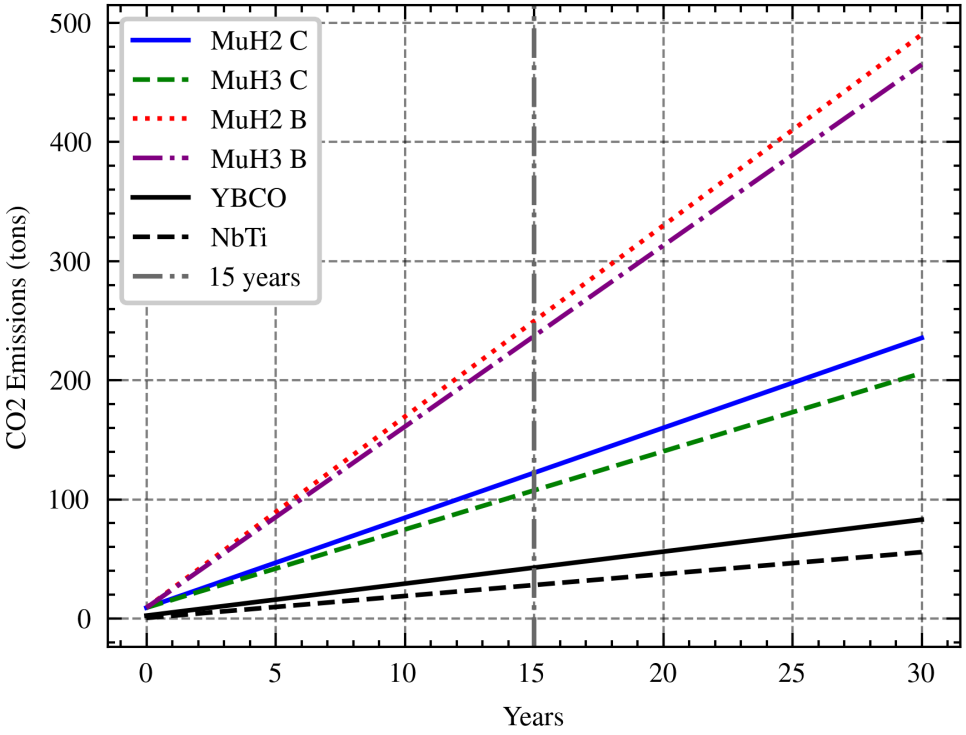


Figure 5.4: $CO_2$ Comparison of NbTi vs. YBCO Transport Solenoids.

## 5.6 | Directorate Decision

The findings of this study were presented to the PSI directorate in October 2024. Based on the comprehensive analysis and results, the PSI directorate decided to implement a single NbTi solenoid at Position C of the MuH2 beamline. This significant milestone sets a benchmark for the adoption of superconducting materials within PSI's accelerator-driven research infrastructures—**a decision made possible by the outcomes of my work.** Several key considerations influenced this strategic decision:

1. **Gradual Implementation Strategy**: PSI aims to introduce superconducting magnet technology in a controlled manner. By starting with Position C, the most accessible location, PSI can manage the integration process effectively. An additional resistive magnet will also be used as a backup to ensure operational reliability during the initial phase.

2. **Operational Challenges at Positions A and B**: Positions A and B present unique challenges due to the magnets being housed within large vacuum chambers. The complexity of these installations requires additional resources and expertise, making them less suitable for the initial implementation phase with the deadline of 2027.

3. **Resource Allocation**: The current human resources are insufficient to construct all six planned solenoids simultaneously within the C beamline. Therefore, implementing a single solenoid allows PSI to allocate resources efficiently and scale the project as needed.

4. **Focus on Energy Efficiency and Sustainability**: Future upgrades prioritize energy conservation and environmental sustainability. Configurations that significantly increase energy consumption, as highlighted in Table 1.1, are not favored. Superconducting magnets demonstrated to offer substantial energy savings and reduced $CO_2$ emissions align with PSI's sustainability goals and provide a pathway for more energy-efficient operations.

5. **Radiation Damage Data for Position A**: There is insufficient radiation damage data for superconducting magnets at Position A. To address this, PSI plans to commission an HTS demonstrator at the HIMB facility within a high-radiation environment near the target. This demonstrator will facilitate the empirical assessment of radiation-induced degradation in HTS solenoids, laying the groundwork for future deployment of YBCO superconducting magnets in high-thermal-load positions such as Position A.

By adopting this strategic approach, PSI ensures a successful and sustainable integration of superconducting technology into its beamline operations. The initial implementation at Position C will provide valuable insights and data, informing future deployments and optimizations of HTS solenoids in more challenging environments. This phased and resource-conscious strategy enhances operational efficiency and aligns with PSI's long-term energy conservation and environmental responsibility objectives.

# 6

# Conclusion

## 6.1 | Dissertation Aims and Conclusion

This dissertation investigates integrating superconducting magnet technology to enhance energy efficiency at the HIMB facility at the PSI. The primary aim is to evaluate superconducting magnets' technical, environmental, and economic viability as replacements for resistive magnets within the HIMB context. The research is structured around four key objectives, each providing comprehensive insights and practical advancements for successfully implementing superconducting technology within PSI's
accelerator-driven research infrastructures.

The first objective involved an extensive literature review of radiation damage mechanisms affecting superconducting materials. This review was carried out in collaboration with the PSI beam dynamics team, which provided valuable data on the thermal energy of radiation at the HIMB facility. However, the available data did not include measurements of the neutron flux in the beamline, which are critical for accurately quantifying overall radiation degradation. In addition, discussions with cryostat manufacturers (Cryomech and Sumitomo) revealed that the extent of radiation-induced damage to cryostat components remains largely unknown. These gaps in our current understanding of radiation effects underscore the need for further empirical investigations.

The second objective was to develop a robust superconducting solenoid model using COMSOL Multiphysics, incorporating the radiation-induced thermal loads characteristic of the HIMB environment. This finite element analysis model enabled realistic simulations of operational conditions and included a parametric study to identify the heat load from the radiation levels at which the solenoids operate effectively. The study revealed that the extreme radiation heat load at position A necessitates using YBCO superconductors, leading to the successful modeling of a HTS solenoid. This advanced modeling approach predicts superconducting solenoids' performance and safety parameters and is a critical tool for future design optimizations.

The third objective focused on evaluating layer winding techniques for YBCO tapes. Pancake winding often introduces numerous joints that introduce additional

thermal load into the system. This research successfully demonstrated the feasibility of layer winding through the fabrication and testing of a layer-wound YBCO magnet prototype. The results indicated no degradation in critical current in the bent sections of the magnet, validating layer winding as a viable method for producing large-diameter coils. This innovation enhances the reliability and performance of superconducting solenoids, positioning them well for future application in the HIMB demonstrator, where it will undergo testing for radiation-induced damage.

The fourth objective involved a comprehensive economic and environmental evaluation of superconducting solenoids compared to resistive magnets. This analysis revealed significant energy savings associated with the reduced power consumption of superconducting technology, leading to substantial reductions in $CO_2$ emissions. The findings demonstrate the economic viability of adopting superconducting solenoids, with lower operational costs supporting their implementation. **These compelling benefits influenced the PSI directorate to endorse the proposed superconducting solenoid design for the MuH2 C position, marking a significant milestone in the transition towards superconducting technology at PSI.**

This strategic decision sets a precedent for integrating superconducting materials within PSI's accelerator-driven research infrastructures. By replacing a traditional resistive solenoid with a superconducting version, PSI enhances the performance of the HIMB facility, achieves significant energy savings, and reduces its environmental footprint, aligning with its environmental mission statement.

In conclusion, this dissertation substantially contributes to superconducting magnet technology by demonstrating its practical viability and strategic benefits at PSI. By addressing critical challenges related to radiation effects, winding techniques, and comprehensive economic and environmental evaluations, this research establishes a robust framework to design superconducting solenoids for high-intensity, high-radiation particle accelerator environments. The successful integration of superconducting solenoids enhances PSI's capabilities and aligns with global sustainability goals, positioning superconducting technology as a cornerstone of future accelerator technologies.

## 6.2 | Proposals for Future Work

Building upon the findings of this study and addressing the identified research gaps, the following future work is proposed to further advance the integration and optimization of superconducting solenoids at the HIMB.

- **Experimental Validation of Radiation Effects on Superconducting System Components**: Undertake empirical investigations using the HTS demonstrator in the HIMB beamline to quantify radiation-induced degradation in HTS magnets

systematically. The resulting data will inform optimizing design parameters for enhanced radiation resilience.

In addition, a detailed assessment of radiation damage to cryocoolers should be conducted to ensure the overall reliability of the superconducting system under high-radiation conditions.

- **Integration of PHP Cooling Systems in HTS Solenoids**: Explore the use of PHP cooling systems in collaboration with the PHP research group at PSI. PHP can serve as an efficient thermal pathway to cool the magnet, especially if the cryocooler is farther away from the magnet. This integration can be applied to the HTS radiation damage demonstrator if the deposited dose damages the cryocooler. Implementing PHP cooling systems will enhance the thermal management of superconducting solenoids, ensuring their stable operation in high-radiation environments by maintaining safe distances.

- **Comprehensive Life cycle Analysis of Superconducting vs. Resistive Solenoids**: Conduct a detailed LCA—a full cradle-to-grave assessment—that encompasses the production, operation, and end-of-life phases of superconducting solenoids and their constituent materials compared to resistive alternatives. This holistic evaluation will provide critical insights into superconducting technology's environmental and economic impacts, reinforcing the sustainability case for superconducting systems. Ultimately, a comprehensive LCA will inform strategic decisions and underscore the long-term benefits of adopting superconducting technology.

- **Establishing Radiation-Validated Degradation Models and Scaling Strategies**: Develop predictive degradation models for HTS materials based on experimentally validated radiation damage data. Given the challenges of reproducing the full mixed-particle spectrum, integrated fluence, and cryogenic irradiation conditions, future work should focus on approximating these factors through controlled short-term tests and validated extrapolation techniques. This includes mapping the particle spectrum and fluence at critical locations (e.g., Position A) along the HIMB beamline and evaluating the mechanical and superconducting performance of irradiated HTS tapes.

  If the demonstrator exhibits stable critical current and temperature under irradiation, this would support scale-up efforts. However, if degradation is observed, further investigation is needed to understand failure mechanisms and identify potential showstoppers. Scaling to a full-size HTS magnet will also require addressing technical challenges related to mechanical winding, cryogenic integration, and local radiation field variation. A reliable and predictive model

is essential to ensure long-term operational integrity under realistic HIMB conditions.

Addressing these areas will further advance the development and deployment of superconducting solenoids at PSI and beyond, ensuring their performance, reliability, and sustainability in high-radiation and high-intensity beamline environments. These future initiatives will enhance the current HIMB upgrade and set the stage for broader adoption of superconducting technologies within PSI's accelerator-driven research infrastructures.

# A

# Scaling Laws

This appendix presents the scaling law used to estimate the engineering critical current density $J_e$ of NbTi and YBCO as a function of magnetic flux density $B$ and temperature $T$. These relationships, known as scaling laws, are essential for modeling the performance of superconducting magnets and are expressed in the form $J_e(B, T)$.

## A.1 NbTi Scaling Law

To determine the engineering critical current density $J_e(B, T)$ for NbTi, we employ the scaling law proposed by Bottura [8]. The scaling law is given by:

$$J_e(B,T) = J_{ref} \cdot C_0 \cdot b^{\alpha} \cdot (1-b)^{\beta} \cdot (1-t^m)^{\gamma}, \tag{A.1}$$

where:

$$t = \frac{T}{T_{c0}}, \quad b = \frac{B}{B_{c2}}, \tag{A.2}$$

and the upper critical field $B_{c2}$ is defined as:

$$B_{c2} = B_{c20}\,(1-t^m)\,. \tag{A.3}$$

In these equations:

- $J_e$ is the engineering critical current density.
- $C_0$, $\alpha$, $\beta$, $\gamma$, and $m$ are empirical coefficients.
- $T_{c0}$ is the critical temperature at zero magnetic field.
- $B_{c20}$ is the upper critical magnetic field at absolute zero temperature.

Bottura suggests a value of $m = 1.7$ for the exponent in the temperature dependence of $B_{c2}$.

The coefficients used in this scaling law are tailored to match the characteristics of the NbTi wire from Bruker, which is also utilized in the SLS2 superbend magnets. The specific values of these coefficients are provided in Table A.1.

Table A.1: Coefficients used in the NbTi scaling law (Equation A.1).

| Symbol | Value | Unit | Description |
|---|---|---|---|
| $C_0$ | 26,274 | – | Scaling constant |
| $\alpha$ | 0.812 | – | Exponent for $b$ |
| $\beta$ | 1.23 | – | Exponent for $1 - b$ |
| $\gamma$ | 2.32 | – | Exponent for $1 - t^m$ |
| $m$ | 1.7 | – | Exponent in $B_{c2}$ temperature dependence |
| $B_{c20}$ | 14.5 | T | Upper critical field at 0 K |
| $T_{c0}$ | 9.2 | K | Critical temperature at 0 T |
| $J_{ref}$ | 3.78 | kA/mm$^2$ | Reference engineering critical current density |

# A.2 YBCO Scaling Law

The scaling law for YBCO was derived from the data presented in [66]. We focused on the perpendicular magnetic field orientation, as it represents the lowest performance scenario and thus serves as a worst-case condition. Utilizing Python's `scipy.interpolate.interp2d` function, we interpolated the provided plot to develop an analytical model of the critical current density $J_e(B,T)$. The resulting scaling law is illustrated in Figure A.1.

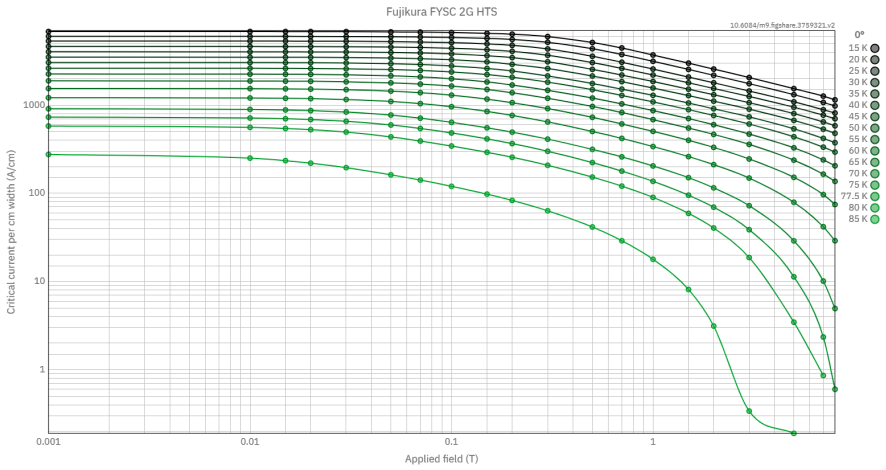


Figure A.1: Scaling law for YBCO under perpendicular magnetic field orientation. Adapted from [66].

# B

# Material properties

This appendix details the material properties utilized in the simulation model for the HIMB project. The data, extracted from the SLS2 upgrade [4] and from the works of [57, 58, 70], includes thermal conductivity $k(T)$ and specific heat capacity at constant pressure $c_p(T)$ for copper, NbTi, epoxy, G10, and YBCO tape.

## B.1 | Copper Material properties

The thermal conductivity is given in Figure B.1 and the specific heat capacity at constant pressure is given in Figure B.2.

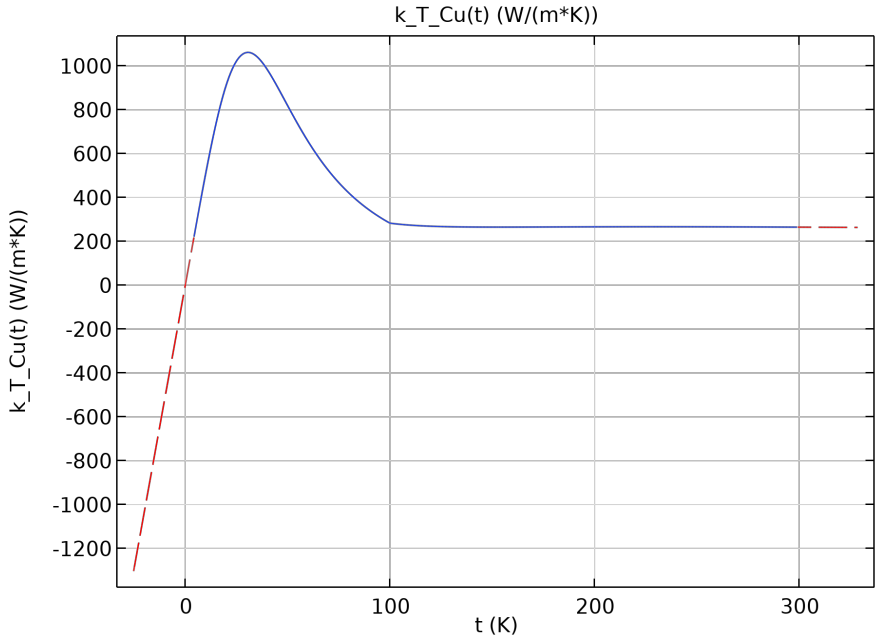


Figure B.1: Thermal conductivity of copper as a function of temperature.

## B.2 | Epoxy Material properties

The thermal conductivity is given in Figure B.3 and the specific heat capacity at constant pressure is given in Figure B.4.

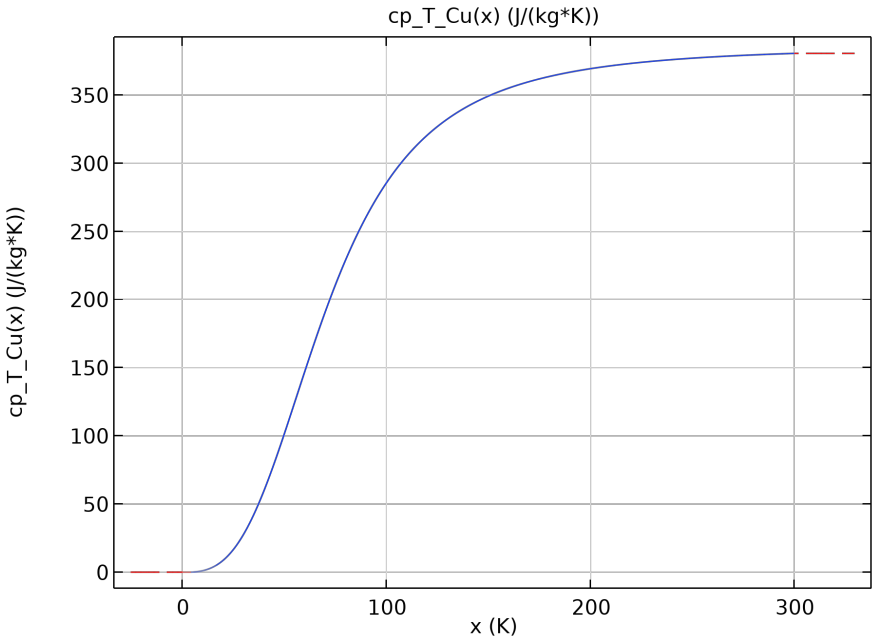


Figure B.2: Specific heat capacity of copper at constant pressure as a function of temperature.

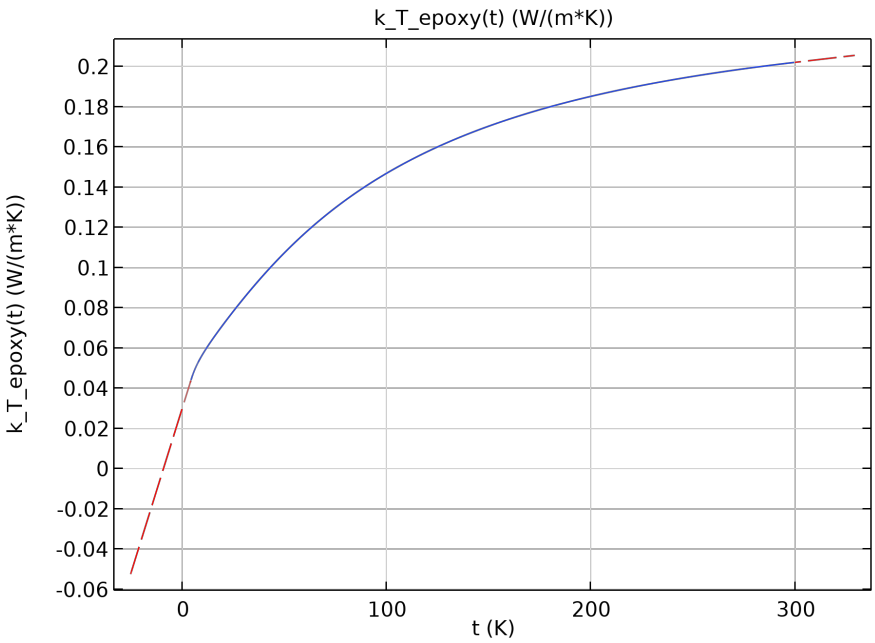


Figure B.3: Thermal conductivity of copper as a function of temperature.

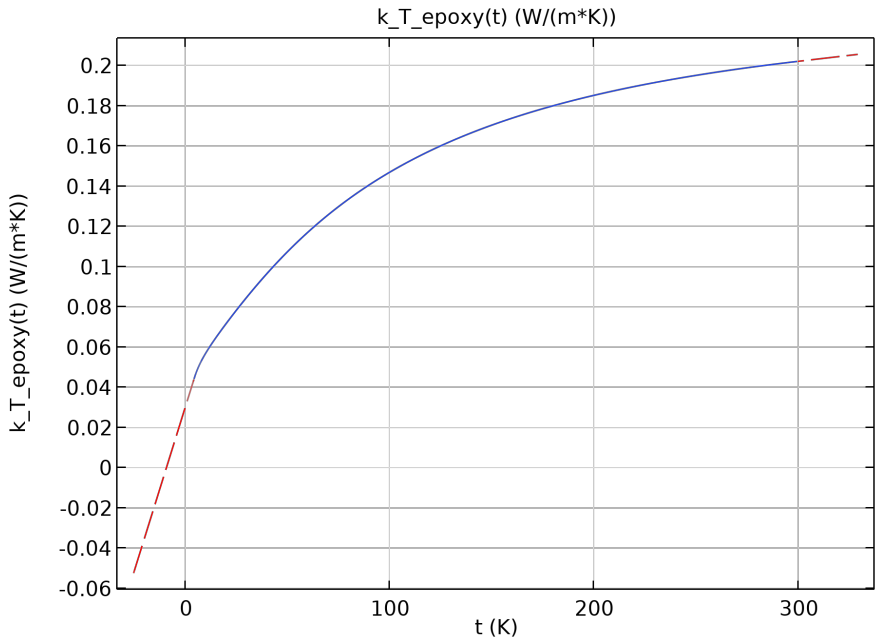


Figure B.4: Specific heat capacity of epoxy at constant pressure as a function of temperature.

## B.3 | G10 Material properties

The thermal conductivity is given in Figure B.5 and the specific heat capacity at constant pressure is given in Figure B.6.

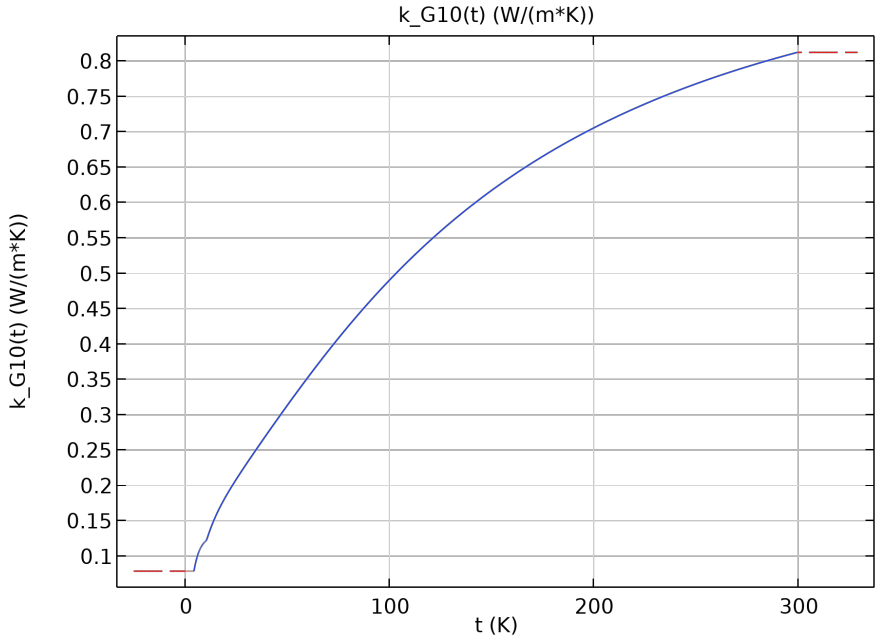


Figure B.5: Thermal conductivity of G10 as a function of temperature.

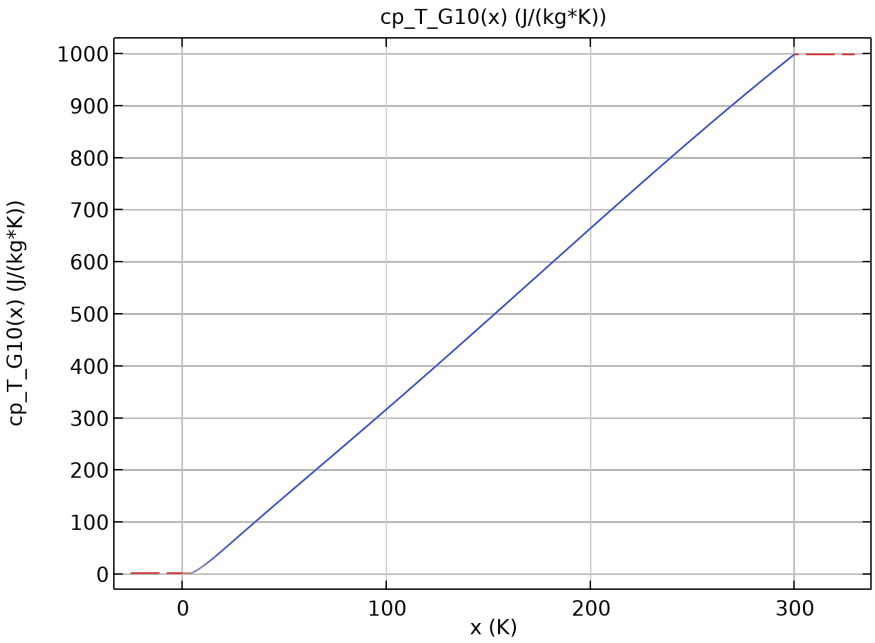


Figure B.6: Specific heat capacity of G10 at constant pressure as a function of temperature.

## B.4 | NbTi Material properties

The thermal conductivity for the transverse and longitudinal directions was taken as the thermal conductivity of a fraction of epoxy for the transverse and as a function of the thermal conductivity of copper for the longitudinal direction. This is justified due to the dominance of those terms when considering the law of compositions. The specific heat capacity at constant pressure is given in Figure B.7.

## B.5 | YBCO Material properties

The thermal conductivities along the transverse direction is given in Figure B.8 [57] and longitudinally in Figure B.9, taken from [58]. The specific heat capacity at constant pressure is given in Figure B.10 and extracted from [70].

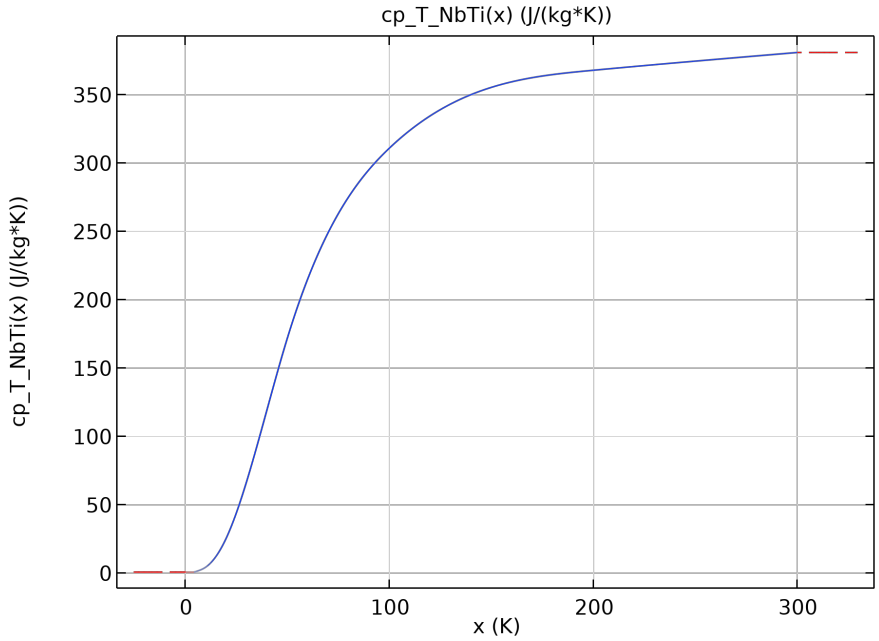


Figure B.7: Specific heat capacity of NbTi at constant pressure as a function of temperature.

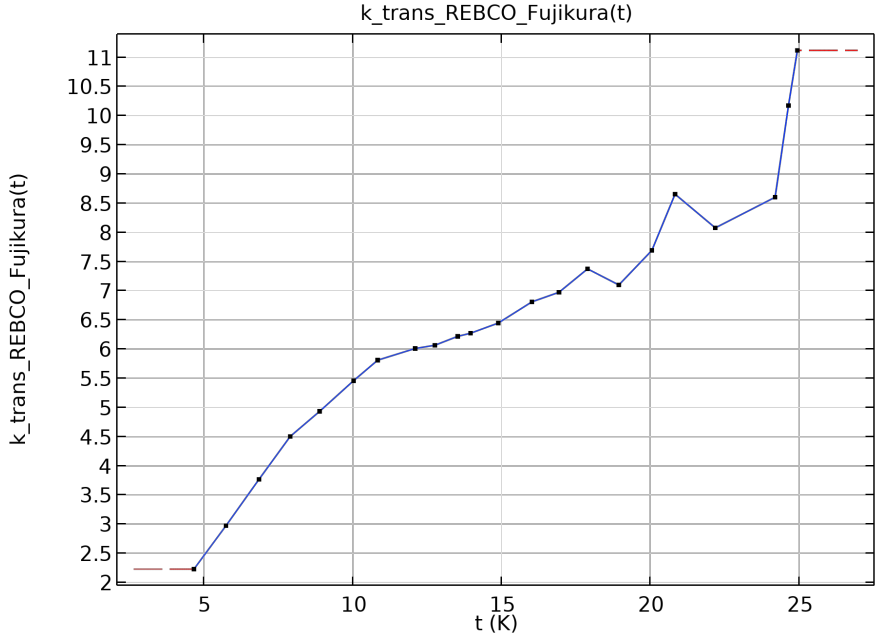


Figure B.8: Transverse thermal conductivity of YBCO as a function of temperature. Taken from [57].

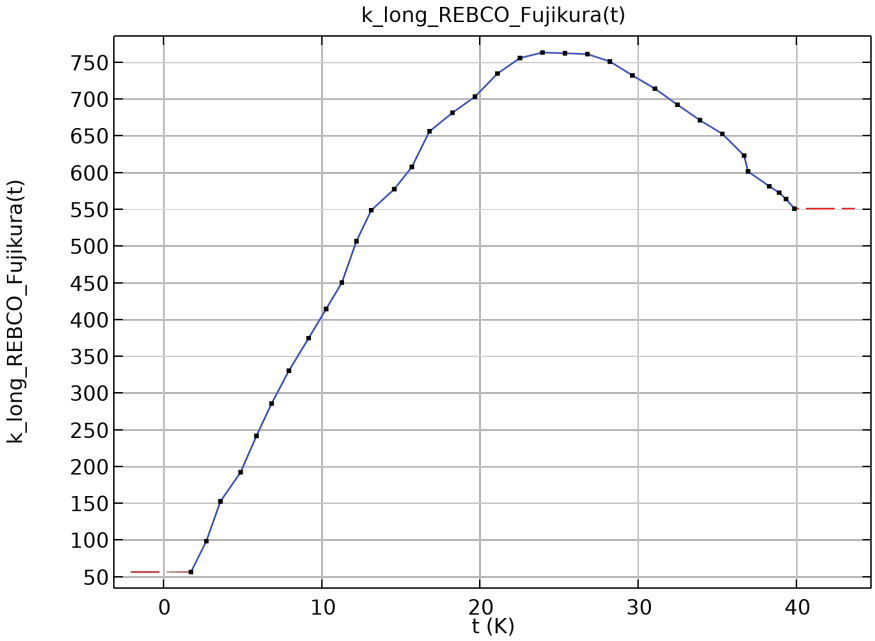


Figure B.9: Longitudinal thermal conductivity of YBCO as a function of temperature. Taken from [58].

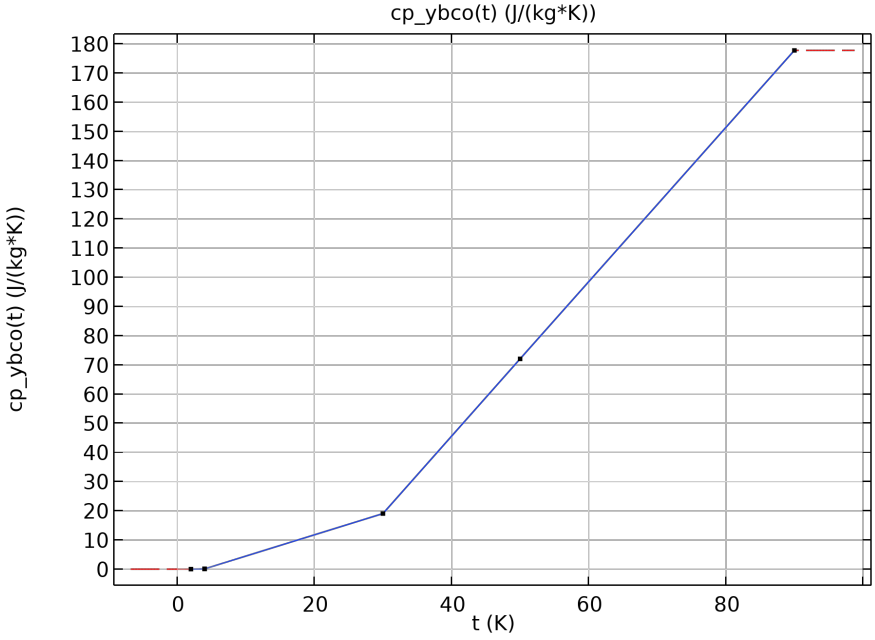


Figure B.10: Specific heat capacity of YBCO at constant pressure as a function of temperature. Taken from [70].

# References


[1] G. Dal Maso, A. Gabard, M. Haj Tahar, P.-R. Kettle, K. Kirch, D. Kiselev, A. Koschik, A. Knecht, D. Laube, A. Papa, T. Rauber, D. Reggiani, R. Riccioli, J. Snuverink, V. Talanov, and E. Valetov, "Future facilities at PSI, the High-Intensity Muon Beams (HIMB) project," *EPJ Web of Conferences*, vol. 282, p. 01012, 2023.

[2] A. L. Gabard, J. P. Duppich, and D. George, "Radiation Hard Magnets at the Paul Scherrer Institute," in *Proceedings of the International Particle Accelerator Conference (IPAC)*, 2012. [Online]. Available: https://accelconf.web.cern.ch/ipac2012/papers/thppd011.pdf

[3] R. Riccioli, C. Calzolaio, A. Gabard, P.-R. Kettle, D. Kiselev, A. Knecht, Rp. Martinie, G. Dal Maso, A. Papa, T. Rauber, D. Reggiani, S. Sanfilippo, J. Snuverink, and E. Valetov, "Magnet Design for the High-Intensity Muon Beams Project (HIMB) at PSI's Accelerator Complex HIPA," *IEEE Transactions on Applied Superconductivity*, vol. 34, no. 5, pp. 1–5, Aug. 2024.

[4] C. Calzolaio, G. Montenero, and S. Sanfilippo, "Superconducting Longitudinal Gradient Bend for the Swiss Light Source Upgrade: Thermo-Mechanical Study," *IEEE Transactions on Applied Superconductivity*, vol. 29, no. 5, pp. 1–4, Aug. 2019.

[5] N. Vallis, B. Auchmann, P. Craievich, M. Duda, H. Garcia Rodrigues, J. Kosse, M. Schaer, and R. Zennaro, "P-cubed: A positron source demonstrator for fcc-ee," *Proc. of the 65th ICFA Advanced Beam Dynamics Workshop on High Luminosity Circular e+e- Colliders*, vol. eeFACT2022, pp. 1–4, 2022.

[6] M. Wilson, *Superconducting Magnets*, ser. Monographs on cryogenics. Clarendon Press, 1983. [Online]. Available: https://books.google.ch/books?id=AObvAAAAMAAJ

[7] Y. Iwasa and K. R. Marken, "*Case Studies in Superconducting Magnets: Design and Operational Issues*," *Physics Today*, vol. 48, no. 10, pp. 68–68, Oct. 1995.

[8] L. Bottura, "A practical fit for the critical surface of NbTi," *IEEE Transactions on Appiled Superconductivity*, vol. 10, no. 1, pp. 1054–1057, Mar. 2000.

[9] "Robinson HTS Wire Critical Current Database," https://htsdb.wimbush.eu/.

[10] V. Parma, "Cryostat Design," *CAS - CERN Accelerator School: Superconductivity for Accelerators*, pp. 353–399, 2014. [Online]. Available: https://cds.cern.ch/record/1974062?ln=en

[11] P. Lebrun, "Design of a cryostat for superconducting accelerator magnets: The LHC main dipole case," 2004.

[12] CERN. (2025) Home | CERN. Accessed: February 24, 2025. [Online]. Available: https://home.cern/

[13] O. S. Brüning, P. Collier, P. Lebrun, S. Myers, R. Ostojic, J. Poole, and P. Proudlock, *LHC Design Report*, ser. CERN Yellow Reports: Monographs. Geneva: CERN, 2004. [Online]. Available: https://cds.cern.ch/record/782076

[14] J. J. Kosse, "Superconducting magnets for magnetic density separation: A NbTi based demonstrator," Ph.D. dissertation, University of Twente, Mar 2021. [Online]. Available: https://research.utwente.nl/en/publications/superconducting-magnets-for-magnetic-density-separation-a-nbti-ba

[15] Beyond Gravity. (2024) Cryogenic Superinsulation | Beyond Gravity. Accessed: Feb 24, 2025. [Online]. Available: https://www.beyondgravity.com/en/satellites/thermal-control-solutions/cryogenic-superinsulation

[16] C. Calzolaio, S. Sanfilippo, S. Sidorov, A. Anghel, and A. Streun, "Design of a Superconducting Longitudinal Gradient Bend Magnet for the SLS Upgrade," *IEEE Transactions on Applied Superconductivity*, vol. 27, no. 4, pp. 1–5, Jun. 2017.

[17] HTS-110. (2024) Superconducting current leads. Accessed: Feb 24, 2025. [Online]. Available: https://www.hts-110.com/product/cryosaver-current-leads/

[18] H. Garmestani, M. Vaghar, and W. Markiewicz, "Concepts of plasticity in solenoid stress analysis," *IEEE Transactions on Magnetics*, vol. 30, no. 4, pp. 2237–2240, Jul. 1994.

[19] L. Bottura, "Magnet quench 101," in *Workshop on Accelerator Magnet, Superconductor Design and Optimization*, 2013, pp. 1–9.

[20] L. Bottura, "Cable stability," in *CERN Accelerator School: Course on Superconductivity for Accelerators*, 2014, pp. 401–451.

[21] L. Bottura, "Margin, stability and quench models and simulation," in *Proceedings of the 3rd International School on Numerical Modelling for Applied Superconductivity*, 2010.

[22] L. Rossi, S. Mariotto, and S. Sorti, "Energy saving magnets for beam lines," *Journal of Physics: Conference Series*, vol. 2687, no. 8, p. 082049, Jan. 2024.

[23] F. Nardai, H. Weber, and R. Maix, "Neutron irradiation of a broad spectrum of NbTi superconductors," *Cryogenics*, vol. 21, no. 4, pp. 223–233, Apr. 1981.

[24] B. S. Brown, "Radiation effects in superconducting fusion-magnet materials," *Journal of Nuclear Materials*, vol. 97, no. 1-2, pp. 1–14, Mar. 1981.

[25] P. Hahn, H. Hoch, H. Weber, R. Birtcher, and B. Brown, "Simulation of fusion reactor conditions for superconducting magnet materials," *Journal of Nuclear Materials*, vol. 141–143, pp. 405–409, Nov. 1986.

[26] C. Snead and T. Luhman, "Radiation Damage and Stress Effects in Superconductors: Materials for High-Field Applications," in *Modern Problems in Condensed Matter Sciences*. Elsevier, 1986, vol. 13, pp. 345–386.

[27] A. Will, A. Bernhard, M. Bonura, B. Bordini, M. Mentink, A.-S. Mueller, A. Oslandsbotn, R. Schmidt, J. Schubert, C. Senatore, A. Siemko, A. Verweij, and D. Wollmann, "Impact of 440 GeV Proton beams on Superconductors in a Cryogenic Environment," *Journal of Physics: Conference Series*, vol. 1559, no. 1, p. 012060, Jun. 2020.

[28] V. Raginel, M. Bonura, D. Kleiven, K. Kulesz, M. Mentink, C. Senatore, R. Schmidt, A. Siemko, A. Verweij, A. Will, and D. Wollmann, "First Experimental Results on Damage Limits of Superconducting Accelerator Magnet Components Due to Instantaneous Beam Impact," *IEEE Transactions on Applied Superconductivity*, vol. 28, no. 4, pp. 1–10, Jun. 2018.

[29] C. Hernalsteens, D. Wollmann, A. Grau, C. Wiesner, A. Bernhard, E. Gnacadja, N. Glamann, D. Saez de Jauregui, R. Tesse, S. Thomsen, L. Pauwels, A.-S. Mueller, D. Gancarcik, E. Ramoisiaux, and F. Abusaif, "Energy deposition simulations for a damage experiment with superconducting sample coils," in *Proceedings of IPAC 2023*. JACoW, 2024, pp. 3696–3699.

[30] R. D. Brown and J. R. Cost, "Radiation effects in magnetic and superconducting materials," *JOM*, vol. 42, no. 2, pp. 39–43, Feb. 1990.

[31] J. O. Willis, D. W. Cooke, R. D. Brown, J. R. Cost, J. F. Smith, J. L. Smith, R. M. Aikin, and M. Maez, "Proton radiation damage in superconducting EuBa2Cu3O $x$ and GdBa2Cu3O $x$," *Applied Physics Letters*, vol. 53, no. 5, pp. 417–419, Aug. 1988.

[32] H. W. Weber, "Radiation effects on superconducting fusion magnet components," *International Journal of Modern Physics E*, vol. 20, no. 06, pp. 1325–1378, 2011, accessed: Feb 24, 2025. [Online]. Available: https://www.worldscientific.com/doi/epdf/10.1142/S0218301311018526

[33] D. X. Fischer, R. Prokopec, J. Emhofer, and M. Eisterer, "The effect of fast neutron irradiation on the superconducting properties of REBCO coated conductors with and without artificial pinning centers," *Superconductor Science and Technology*, vol. 31, no. 4, p. 044006, Apr. 2018.

[34] K. S. Chang, H. C. Jo, Y. J. Kim, M. CheolAhn, and T. K. Ko, "An Experimental Study on the Joint Methods Between Double Pancake Coils Using YBCO Coated Conductors," *IEEE Transactions on Applied Superconductivity*, vol. 21, no. 3, pp. 3005–3008, Jun. 2011.

[35] R. Prokopec, D. X. Fischer, H. W. Weber, and M. Eisterer, "Suitability of coated conductors for fusion magnets in view of their radiation response," *Superconductor Science and Technology*, vol. 28, no. 1, p. 014005, Jan.

2015.

[36] M. Jirsa, M. Rameš, I. Ďuran, T. Entler, and L. Viererbl, "Critical currents in REBaCuO superconducting tapes in response to neutron irradiation," *Superconductor Science and Technology*, vol. 32, no. 5, p. 055007, May 2019.

[37] D. Torsello, D. Gambino, L. Gozzelino, A. Trotta, and F. Laviano, "Expected radiation environment and damage for YBCO tapes in compact fusion reactors," *Superconductor Science and Technology*, vol. 36, no. 1, p. 014003, Jan. 2023.

[38] D. M. Parragh, C. Scheuerlein, R. Piccin, F. Ravotti, G. Pezzullo, D. Ternova, M. Taborelli, M. Lehner, and M. Eisterer, "Irradiation Induced Aging of Epoxy Resins for Impregnation of Superconducting Magnet Coils," *IEEE Transactions on Applied Superconductivity*, vol. 34, no. 3, pp. 1–7, May 2024.

[39] CERN. (2025) Radsum - topical workshop on radiation effects in superconducting magnets. Accessed: Feb 24, 2025. [Online]. Available: https://indico.cern.ch/event/1450988/

[40] Z. Xie, G. Zhao, Z. Zhu, Z. Hou, G. Zhang, Y. Yuan, N. Vassilopoulos, M. Wang, and F. Ning, "Analysis of thermal characteristics for EMuS capture solenoids," *Radiation Detection Technology and Methods*, vol. 5, no. 4, pp. 542–549, Dec. 2021.

[41] Makoto Yoshida, M. Yoshida, M. Yoshida, M. Yoshida, T. Nakamoto, T. Nakamoto, T. Ogitsu, T. Ogitsu, Kenichi Tanaka, K. Tanaka, A. Yamamoto, A. Yamamoto, M. Aoki, M. Aoki, Y. Kuno, Y. Kuno, Akira Sato, and A. Sato, "Superconducting Solenoid Magnets for the COMET Experiment," *IEEE Transactions on Applied Superconductivity*, vol. 21, no. 3, pp. 1730–1733, Jun. 2011.

[42] Makoto Yoshida, M. Yoshida, M. Yoshida, Mitsuhiro Fukuda, M. Fukuda, K. Hatanaka, K. Hatanaka, Y. Kuno, Y. Kuno, T. Ogitsu, T. Ogitsu, Akira Sato, A. Sato, A. Yamamoto, and A. Yamamoto, "Superconducting Solenoid Magnets for the MuSIC Project," *IEEE Transactions on Applied Superconductivity*, vol. 21, no. 3, pp. 1752–1755, Jun. 2011.

[43] Y. Elmahroug, B. Tellili, and C. Souga, "Calculation of fast neutron removal cross-sections for different shielding materials," *International Journal of Physics and Research (IJPR)*, vol. 3, pp. 7–16, 06 2013.

[44] B. Tellili, Y. Elmahroug, and C. Souga, "Calculation of fast neutron removal cross sections for different lunar soils," *Advances in Space Research*, vol. 53, no. 2, pp. 348–352, Jan 2014.

[45] Y. Afkham, A. Mesbahi, A. Alemi, F. Zolfagharpour, and N. Jabbari, "Design and fabrication of a nano-based neutron shield for fast neutrons from medical linear accelerators in radiation therapy," *Radiation Oncology*, vol. 15, no. 1, pp. 1–13, May 2020.

[46] H. C. Jo, S. Choi, J. B. Na, J. Y. Jang, Y. J. Hwang, H. J. Kim, M. C. Ahn, Y. D. Chung, H. M. Kim, Y. S. Yoon, K.-S. Ryu, Y.-C. Kim, H. Lee, and T. K. Ko, "Characteristic comparison for the various winding methods of hts magnets," *IEEE Transactions on Applied Superconductivity*, vol. 22, no. 3, pp. 4902–4907, Jun. 2012.

[47] T. H. Nes, G. De Rijk, A. Kario, and H. H. J. Ten Kate, "Differential geometry method for minimum hard-way bending 3D design of coils with ReBCO tape conductor," *Superconductor Science and Technology*, vol. 35, no. 10, p. 105011, Oct. 2022.

[48] F. Hornung, M. Eisele, M. Klaeser, P. Leys, C. Ruf, and T. Schneider, "From Double-Pancake Coils to a Layer Wound 5 T REBCO-HTS High Field Insert Coil Design," *IEEE Transactions on Applied Superconductivity*, vol. 27, no. 4, pp. 1–4, Jun. 2017.

[49] C. Barth, G. Mondonico, and C. Senatore, "Electro-mechanical properties of REBCO coated conductors from various industrial manufacturers at 77 K, self-field and 4.2 K, 19 T," *Superconductor Science and Technology*, vol. 28, no. 4, p. 045011, Apr. 2015.

[50] J. Kosse, B. Auchmann, M. Duda, J. van Nugteren, S. Mueller, H. Rodrigues, and S. Sanfilippo, "HTS Solenoids at PSI," 2022, presentation at the Muon Collider Workshop, October 12. [Online]. Available: https://indico.cern.ch/event/1175126/contributions/5024246/attachments/2526079/4345515/2022_Muon_collider_P3_PSI_Kosse_V3.pdf

[51] S. Mariotto, L. Rossi, and S. Sorti, "Design of Energy-Saving MgB$_\text{2}$ Ramped Superconducting Magnets for Particle Beam Lines," *IEEE Transactions on Applied Superconductivity*, vol. 34, no. 3, pp. 1–5, May 2024.

[52] M. A. Green and B. P. Strauss, "Estimating the Operating Cost of Superconducting Magnet Systems at Various Operating Temperatures," *IEEE Transactions on Applied Superconductivity*, vol. 26, no. 4, pp. 1–5, Jun. 2016.

[53] R. Teyber, L. Brouwer, A. Godeke, and S. Prestemon, "Thermoeconomic cost optimization of superconducting magnets for proton therapy gantries," *Superconductor Science and Technology*, vol. 33, no. 10, p. 105005, Oct. 2020.

[54] Electricity Maps. Electricity Map - Hourly Data Visualization. Accessed: Feb 24, 2025. [Online]. Available: https://app.electricitymaps.com/map/72h/hourly

[55] A. Buchholz, M. Noe, D. Kottonau, E. Shabagin, and M. Weil, "Environmental Life-Cycle Assessment of a 10 Kv High-Temperature Superconducting Cable System for Energy Distribution," *IEEE Transactions on Applied Superconductivity*, vol. 31, no. 5, pp. 1–5, Aug. 2021.

[56] T. Hartikainen, A. Korpela, J. Lehtonen, and R. Mikkonen, "A comparative life-cycle assessment between NbTi and copper magnets," *IEEE Transactions on Applied Superconductivity*, vol. 14, no. 2, pp. 1882–1885, Jun. 2004.

[57] M. Bonura and C. Senatore, "Transverse Thermal Conductivity of REBCO Coated Conductors," *IEEE Transactions on Applied Superconductivity*, vol. 25, no. 3, pp. 1–4, Jun. 2015.

[58] M. Bonura, "High-field thermal transport properties of REBCO coated conductors," *Superconductor Science and Technology*, no. 2, p. 025001, Feb 2015.

[59] SHI Cryogenics. (2025) RDK-305D2 4K Cryocooler Series. Accessed: Feb 24, 2025. [Online]. Available: https://shicryogenics.com/product/rdk-305d2-4k-cryocooler-series/

[60] SHI Cryogenics. (2025) CH-110LT 40K Cryocooler Series. Accessed: Feb 24, 2025. [Online]. Available: https://shicryogenics.com/product/ch-110lt-40k-cryocooler-series/

[61] SHI Cryogenics. (2025) RD-125D 77K Cryocooler Series. Accessed: Feb 24, 2025. [Online]. Available: https://shicryogenics.com/product/rd-125d-77k-cryocooler-series/

[62] W. Frei. (2013) Meshing Your Geometry: When to Use the Various Element Types. Accessed: Feb 24, 2025. [Online]. Available: https://www.comsol.com/blogs/meshing-your-geometry-various-element-types

[63] H. Gothäll. (2022) How to Inspect Your Mesh in COMSOL Multiphysics®. Accessed: Feb 24, 2025. [Online]. Available: https://www.comsol.com/blogs/how-to-inspect-your-mesh-in-comsol-multiphysics

[64] COMSOL. Adaptive Mesh Refinement. Accessed: Feb 24, 2025. [Online]. Available: https://doc.comsol.com/5.5/doc/com.comsol.help.comsol/comsol_ref_solver.27.134.html

[65] COMSOL. (2017) Finite Element Mesh Refinement Definition and Techniques. Accessed: Feb 24, 2025. [Online]. Available: https://www.comsol.com/multiphysics/mesh-refinement

[66] S. Wimbush, N. Strickland, and A. Pantoja. (2021) Critical current characterisation of Fujikura FYSC 2G HTS superconducting wire. Accessed: Feb 24, 2025. [Online]. Available: https://htsdb.wimbush.eu/dataset/3759321

[67] W. Prusseit, "HTS wire for high field magnet applications," Presentation, CERN Roadmap Workshop, 2021, Accessed: Feb 24, 2025. [Online]. Available: https://indico.cern.ch/event/1032199/contributions/4359092/attachments/2255357/3826776/THEVA%20%40%20CERN%20roadmap%20workshop%20010621.pdf

[68] EPFL. Sultan_Facility. https://www.epfl.ch/research/domains/swiss-plasma-center/research/superconductivity/page-97675-en-html/. Accessed: June 6, 2025.

[69] Federal Office for the Environment. (2024) Climate: In brief. Accessed: Feb 24, 2025. [Online]. Available: https://www.bafu.admin.ch/bafu/en/home/themen/thema-klima/klima--das-wichtigste-in-kuerze.html

[70] M. Bonura. (2015) NZPV and MQE from electrical and thermal properties of commercial REBCO tapes. Accessed: Feb 24, 2025. [Online]. Available: https://indico.cern.ch/event/396905/contributions/1837519/attachments/1152230/1654608/Bonura_WAMHTS-3.pdf